EFFECTIVE TREATMENT OF SOLID TUMORS VIA CRYOSURGERY

ZHAO XING

(*B.Eng.*, DALIAN UNIVERSITY OF TECHNOLOGY, CHINA)

A THESIS SUBMITTED

FOR THE DEGREE OF DOCTOR OF PHILOSOPHY

DEPARTMENT OF MECHANICAL ENGINEERING

NATIONAL UNIVERSITY OF SINGAPORE

2013

Declaration

I hereby declare that this thesis is my original work and it has been written by me in its entirety.

I have duly acknowledged all the sources of information which have been used in the thesis.

This thesis has also not been submitted for any degree in any university previously.

_____

Zhao Xing

01 Jul 2013

Acknowledgements

The success of this project was achieved by a group of knowledgeable, supportive and helpful people. First and foremost, the author would like to thank Dr. Kian Jon Chua for his supports and invaluable guidance during the study. His constant monitoring and enlightening advice have motivated the author to achieve sound results and have driven the author to make extra effort to understand the key issues related to the project. Heartfelt gratitude is also expressed to Prof. Siaw Kiang Chou to acknowledge his enormous supports and encouragement throughout the course of the project. His invaluable guidance and constructive comments have largely promoted the quality of the work. In addition, the author is also thankful to Mr. Tiong Thiam Tan for his assistance during experiments.

Last but not least, the author wishes to extend his sincerest appreciation to the love, support and encouragement from my parents and other family members.

Many thanks to you all,

Zhao Xing
01 Jul, 2013

Table of Contents

Summary

Cryosurgery is an effective medical treatment for the tumor ablation by employing extreme cold to destroy abnormal tissues. The low temperature environment is usually created through a cryo-device coined as cryoprobe. Due to the small dimension of a cryoprobe, the cryosurgery has been widely accepted as a minimally invasive therapy for tumor treatments. However, cryosurgery frequently falls short of maximizing the cryoinjury within the targeted region while minimizing the damage to the surrounding healthy tissues.

This dissertation discloses important thermal observations for cryosurgical processes and develops operating protocols to produce the optimized ablation zone to cover the tumor profile. The mathematical models are developed to analyze the bioheat transfer in the biological tissue with different operating procedures. The models have been validated by experimental data.

The effects of experimental parameters on the freezing delivery in the cryosurgical system have been analyzed. These parameters control the performance of cryosurgical system. The performance becomes important when the cryosurgery is executed based on the cryosurgery planning for freeze-thaw cycles. We modify and improve the conventional cryosurgical system. The modified system significantly reduces the real-time fluctuations of the flow rate. The impacts of key experimental parameters on the cryosurgical system are quantified by using the orthogonal experimental method.

The treatment of irregularly shaped tumors is another interesting topic in cryosurgery. The irregularly shaped tumors can markedly compromise the

effectiveness of cryosurgery, inducing tumor recurrences or undesired large amount of over-freezing in the surrounding healthy tissues. A bifurcate cryoprobe is proposed with the capability to generate irregularly shaped ablation zone. Simulation results indicate that the bifurcate cryoprobe can generate larger ablation zone with higher degree of profile irregularity, but it incurs the penalty of higher invasive trauma.

Another important consideration for the tumor treatment is the heating effect of blood flows. To evaluate the heating effect, the numerical model is incorporated with a clinically-extracted vessel network. *In-vitro* experiments are conducted to verify the model. The validated model simulates temperature developments in vascular tissue and investigates the thermal influence in response to different blood flow rates. The study shows that the large blood vessels are effective in reshaping the frozen tissue, but it induces less thermal influence on the isotherm at the critical temperature (i.e. 233 K).

Besides studying the cryo-freezing process, cryosurgery can employ complementary heating tools to enhance the cryosurgical efficacy. We promote the performance of cryosurgery by incorporating the Joule heating and radiofrequency-generated (RF-generated) heating. The intention of incorporating heating into cryosurgery is to protect healthy tissue surrounding the tumor. The healthy tissue close to the tumor can be inevitably frozen due to extremely low temperatures. The frozen tissue beyond tumor is unwanted and it ought to be reduced.

The Joule heating has been applied to minimize the unwanted frozen zone. For internal tumors, the unwanted frozen tissue is controlled by heating probes named cryo-heaters. Cryo-heaters at essential locations are observed to be effective in reducing the growth of frozen tissue and sustaining an excellent coverage of complete ablation zone. We also identify the existence

of diminishing temperature effect when alternate freeze-thaw cycles are applied. For surface tumors, the unwanted frozen tissue can be controlled by a simple heating coil. A dimensionless parameter, heating coil coefficient, is applied to study the performance of heating coil. Smaller coils are found to perform well in terms of reducing the unwanted frozen zone but they are associated with short operating durations.

Compared to Joule heating, RF-generated heating is famous to destroy aberrant tissues with a minimally invasive nature. We have built an axisymmetric three-dimensional finite element model that evaluates the performance of RF-assisted cryosurgery. In the first stage, the RF ablation and cryosurgical ablation are studied separately. This helps to validate the numerical models with their respective experimental data. The second stage contains a proposed RF-assisted cryo-device. The electrode and the ground pad in a conventional RF ablation system are incorporated within a cryoprobe. This RF-assisted cryosurgery is capable of producing RF-generated heating during the freezing. Results show that the RF-assisted cryosurgery could reduce the frozen tissue and sustain the size of complete ablation. However, the RF-generated heating was not effective as the cartridge heating in terms of reshaping the frozen tissue.

List of Tables

List of Figures

XI

XIV

List of Symbols

C	specific heat capacity ($J \cdot kg^{-1} K^{-1}$)
CB	cryosurgery bulkiness
D_S	damage function of tissue
E	deviation modulus
E_a	activation energy ($J \cdot mol^{-1}$)
f_s	solid faction in phase change
F	sum of the evaluation index
h	combined convection heat transfer coefficient ($W \cdot m^{-2} K^{-1}$)
h_L	specific latent heat ($J \cdot kg^{-1}$)
I_{rr}	irregularity
ΔG	Gibbs free energy of inactivation (J)
i	number of iteration step
IF	initial freezing
k	thermal conductivity ($W \cdot m^{-1} K^{-1}$)
k^*	number of factors in orthogonal exp. analysis
l^*	number of levels in orthogonal exp. analysis
m	total number of iterations
n	number of freeze-thaw cycles
$\hat{n}$	vector normal to the surface
Nor	normality
P_k	Planck's constant
Q_m	metabolism heat ($W \cdot m^{-3}$)
R	the universal gas constant ($J \cdot mol^{-1} K^{-1}$)
R_{al} , R_{bl}	length between the 233 K and 323 K isotherm at line A and line B in the first freeze-thaw cycle (m)
R_s	designated circular arc path (m)
r	radial distance from the center of cryoprobe (m)

t	time (s)
t_0	total duration of the freezing/heating process (s)
t^*	duration to achieve a relative stable temperature (s)
T	temperature (K)
T^*	critical temperature for boundary conditions (K)
T_1^*	minimum temperature for all tissue to survive (K)
T_2^*	maximum temperature for all tissue to survive (K)
T_{fc}^*	critical temperature of complete ablation for freezing (K)
T_{tc}^*	critical temperature of complete ablation for heating (K)
TC	thermocouple
$\tilde{u}$	vector of coordination
V_{equ}	volume of equivalent ellipsoid (m^3)
V_{tum}	volume of isothermal surface (m^3)
X	location
Y	targeted factor
x,y,z	cartesian coordinate (m)
u,v,w	velocity in the direction of x,y,z ($m \cdot s^{-1}$)

Greek symbols

α	constant
β	angle between the primary and secondary probe ($^\circ$)
Γ, Λ, Π	computational volume of unfrozen, mushy and frozen zone
γ	Boltzmann's constant
δ	percentage of temperature drop
ε	pre-exponential factor
κ	constant
μ	dynamic viscosity ($kg \cdot m^{-1} s^{-1}$)
ρ	density ($kg \cdot m^{-3}$)
σ	electrical conductivity (S/m)
τ_1, τ_2	overlapping effects of the damage induced by freeze-thaw

	cycles
φ	general variable
Φ	probe temperature at the initial stage
ω_b	blood perfusion rate (s^{-1})
Subscripts	
a,b,c	frozen region, mushy region and unfrozen region
A,B,C	selected influencing factors
ar	artery
amb	ambiance
bf	blood flow
fc,tc	freezing cycle, thawing cycle
ini	initial stage
p	probe
sta	stable
t	tissue

Chapter 1:   Introduction

1.1.   Background

Tumors are the malignant growth by abnormal and uncontrolled cells. They are formed because the mutated gene dispatches an incorrect message that causes cells to grow rapidly. When the growth is limited in one spot, the tumor is considered as to be benign. When a tumor spreads to other parts of the body and grows, invading and destroying other healthy tissues, it is deemed to be malignant and the process is coined as metastasis. Tumors are can be broken down into solid tumors (organ tumors) and liquid tumors (blood cancers). This work focuses on treatments for solid tumors.

The global burden of cancer continues to increase because of the growth of the world population and an increasing adoption of cancer-causing behaviors [1]. Overall, estimated 12.7 million new cancer cases and 7.6 million cancer death occur in 2008, with 56 % of new cancer cases and 63% of the cancer occurring in the less developed regions of the world [2]. The rapid global increase in cancer occurrence has imposed great interests to enhance treatments. Currently, the common cancer treatments include surgical excision, radiation therapy, chemotherapy, hormone therapy, radiofrequency ablation, and cryosurgery.

Cryosurgery, or tissue destruction by controlled freezing, has been known to be an effective and minimally invasive therapy to treat tumors by employing cryogenic temperatures [3, 4]. Compared to other treatments such as surgical excision, radiation therapy and chemotherapy, it is relatively low cost and induces less damage to the surrounding healthy tissue. In a typical cryosurgical process, the undesired tissue undergoes liquid-solid and reverses phase

transformation. Successful cryosurgery means maximal destruction of cancerous cells while minimizing cryoinjury to the surrounding healthy tissue. This therapy has been widely applied to treat cancerous cells of liver, lung, encephalon and bone [5-9]. Hepatic cryosurgery is the major focus of this dissertation. It has been increasingly effective for the unresectable cancer treatment that may be associated with underlying diseases, bilobar hepatic metastases, and anatomic location limits such as bifurcation of portal veins and confluence of hepatic veins. However, the cryosurgical protocol in the vascular network is still far from being well-established. Crucial issues, such as the recurrence of tumors and the protection of surrounding health tissue, still need to be improved. Therefore, more investigation should be carried out to advance the fundamental understanding of the underlying mechanisms and pragmatic approaches to enhance the performance of cryosurgery.

1.2. Objectives

The specific objectives of this study are:

a.) Understand the influence of controlling parameters on the performance of cryosurgical system. Enhance the control accuracy during the freezing process.

b.) Evaluate the thermal effects of large blood vessels in complex blood network. Develop the numerical model to simulate the bioheat transfer process with a clinically-extracted vessel network.

c.) Develop feasible cryo-devices to generate irregularly shaped ablation zones. These cryo-devices should be feasible to cater the cryosurgical demand during the treatment of highly irregular-shaped tumors.

d.) Incorporate cartridge heating elements into the cryosurgical process and study the performances of the heating elements. Investigate the degree of thermal injury during cryosurgery.

e.) Apply RF-generated heating to reshape the frozen tissue and protect the surrounding healthy tissue during cryosurgery. Compare the RF-generated heating with the Joule heating.

1.3.   Scope

The scope of this study covers:

a.) Understand the correlation of controlling parameters (i.e. pressure and flow rate) during the cryosurgical process. A series of experimental tests are conducted in *in-vitro* liver samples to discover the impacts of different parameters.

b.) Develop feasible numerical model to investigate and optimize cryosurgical processes, especially in the vascular tissue where the structure of the blood vessels cannot be neglected. Develop the damage function that covers over-lapping effects of the freeze-thaw cycles. Validate the proposed models with the experimental data or results in reference.

c.) Protect the surrounding healthy tissue by incorporating heating elements. Test the performance of Joule heating and RF-generated heating. Incorporate these heating mechanisms into cryosurgery to promote the cryosurgical performance.

1.4.   Outline

Brief descriptions of all chapters in this dissertation are summarized as below:

Chapter 1 provides a general introduction of this dissertation, including the backgrounds, objectives, scope and outline.

Chapter 2 reviews existing literatures related to cryosurgical techniques. The monitoring technologies during cryosurgery are discussed. Besides of cryosurgical procedure, we also review the mechanism of tissue injury, thermal impacts of large blood vessels and metabolism. Additionally, the RF ablation, as a competitive minimally-invasive therapy to cryosurgery, is introduced with its advantages and disadvantages.

Chapter 3 develops several mathematical models to enhance the predictability of the bioheat transfer processes. These models cover the cryo-freezing, cartridge heating and RF ablation. Furthermore, the data process scheme and method of orthogonal experiment analysis are presented. The function of tissue damage for freeze-thaw cycles is proposed.

Chapter 4 describes the experimental facilities and procedures in this research campaign. Experimental procedures of the conventional cryosurgery, cryosurgery incorporating peripheral Joule heating and RF ablation are presented. The uncertainties of the devices used during experiments are given.

Chapter 5 provides in-depth results of promoting the efficacy and accuracy of the cryo-freezing process. Firstly, a set of experiments are tested to determine the important controlling factors and their influences during cryosurgery. Secondly, irregularly shaped ablation zones that cater the surgical demands of irregular tumors are quantified. The shape factor was proposed to identify the

effectiveness of the conventional cryoprobe and bifurcate cryoprobes. Lastly, the bioheat transfer process embedded with a complex blood network has been successfully simulated.

Chapter 6 incorporates the peripheral Joule heating to reduce the unwanted frozen zone for internal and surface tumors. Tissue demarcation, based on the tissue cellular state and tissue frozen state, is given. The proposed tissue damage model for cryoablation with freeze-thaw cycles is successfully applied to estimate cell damage rate. Cryo-heaters and heating coil are tested for the internal tumors and surface tumor, respectively. The efficacies of the devices are evaluated. The scheme of the selection of the appropriate heating coil is given.

Chapter 7 evaluates the performance of RF-assisted cryosurgery. The electrode and the ground pad in a conventional RF ablation system are incorporated within a cryoprobe. This RF-assisted cryosurgery is capable of producing heating while freezing.

Chapter 8 summarizes the major results and lists the key contributions to knowledge. The limitations of this study and the recommendations for future work are given.

Chapter 2: Literature Review

In this chapter, the literature review starts with cryosurgical techniques. Readers can obtain a comprehensive understanding on the development, principle and limitations of this technique. Secondly, several monitoring technologies during cryosurgery are compared and their advantages and disadvantages are discussed. Thirdly, the mechanisms of thermal injury in biological tissue are reviewed and cell injuries due to thermal influence are classified. Fourthly, the main heat sources in the biological tissue, including large blood vessels and metabolism, are discussed. In the last section, we review on RF ablation, which is a very competitive thermal therapy as compared to cryosurgery.

2.1.   Cryosurgical technique

The first publication of using extreme cold for the destruction of tissue dates back between 1819 and 1879 [10]. The physician of Brighton Infirmary used a mixture of salt and crushes ice for palliation of tumors. However, salt/ice mixtures are not capable of reducing tissue temperature sufficiently to treat tumors. In the late 1800s, at a time of tremendous scientific advance, Cailletet claimed that the oxygen and carbon monoxide could be liquefied under high pressure [11]. The first person to employ refrigerants for the medical application was Campbell White with a report in 1899, advocating liquid air for a large range of conditions in treatment [11]. Thereafter, the debate on the best cryogen persisted for the first half of the twentieth century. Argon gas is a freezing medium under high pressure by Joule-Thomson effect. Argon gas has an advantage of cooling the probe more quickly than the liquid nitrogen does;

however, the minimum temperature that argon gas can achieve is much higher. Therefore, in the past decades, many studies in cryobiology have taken the cooling effects of liquid nitrogen. Eventually, the liquid nitrogen becomes one of the most accepted freezing medium in cryosurgery [12, 13].

The low temperatures during cryosurgery is delivered by a cryo-device. The first generation of cryo-devices dates back in the early 1960's. Gondor et. al. used a funnel through which liquid nitrogen was poured [14]. The design was subsequently replaced by probes in large diameters. However, both of the designs were abandoned due to the high rate of complications and poor accuracy. The applicable cryoprobes were merged in the late 1980's [14]. The cryoprobe vaporizes the freezing medium based on Joule-Thomson principle. The mechanism allows the cryoprobe to reduce diameters to a range of 8 mm. Owing to development of manufacturing technology, ultra-thin cryoprobes are available in the market nowadays (1.47 mm diameter, GalilMedical Inc., Minneapolis, Mn). The cryoprobe with small diameter facilities the invasive process during cryotherapy.

The latest technologies associated with cryosurgical systems provide two methods to deliver freezing mediums. The cryoablation can be generated by spraying the freezing medium directly on the targeted tissue [15, 16]. There are some available products spraying the freezing medium to treat benign skin lesions (i.e. CryoProbe™ , H&O Equipments Inc., Belgium). However, due to the risk of gas embolism [17], the type of cryoablation has limited applications. Most cryosurgeries nowadays are accomplished by a non-contact gas expansion method (Joule-Thomson). The method separates the freezing medium from cancer cells by a cryoprobe. The cryoprobe normally houses a coaxial inner tube [18, 19]. The downstream of the inner tube contains a small chamber enclosed within the tip of cryoprobe. When the pressurized liquid

freezing medium passes through the inner tube, the medium vaporizes in the small chamber, creating extremely low temperatures. Then, the freezing medium streams back through an interlayer between the coaxial inner tube and the wall of cryoprobe. The design has demonstrated significant improvements on the controlling of the freezing process and it has avoided the risk of gas embolism.

Albeit the performance of cryo-device has been significantly improved during past decades, there are still several challenges to ensure a successful cryosurgery. The first challenge is to enhance the accuracy of freezing process, specifically when solid tumors are closed to large blood vessels or important organs. Large blood vessels can significantly accelerate the bioheat transfer and compromise the freezing ability [3]. Without sufficient considerations of large blood vessels, the cryosurgery can turn out to be a failure [20]. Given the importance of large blood flow, many studies have conducted on the visualization of blood vessels [21, 22], the reconstruction of vascular network [23-25] and the simulation of the cryosurgical process [4, 26-29]. The most famous model of bioheat transfer is the Pennes model [30]. It employs a perfusion heat source term to simplify complex blood flows. However, Wulff criticized the Pennes model because the presence of arterial and venous blood streams rendered the existence of continuous gradients in tissue temperatures implied [31]. To consider the heating effect of blood flow, some studies have simplified the blood vessels by fractal-like tree networks [25, 27, 32, 33]. These models investigate the capillary pressure and the flow pattern well; however, these simulations, often than not, ignore the physical structure of blood vessels and is incapable of producing simulations with real blood network. Until now, there are still plenty of debates on the best cryosurgery planning to simulate the thermal development in a complex blood network.

Cryosurgery planning involves determinations of essential operating parameters, adopting the appropriate monitoring technique, identifying the best positioning of the cryoprobe, and developing a well-controlled system to achieve the best surgical outcome. Although many efforts have devoted to cryosurgery planning [4, 9, 34, 35], specific studies dedicate to investigating parameters that enhance the control of cryosurgical system are still lacking. Basic thermal properties such as the flow rate of freezing medium, temperatures, and pressures at essential locations in the conventional cryosurgical system can significantly affect the cryosurgical performance. Understanding these parameters helps cryosurgeons to control the cryosurgical system according to the results of cryosurgery planning.

Another challenge associated with cryosurgery is to improve the reliability, the accuracy and the flexibility of cryosurgical devices. Extremely low temperatures bring a host of challenges of protecting the surrounding healthy tissue from cryoinjury. Considering that the tumor edge is at the critical temperature (i.e. 233 K [36-42]), beyond it, large amounts of healthy tissue suffer the cryoinjury due to low temperatures. Therefore, additional tools are taken to protect the surrounding healthy tissue. Rabin and Shitzer protected the surrounding healthy tissue by a computer-controlled cryo-device with electrical heating elements [43]. The device was characterized with an effective penetration depth of the cryolesion in the range of 5 mm to 15 mm [43]. They have conducted simple tests and successfully applied heating probes to protect the surrounding healthy tissue. Moreover, for the treatment of large tumors, cryosurgery must employ additional cryoprobes to generate a large complete ablation zone to cover the profile of tumor. Involving additional cryoprobes are often troublesome. They need to determine extra allocations of added cryoprobes. Therefore, a complex cryosurgery planning for the optimization of probe allocations is often necessary. Furthermore, some

cryo-device has been improved with the flexibility to cater the complex surgical demands, such as irregularly shaped tumors. For example, Yan et. al. proposed a new modality for maximizing cryosurgical killing for the treatment of the slender or elongated solid tumors [44]. The modality, named as one time's percutaneous insertion with multiple freezing/heating ablations, could reduce the mechanical incision trauma compared to the conventional cryosurgical freezing. Owing to the heating function incorporated within the probe, their proposed probe was capable of moving along its original incision tract to desired positions to generate a series of frozen tissues [44]. Until recently, there have been plenty of studies dedicated to enhance the performance by new cryo-therapies [24, 45-47].

The third challenge associated with cryosurgery is the basic understanding of the mechanism of tissue damage in cryobiology. It is generally believed that the freezing rate of cryoprobe is an important factor for cell damage. The freezing rate of cryoprobe should be as fast as possible to facilitate the heat exchange. The freezing rate of the cryoprobe is rapid, commonly more than 60 K/min at the initial stage [48]. The fast freezing process freezes the intracellular water. The intracellular ice can permanently disrupt cell membranes. The thawing process enables ice crystals to fuse and form large crystals, propelling further damage to cells. Although many studies have been focused on the damage mechanism [45, 49, 50], the cryosurgical procedure has little change in recent years. It is generally believed that a fast freezing, slow thawing, and the repetition of freeze-thaw cycles are essential tenets of cryosurgery [41, 51]. A comprehensive review on mechanism of the tissue injury is given in Section 2.3.

2.2. Monitoring technologies

2.2.1. Visualization of the vascular network

The structure of blood vessels is very important for the cryosurgery planning. Many technologies have been employed to visualize and reconstruct organ vessels [21, 52, 53]. Angiography, a medical imaging technique, visualizes arteries and veins by injecting a radio-opaque contrast agent into blood vessels to obtain the structure by X-ray based technique. Besides, fluoroscopy is a common method used to obtain real-time images of internal structures of a patient through use of a fluoroscope. Additionally, cone-beam X-ray-projection-based volume imaging with flat panel detectors (FPDs) allows obtaining three-dimensional images with better accuracy[54]. These techniques help to reconstruct the organ vessels in the cryosurgery planning.

2.2.2. Monitoring technique of temperatures

The monitoring techniques of temperatures, principally temperature sensors and ultrasonography, have undergone a great advance since 1990s. The technologic development in monitoring the freezing process provides the foundation for a wider use of cryosurgical techniques [48]. The clinical visualizations produced by monitoring technologies help physicians to make judicious judgments of the extent of freezing [21, 52, 53]. One of the oldest monitoring technologies is the application of thermocouple probes. Tissue temperatures are measured by placing needle-mounted thermocouples at appropriate sites. For instance, one of the popular applications of using a thermocouple is to place it 10 mm from the edge of tumor. The real-time temperature data produced by the thermocouple assists physicians to confirm that the cryo-lesion is large enough to cover the solid tumor. Specifically, in a treatment of the prostatic cancer, preferred positions of thermocouples are in the posterior capsule and apex of the prostate gland to ensure the adequate freezing [48].

Another popular monitoring tool during cryosurgery is the ultrasonography. The intraoperative ultrasonography has sparked renewed interests in cryosurgery for visceral tumors. The ultrasonography guides the cryoprobe to place in targeted position and produces visualization of ice front during cryosurgery. It provides real-time images of the frozen volume and the possibility of marching the volume with the extent of the neoplasm. It has been widely applied in treatments of liver and prostate cancer [55-57]. The tissue in frozen state is black on the image as the detected region is hypoechoic. The ice front, in contrast, is hyperechoic. Therefore, it is displayed by a bright line in the monitoring screen. The difference is mainly due to the decrease of elasticity as the tissue turns into the frozen state [58]. The monitoring tool has been widely accepted with an excellent reliability of identifying the extent of tissue destruction [58, 59]. However, a major limitation of ultrasonography is that it is incapable to display the frozen in certain directions. Occasionally, the frozen volume is hidden by the posterior acoustic shadowing [48]. Considering the limitation, the technology has been improved as the three-dimensional ultrasonography, which compensates the lost details of the hidden volume [60]. However, owing to the displaying mechanism, the ultrasongraphy cannot display any information on temperatures. The temperatures in targeted area can only be estimated according to experience of physician.

Modem developments in monitoring instruments provide alternative options for cryosurgeons. These include the computerized tomography (CT) [61] and the magnetic resonance imaging (MRI) [62]. Although CT is not a real-time monitor, it produces a complete cross-section of tissue in frozen state. A series of images produced within a short period are still useful in monitoring the cryosurgical process. MRI, as a stronger monitoring tool, is capable to generate three-dimensional and real-time images of the frozen tissue.

12

Nevertheless, MRI requires more complex medical instruments associated with high costs.

In summary, the thermocouple and the ultrasonography are cost effective monitoring tools with acceptable accuracies while CT and MRI are costly techniques for monitoring. These tools have largely reduced the unsuccessful operations. However, all these monitoring instruments are not capable of providing three-dimensional and real-time temperature contours of the biological tissue. Therefore, the monitor-guided cryosurgery is often accompanied with the computational cryosurgery planning to optimize the surgical protocols.

2.3.   Mechanisms of tissue injury

The tissue injury starts to occur when the tissue temperature is beyond the range of normal body temperatures. The destructive effects occurring in cells during the freezing process are depicted schematically in Figure 2.1. The tissue injury at low temperatures can be categorized into two major mechanisms, direct cell injury and vascular injury. The cause of direct cell injury is mainly due to the immediate cell destruction in cooling and freezing process while the vascular injury may occur several hours upon the completion of a cryosurgery in the form of being vascular stasis. The relative importance of these two mechanisms has long debated in frostbite and that debate continues in relation to cryosurgical injury [51]. Nevertheless, the goal of cryosurgery is to maximize the deleterious effects of these mechanisms in the targeted region.
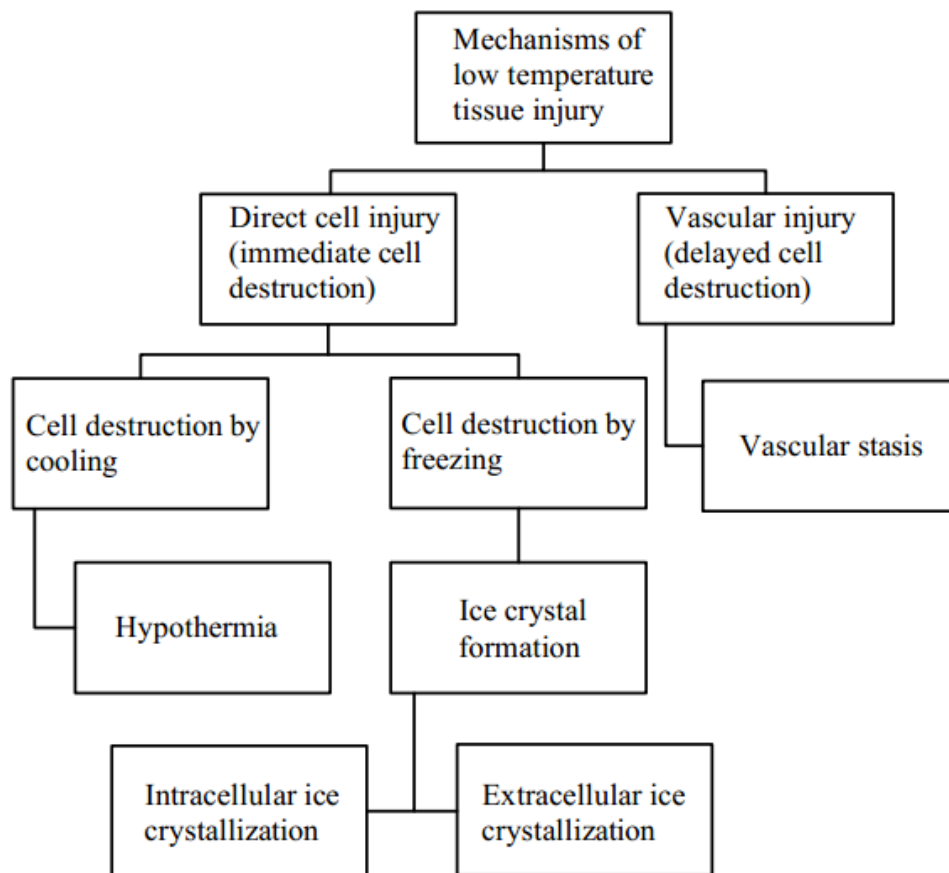
Figure 2.1 Flow chart on the mechanism of tissue destruction.

2.3.1. Direct cell injury

The direct cell injury is due deleterious effects of the cooling and thawing cycles on cells. It includes effects of hypothermia and ice crystal formation. Hypothermia is the initiation of the tissue injury due to low temperatures. Temperatures in the hypothermic range impede cell metabolism progressively. Hypothermia can lead to the cell death when the cooling duration is sufficiently long [63]. Gage claimed that the cell survival at 273 K was no more than a few days and even short exposure to nonfreezing temperature could kill cells [51]. It is apparent that hypothermia is not the major mechanism resulting in the tissue damage for cryosurgery, due to the time frame of the cryosurgery.

The ice crystal formation, under the category of direct cell injury, is an important mechanism of cryoinjury. It can be divided into the extracellular ice crystallization and intracellular ice crystallization. When the temperature falls into the freezing range of sub-zero to around 253 K, the ice crystal formation firstly occurs in the extracellular space [51] and this process is known as extracellular ice formation. As the process continues, extracellular ice crystals grow and the intracellular water seeps out the membrane due to the low osmotic potential developed in the extracellular region. As the process continues, ice crystals grow, cells shrink, and membranes and cell constituents are progressively damaged. With sufficient time, the high accumulation of electrolyte concentration is lethal to cells. However, this phenomenon, known as the solution-effect injury, does not always lead to complete cell annihilation. The other mechanism, the intracellular ice formation, is a serious threat to the cell viability. As the temperature further falls to 233 K or even lower, the formation of the intracellular ice occurs [36, 37]. The intracellular ice crystal formation is more likely to be generated by rapid cooling rates, freezing water before leaving cells [51]. The intracellular ice may propagate from one cell to another via intercellular channels [64]. Bischof et. al. has confirmed this result and claimed that there was a reduced resistance for propagation of freezing in tissue due to the vascular channels [65]. Once the intracellular ice is formed, the ice can permanently disrupt the internal cellular organelles and membranes.

An important clinical procedure to achieve immediate cell destruction is to thaw cells after the freezing. During the thawing process, as the temperature raises to the range from 233 K to 253 K [51], ice crystals fuse into large crystals. This is a disruptive process to cell membranes named as recrystallization. Meanwhile, water permeates into cells as the extracellular

15

environment is tentatively hypotonic. The enlarged cell volumes further propel ruptures of membranes. This mechanism explains the reason why the repetition of freeze-thaw cycles enhances the deleterious effects during cryosurgery.

2.3.2. Vascular stasis

The vascular stasis, under the classification of the delayed cell destruction, is a serious slowing or complete cessation of blood or lymph flow through vessels. The losses of circulation and cellular anoxia have been widely considered as a contribution to cryoinjury. The vascular stasis is the consequence of a series of changes in the circulation during the cryosurgical treatment. Numerous studies have demonstrated that the vascular changes are observed at the temperature range around 253 K [66-68]. When tissue is exposed to the cooling environment, the first response is the vasoconstriction with a reduction of blood flow. Further decrease in temperature may eventually cease the blood circulation. Edema, in contrast, develops and progresses in the following a few hours. Experiments disclosed that changes in capillary endothelial cells defecting endothelial cell junctions were observed about 2 hours after thawing [69, 70]. The endothelial injury leads to the incensement of the permeability of capillary wall, edema, platelet aggregation and microthrombus formation, resulting in the stagnation of the circulation in about 30-45 min [51]. Plenty of small blood vessels are completely occluded by thrombi 4 hours after thawing [51]. The loss of blood supply deprives cells of any possibility of survival with an uniform ablation of tissue, except at the boundary of previously frozen tissue [51].

2.3.3. Critical temperatures for tumor ablation

Many studies employ the isotherm at a critical temperature to identify the

complete ablation zone. This is a standard clinical procedure known as "critical isotherm protocol" [71]. It demarcates a region whereby the total cell death occurs when tissue temperature drops below the complete critical value. The critical temperature has been studied with a range from 271 K to 203 K [72, 73]. The most widely used value that induces the permanent injury is 233 K [36-42]. A brief summary of critical temperatures is shown in Table 2.1.

Table 2.1 Review on the critical temperatures

First Author	Cells/Tissue	Critical Temp.	Freeze-thaw program	Ref.
Gage	Osteocytes, bone, dog	271 K	5 min F–slow T	[72]
Gage	Melanocytes, skin, dog	269 K	4 min F–slow T	[74]
Smith	Liver, rat	258 K	3 min F–fast T	[75]
Rivoire	Liver, pig	258 K	5 min F–slow T	[76]
Lefebvre	Cheek pouch, hamster	255 K	1 min F-fast T	[68]
Dow	Prostate, dog	253 K	1 min F–slow T	[77]
Gage	Skin, dog	233 K	3 min F–slow T	[78]
Yamada	Skin, mouse	233 K	1 min F–slow T	[39]
Gage	Palate, dog	233 K	3 min F–slow T	[38]
Neel	Sarcoma, mouse	213 K	6 min F–slow T	[79]
Staren	Adenocarcinoma, rat	203 K	7 min F–slow T	[73]

Note: F: freezing; T: thawing

Nevertheless, the extremely low temperatures during cryosurgery bring a host of challenging problems, such as large magnitudes of post-surgical thermal stress and the protection of surrounding healthy tissue against the severe cryo-freezing. Therefore, reducing the degree of cryoinjury occurred in the healthy tissue is one of the key focuses in this dissertation.

2.3.4. Repetition of freeze-thaw cycles

It is of paramount importance to understand the connection between tissue cryo-freezing and the corresponding cell death mechanism to determine key controllable parameters that enable cryosurgeons to enhance the surgical success. It is generally believed that the intracellular ice plays an important role in cryoinjury by either electrical transient at the ice interface [80] or critical gradient in osmotic pressure across the membrane [49, 81]. To control and regulate the complete ablation zone, often demarcated at below 233 K [82], repeating several freeze-thaw cycles has been known to be an effective therapy [51, 83, 84]. However, the physical mechanism involving cell destruction during freeze-thaw cycles, particularly when freezing and peripheral thawing are executed to control and enhance the cryoablation, has not been covered in depth. Some studies define specific temperatures to demarcate the cellular status [51] while some apply freezing/cooling rates as the criteria for the cell ablation [9]. Though there are existing works that study the ablating mechanism involving a single freeze-thaw cycle, few have considered the biophysical implication of several freeze-thaw cycles on the overall quantitative cell damage.

2.4.   Shape factor of tumor profile

It is essential to investigate the shape factor of tumor profiles when tumors are associated with irregular boundaries. Many theoretical and applied disciplines have expressed legitimate interests in shape analysis [85-89]. However, it is not appropriate to extend this unique methodology to a wide array of applications [85]. Golston et. al. analyzed the border irregularity with an index termed "jaggedness" [87]. This method of detecting irregular border used the ratio of the square of the perimeter of a given shape to its corresponding area in order to obtain a size-independent measurement on irregularity [87]. However, there are significant challenges associated with the determination of the perimeter and area, which means that this method may not be applied to

solid tumors. In addition, results showed that the border detection algorithm managed to find a reasonably correct border in at most 60% of cases [87]. Claridge et al. studied malignant skin tumors and described the shape of the lesion by a parameter known as the "bulkiness" [88]. They claimed that a figure might be perceived as irregular if either its overall shape was irregular or it had an irregular border [88]. While the shape factor parameter that they proposed appropriately accounts for two-dimensional figures, it was unable to account for the invasive directions during cryosurgery. Other studies have used shape descriptors such as the compactness index (CI) [90, 91] or the fractal dimension (FD) [92] to measure border irregularity. Unfortunately, both these parameters have limitations - CI is sensitive to the irrelevant border information while FD does not measure structural irregularies [86]. Combing through available literatures, it is evident that although various studies have been carried out to investigate shape factor of figures, rare studies have effectively developed a three-dimensional parameter that comprehensively quantifies shape effects during cryosurgery.

The shape factor in cryosurgical planning is complex since it has to consider the surrounding biological environment. For example, the size of the parent organ, the blood flow in large vessels and the location of bones in the tumor's vicinity can significantly affect the invasive direction of cryoprobe. The shape factor in this study mainly focuses on the profile of the complete ablation. Conventional cryosurgery techniques need better ablating protocols that account for the morphology of the complete ablation zone. We propose a shape irregularity index that can be effectively applied to the cryosurgery.

The shape of the complete ablation generated by a conventional cryoprobe could be largely different from the tumor profile. To cover the irregularly shaped tumor, large amounts of nearby healthy tissue can be damaged. Several

studies have been carried out to resolve this bottleneck [13, 34, 93]. Multiprobe cryo-therapy is a common surgical procedure to produce irregular frozen tissue for large tumors. However, the primary concern of this procedure is determining the most effective allocation of cryoprobe. Rossi et al. utilizes a bubble packing method to predict the actual experimental cryoprobe location [34]. Recently, Chua introduces a piecewise method whereby the placement of probes is estimated by superimposing ice contours obtained under discrete conditions [94]. These above methods provide applicable results in planning the multiprobe allocation. However, the placement of cryoprobes is still an art held by cryosurgeons, requiring careful consideration when deciding the correct number and position of the cryoprobes prior to the procedure [35].

2.5. Heating of large blood flows and metabolism

Anatomically, tumors are often situated close to or embedded with large blood vessels. This is mainly because that the growth of a tumor ultimately relies on nutrients supplied by the surrounding blood network. The blood flow inside the blood network represents a heat source to the nearby frozen tissues and thereby limits freezing lesions during cryosurgery. This may result in inadequate cooling temperatures and lead to tumor recurrence after treatment. In view of this, it is necessary to understand the effects of branched blood network on the temperature responses of tissues subjected to control freezing. This was also shown by Berger et. al. with a conclusion that tumor cells in the vicinity of large blood vessels were often correlated with tumor recurrence after treatment [3]. Many analytical models have been formulated to simulate the heat transfer in biotissue [9, 26, 28, 95, 96]. However, a major limitation of most of these model is that they did not consider the inhomogeneous and anisotropic nature of blood vessels and their thermal impacts, especially large vessels [4, 20, 33].

The functionality of the blood circulatory system largely depends on its structure and arrangement. In consideration of blood vessels heat contribution, the vascular network of simplified fractal-like branching has been studied [25, 27, 32, 33]. Parameters in the fractal tree model, such as branch level, diameter, branch number and branch angle, are required to be defined so the fractal-like blood vessel trees can be constructed. Often than not, such a simplistic model compromises the accuracy of temperature contours because the defined vessel tree cannot match perfectly with real blood network. The locations of large vessels at the lower levels of vessel tree are tedious to determine. The improper blood vessel allocation in the model can produce misleading results. A recent work has noted this inadequacy and even claimed that without sufficient consideration of large blood vessels, the cryosurgical treatment on tumors embedded with or close to large vessels may turn out to be a failure[20]. Though many works have been carried out to investigate freezing process, the study of temperature profiles, in the presence of dominant vascularized blood flow has yet to be indepthly pursued. There is no common ground for the cryosurgical planning with the consideration of vascular network. In view of this, it is important to investigate the thermal impact of large vessels on the thermal development of tissue subjected to freezing.

Besides the vascular heating effect, the metabolism is another consideration in bioheat transfer. Metabolism is a set of chemical reactions that occur in living organisms. The metabolic rate varies with physiological activities and body mass. The metabolic heat generation is a function of local tissue temperature [97]. However, for the simplicity of analysis, the rate of heat production can be considered as a constant [30, 98] or even neglected compared to the heating effect of blood perfusion [35, 99].

21

2.6. Radiofrequency ablation

One of the most significant merits for cryoablation is the minimal invasive nature associated with short hospital stays. Compared to cryoablation, RF ablation also has been widely used as the focal ablative technique. It provides an alternative surgical option for the ablation of tumors. RF ablation utilizes alternating current (AC), typically around 500 kHz [100], to deliver therapeutic energy into soft tissues. This frequency range is high enough to prevent the induction of ventricular fibrillation [101]. The energy delivery is accomplished by passing RF current from the RF electrode, through the intervening tissue, to the ground pad. As RF current is alternating, there is no constant cathode or anode during the RF energy delivery. The passage of current through the tissue results in the electromagnetic heating, which is termed as resistive or ohmic heating [101]. The tissue resistance converts the electrical energy into thermal energy via the molecular agitation. The thermal energy is further transferred into the adjacent tissue by heat conduction (i.e. solid tissue) and heat convection (i.e. blood flows and solid tissue). A coagulative ablation zone around electrodes can be formed when temperatures are above certain range. The intent of RF ablation is to thermally necrose the tissue to cover the profile of tumor by raising targeted tissue temperatures for a period of 10-15 min [102, 103].
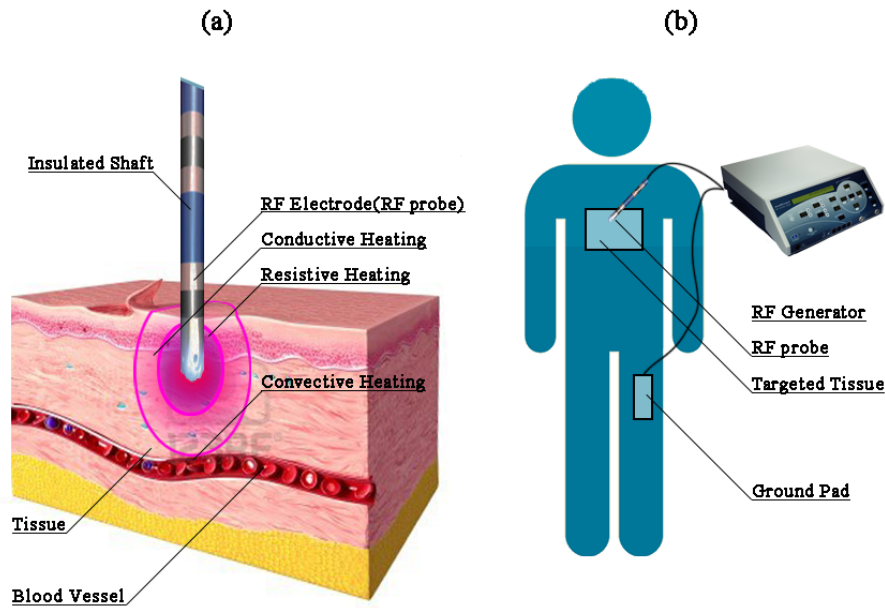
Figure 2.2 Description of RF ablation. (a) a cross-sectional view of the resistive heating, conductive heating and convective heating during RF ablation; (b) major components of a typical RF ablation system.

Figure 2.2 shows the schematic representation of RF ablation. Figure 2.2 (a) demonstrates the cross-sectional view of the tissue occurring resistive heating, conductive heating and convective heating during RF ablation. When the RF probe delivers RF currents, the tissue nearby the RF probe is exposed to high current densities [103]. Consequently, the current density induces the most resistive heating within this narrow rim of tissue. Tissue heating beyond this region occurs because of passive heat conduction/convection from the high temperature region. The temperature can induce the protein coagulation and form a complete ablation zone. Figure 2.2 (b) shows the components in a typical RF ablation system. To form a return circuit, the ground pad is pasted to the skin of patient. The RF generator provides the RF current to the RF probe. The RF probe is typically made of stainless steel, platinum or Ni-Ti alloys. The inactive portion of the RF probe, also known as the insulated shaft, is usually insulated electrically to reduce the undesirable heat generation. The active portion of RF probe delivers RF current into the targeted tissue.

The downsides of RF ablation include the chemical reaction, stimulation of tissue and the complication of skin burns [104]. Besides of these drawbacks, a major limitation of percutaneous single RF probe is the inability to produce a large ablation zone to cover large tumors. This is because that the large RF power induces the undesirable skin burns. To enhance the performance, internally cooled probes in RF ablation has facilitated remarkable progress in obtaining larger ablation zones [105]. Inside the shaft of the internally cooled probe, there are dual channels through which distilled water under room temperature is pumped by a peristaltic pump, continuously cooling the shaft proximal to the radiating segment. The internally cooled probes can effectively prevent overheating of the shaft. Therefore, the high RF power and temperature can be taken to spread the lesion size.

Albeit the performance of RF probe has been improved, there are still much room to develop novel RF ablation devices and operating protocols to promote the surgical success. Ritz et. al. developed a novel bipolar RF ablation device combined with hepatic blood flow interruption by Pringle maneuver [105]. The internally cooled bipolar RF probe was incorporated with two electrodes on the probe. They claimed that bipolar unit did not require the use of the grounding pad and the RF ablation was conducted with a reduced cooling effect of blood flow [105]. Claire et. al. developed a helical coil designed to be located inside a tumor to deliver radiofrequency energy at 27.12 MHz [106]. The benefit of this design exploited the size and the uniformity of the electric field generated by magnetic induction inside this solenoidal geometry [106]. Furthermore, Schutt and Haemmerich built numerical models to study the multiple electrodes within a straight RF probe [107]. They segmented the ground pads and investigated on the sequential activation of the ground electrodes. They claimed that the method might reduce the incidence of ground pad burns and enabled the use of higher power generators during RF

tumor ablation [107]. Recently, Stoffner et. al. experimentally tested the multi-polar RF ablation and they concluded that 4-6 applicators were feasible in forming the lesion while 3 applicators could be ablated consecutively for small tumors [108]. All these articles provided applicable results and were effective in the treatment of certain types of tumors.

The efficacies of RF ablation and cryosurgery are difficult to compare because most reports are concluded from different selection criteria, different treatment protocols and even different types of tumors. Therefore, there are very few studies focused on the exact evaluation of these two technologies. Articles examining these two ablative therapies are often associated with the long-term and statistical results. Joosten et. al., for example, specifically compared long-term feedback of cryoablation and RF ablation [8]. They concluded that there was no significant difference in survival between both treatment modalities [8]. 2-year survival rates were observed to be 61 % and 75 % for cryoablation and RF therapy, respectively [8]. The figures corresponded well with some other work specifically focused on cryoablation or RF therapy. Studies indicated that the overall 2-year survival rate for cryoablation varied from 52 % to 78 % [109-111] while the rate for RF ablation ranged from 50% to 69% [112-114].

The aim of this study is to gain an insightful knowledge on the RF and cryoablation processes and promote the efficacy of tumor ablation. In this dissertation, the mathematical modeling of RF ablation has been developed, coupling of the electrical-thermal conduction with the heat advection by means of the blood flow. Besides, the model considers the variance of the electrical conductivities in response to temperature. It is calculated to test the thermal influence of a single RF probe and a multi-tine RF probe in porcine livers. The RF ablation has been incorporated into a cryosurgical process to

simulate the performance of a proposed RF-assisted cryoprobe. A set of experiments have been designed to disclose the thermal influence of the hybrid system.

Chapter 3: Mathematical Formulation

This chapter develops mathematical models to analyze and simulate the bioheat transfer in biological tissue. A brief introduction of bioheat transfer models is given. Based on these models, we develop and present the models used in this dissertation. The cryo-freezing model has been developed when large blood vessels are presented. Then, the RF-generated heating model is illustrated to facilitate the RF simulation. Furthermore, the methodology of orthogonal experiment design is applied to reduce the number of tests. Lastly, the tissue damage function is developed for the analysis of tissue damage in both heating and freezing conditions.

3.1. Developing bioheat model

The bioheat transfer process during cryosurgery has been a topic of interest for numerous physiologists, physicans, and engineers [9, 26, 28, 95]. The early bioheat transfer models are quantified by the product of a thermal conductance and a measured temperature gradient between the tissue and the surroundings [115, 116]. This approach involves the heat transfer from the body to the surrounding based on the radiative, convective and evaporative conductances with the environment and the temperature difference between the skin and surroundings. Most conductances are constant physical properties. Afterwards, the most famous quantitative relationship in the bioheat transfer, named with the Pennes model, was published in 1948 on a continuum basis [30]. This groundbreaking paper has been cited in almost all articles related to the bioheat transfer. It has been widely applied in many numerical studies [30, 117]. His work is the quantitative foundation in the field of bioheat transfer. It can be expressed in Eq.(3.1) when the axial gradient in the tissue temperature

along the length of the limb is negligible.

$$\rho_t C_t \frac{\partial T_t}{\partial t} = \frac{k}{r} \frac{\partial}{\partial r}\left(r \frac{\partial T_t}{\partial r}\right) + \omega \rho_{bl} C_{bl}(T_{ar,in} - T_t) + Q_m \qquad (3.1)$$

The heat source of perfusion term is shown as the second term on the right-hand side of Eq.(3.1). This term essentially assumes that blood enters the smallest vessels of the microcirculation at temperature $T_{ar,in}$. As the blood flow leaves vessels, it has undergone complete thermal equilibration with the surrounding tissue at temperature T_t.

3.1.1. Model assumptions

A bioheat transfer model has been formulated to study the cryo-freezing. The proposed model provides a customized cryosurgical plan for surgeons when large blood vessels are presented. To reduce the complexity of the model, several assumptions are made as below,

(a). Physical and thermal properties in biological tissue are uniform and isotropic. The differences in thermal properties between cancerous and healthy tissues are negligible.

(b). Variance of blood rheology is negligible.

(c). Blood flows in large vessels are incompressible fluid.

(d). Variation of blood flow rate variation due to periodic heartbeat is negligible.

(e). Heat sources due to the blood perfusion and metabolism are present when tissue are in unfrozen zone.

(f). Liquidus and solidus tissue temperatures are 272 K and 265 K, respectively [118].

3.1.2. Governing equations
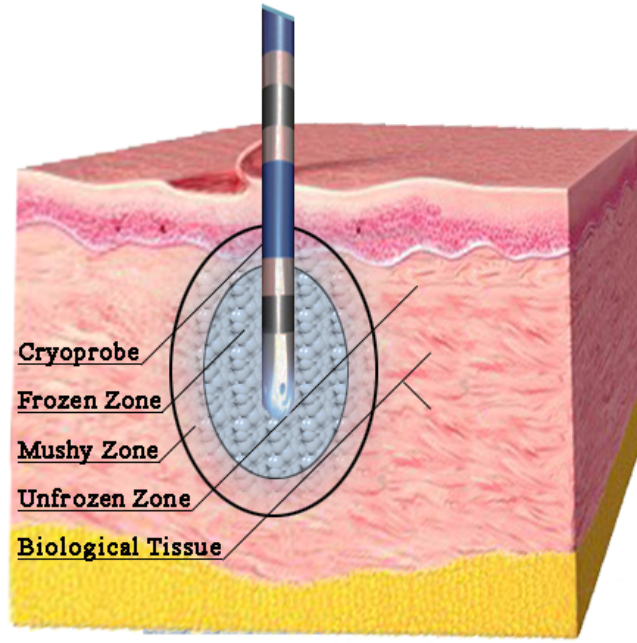
Figure 3.1 Physical demarcation of the biological tissue during a cryosurgical process.

The bioheat transfer equations are based on the demarcation of the biological tissue as shown in Figure 3.1. The biological tissue is divided into a frozen zone, a mushy zone and unfrozen zone.

(a). The energy equation in the frozen tissue can be simplified due to the absent of the blood perfusion and the metabolism as shown in Eq.(3.2).

$$\rho_{t,a} C_{t,a} \frac{\partial T_{t,a}(X,t)}{\partial t} = \nabla k_{t,a} \nabla T_{t,a}(X,t), \text{ where } X \in \Pi(t) \qquad (3.2)$$

(b). In the mushy zone, the energy equation can be written as

$$\rho_{t,b} C_{t,b} \frac{\partial T_{t,b}(X,t)}{\partial t} = \nabla k_{t,b} \nabla T_{t,b}(X,t)$$
$$+ \omega_b \rho_{t,b} c_b (T_{bl} - T_{t,c}(X,t)) + \rho_{t,b} h_{L,t} \frac{df_s}{dt}, \text{ where } X \in \Lambda(t) \qquad (3.3)$$

where f_s is the solid faction in phase change which can be developed as

$$f_s = 0, \text{ if } \quad T_{t,b}(X,t) = T_{liquidus} \qquad (3.4)$$

$$f_s = 1, \text{ if } \quad T_{t,b}(X,t) = T_{solidus} \qquad (3.5)$$

$$f_s = \frac{T_{t,b}(X,t) - T_{liquidus}}{T_{solidus} - T_{liquidus}}, \; if \; T_{t,b}(X,t) \in (T_{solidus}, T_{liquidus}) \tag{3.6}$$

When the temperature difference between T_{bl} and $T_{t,c}$ in the mushy zone is minimal, Eq. (3.3) can be simplified as shown in the Eq. (3.7).

$$\rho_{t,b} C_{t,b} \frac{\partial T_{t,b}(X,t)}{\partial t} = \nabla k_{t,b} \nabla T_{t,b}(X,t) + \rho_{t,b} h_{L,t} \frac{df_s}{dt}, \; where \; X \in \Lambda(t)$$

$$\tag{3.7}$$

(c). In the unfrozen zone, the energy equation is expressed as

$$\begin{aligned} \rho_{t,c} C_{t,c} \frac{\partial T_{t,c}(X,t)}{\partial t} &= \nabla k_{t,c} \nabla T_{t,c}(X,t) \\ &+ \omega_b \rho_{t,c} C_b (T_{bl} - T_{t,c}(X,t)) + Q_m \end{aligned}, \; where \; X \in \Gamma(t) \tag{3.8}$$

It is noteworthy that three physical zones $\Pi(t)$, $\Lambda(t)$ and $\Gamma(t)$ are demarcated with T_a and T_c.

(d). The governing equation of the cryoprobe complies with the settings in experiments and it can be expressed in Eq.(3.9). The temperature of the cryoprobe is governed by $\Phi(T_p)$ at the commencement of the freezing. It approaches to the stable temperature after several minutes.

$$T_{p,fr}(t) = \begin{cases} \Phi_f(t), & t \in [t_{p,ini,fc}, \; t_{p,stable,fc}] \\ T_{p,s,fc}, & t \in [t_{p,stable,fc}, \; t_{p,end,fc}] \end{cases}$$

$$\tag{3.9}$$

3.1.3. Boundary conditions

Boundary conditions are implemented at the demarcation of the different zones. Starting from the interface between the frozen and mushy region, we have

$$T_{t,a}(X,t) = T_{t,b}(X,t) = T_{solidus}, \quad X \in (\Pi \cap \Lambda) \tag{3.10}$$

$$k_{t,a} \nabla T_{t,a}(X,t) \cdot \hat{n} = k_{t,b} \nabla T_{t,b}(X,t) \cdot \hat{n}, \quad X \in (\Pi \cap \Lambda) \tag{3.11}$$

Eq.(3.10) conveys that temperatures at the two sides of the interface are the same while Eq.(3.11) illustrates that the heat flow is constant across the interface. In the same light, the boundary conditions at the interface between the mushy and unfrozen zone can be expressed as,

$$T_{t,b}(X,t) = T_{t,c}(X,t) = T_{liquidus}, \quad X \in (\Lambda \cap \Gamma) \tag{3.12}$$

$$k_{t,b} \nabla T_{t,b}(X,t) \cdot \hat{n} = k_{t,c} \nabla T_{t,c}(X,t) \cdot \hat{n}, \quad X \in (\Lambda \cap \Gamma) \tag{3.13}$$

3.1.4. Blood flow in large vessels

The previous bioheat transfer model in unfrozen tissue can be modified to study the thermal influence due to the complex blood flow system. The blood perfusion term in Eq.(3.8) should be reevaluated when equations in Section 3.1.4 are employed in simulations.

To simplify the simulation on the extracted-vascular network in this dissertation, a two-dimensional model was formulated. The governing equation of blood flow is given in a two-dimensional form in Eq.(3.14).

$$\rho_{bf} C_{bf} \frac{\partial T_{bf}}{\partial t} + \rho_{bf} C_{bf} u \frac{\partial T_{bf}}{\partial x} + \rho_{bf} C_{bf} v \frac{\partial T_{bf}}{\partial y} = k_{bf} \nabla^2 T_{bf} + Q_{bf} \tag{3.14}$$

The continuity is given in Eq.(3.15) and momentum equations of blood flow are shown in Eq.(3.16) and Eq.(3.17), respectively.

$$\frac{\partial \rho_{bf}}{\partial t} + \rho_{bf} \left(\frac{\partial u}{\partial x} + \frac{\partial v}{\partial y} \right) = 0 \tag{3.15}$$

$$\rho_{bf} \left(\frac{\partial u}{\partial t} + \nabla(u\tilde{u}) \right) = -\frac{\partial P}{\partial x} + \mu\left(\nabla^2 u\right) + S_{Mx} \tag{3.16}$$

$$\rho_{bf} \left(\frac{\partial v}{\partial t} + \nabla(v\tilde{u}) \right) = -\frac{\partial P}{\partial y} + \mu\left(\nabla^2 v\right) + S_{My} \tag{3.17}$$

By introducing a general variable φ for momentum equations, a new expression based on the above equations can be coined in the following form.

$$\rho_b \left(\frac{\partial \varphi}{\partial t} + \nabla (\varphi \tilde{u}) \right) = \mu (\nabla^2 \varphi) + S_\varphi \qquad (3.18)$$

The first term on the left side of the equation is the rate of increase of φ while the second term on the left is the net rate of flow of φ out of fluid element. The first term on the right side is the rate of change of φ due to diffusion while the last term in the equation relates to the rate of change of φ due to heat sources.

3.2. Radiofrequency-generated heating

3.2.1 Governing equations of RF ablation

The RF ablation is initiated by the high frequency alternating voltage applied to the electrically conductive ablation probe [100]. With the frequency (around 500 kHz [100]), the wavelength is calculated around 600 m. Considering the inter-polar distance is in order of a few centimeters, the wavelength of RF current is thus two to four orders of magnitude longer than inter-polar distance. Consequently, the ablation probe dissipates the majority of the energy via electrical conduction other than capacitive coupling [119]. The field is solved by using the generalized Laplace equation [120].

$$\nabla [\sigma(t)\nabla V] = 0 \qquad (3.19)$$

When $\sigma(t)$ is independent of space, the governing equation is simplified as:

$$\nabla^2 (V) = 0 \qquad (3.20)$$

The detail expression of the operator ∇^2 is shown in Eq.(3.20) as follows:

$$div(grad(V)) = 0 \qquad (3.21)$$

The Eq.(3.21) shows that the electrical potential is independent of temperature. Heat transfer in tissue is governed by the heat conduction

$$\rho_{t,c} C_{t,c} \frac{\partial T_{t,c}(X,t)}{\partial t} = \nabla(k_{t,c}\nabla T_{t,c}(X,t)) + \mathbf{j} \cdot \mathbf{E}_f +$$
$$\omega_b \rho_{t,c} C_b (T_{bl} - T_{t,c}(X,t)) + Q_m \qquad (3.22)$$

where the electricity field density $\boldsymbol{E_f}$ is equal to the negative gradient of the

potential V:

$$\mathrm{E}_f = -grad(V) = -\nabla V$$

(3.23)

and the current density j is related to the electric field density by

$$j = \mathrm{E}_f / \sigma$$

(3.24)

Therefore, the Eq.(3.22) can be written in the following format:

$$\rho_{t,c} C_{t,c} \frac{\partial T_{t,c}(X,t)}{\partial t} = \nabla(k_{t,c} \nabla T_{t,c}(X,t)) + \frac{|\nabla V|^2}{\sigma(T_{t,c})} \\ + \omega_b \rho_{t,c} C_b (T_{bl} - T_{t,c}(X,t)) + Q_m$$

(3.25)

The electric potential in Eq.(3.25) must be coupled because the electric parameters vary in function of temperature. In other words, the temperature variation leads to the change in the electric parameters which results in the change of electric potential.

The simulations are conducted with finite element method, which is based on weak forms of partial differential equations. The weak forms of equations have been widely used. As the focus of this numerical study, we do not elaborate details of the weak form equations. Interested readers can refer to the reference for details [119]. The governing equations related to the cryo-freezing model are formulated in the previous section.

3.2.2 Electrical conductivity

There are no formal experimental measurements on the temperature-dependence of the electrical conductivity of liver [103]. Many numerical studies assume that the temperature-dependent behavior of liver tissue is similar to that of an equivalent sodium chloride solution [100, 103]. Stogryn has derived expressions for the conductivity of sodium chloride solution at given temperature (T) and normality (Nor) [121] as

$$\sigma(T, Nor) = \sigma(25, Nor)[1.000 - 1.962 \times 10^{-2} \Delta$$
$$+ 8.08 \times 10^{-5} \Delta^2 - \Delta Nor \{3.020 \times 10^{-5} + 3.922 \times 10^{-5} \Delta$$
$$+ Nor(1.721 \times 10^{-5} - 6.584 \times 10^{-6} \Delta)\}$$

$$(3.26)$$

where
$$\sigma(25, Nor) = Nor[10.394 - 2.3776 Nor + 0.68258 Nor^2)$$
$$- 0.13538 Nor^3 + 1.0086 \times 10^{-2} Nor^4]$$

and Δ=298.15-T. Nor must be determined as to obtain the relation between T and σ. temperature The Nor of physiological $NaCl$ solution is $Nor \approx 0.105$ [100]. Therefore, the temperature-dependent electrical conductivity of liver can be obtained.

3.2.3 Numerical simulation of one-tine and multi-tine RF ablation
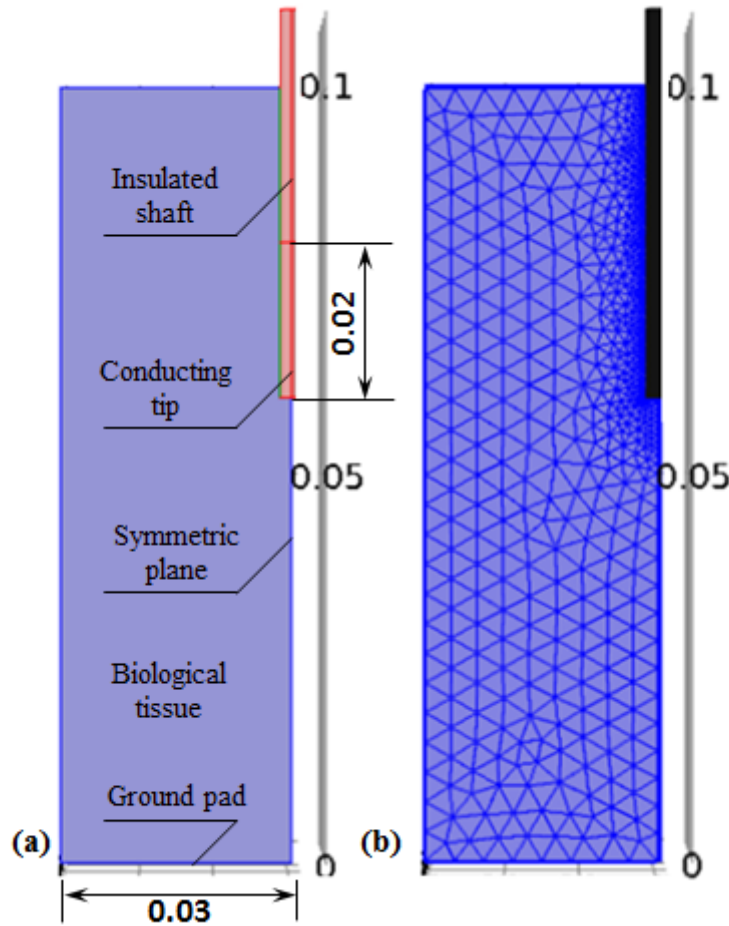
Figure 3.2 Symmetric model geometry of a single RF probe ablation. (a) dimension of the one-tine RF probe in tissue; (b) corresponding finite element mesh containing 29462 elements.

Figure 3.2 (a) shows a symmetric diagram of a three-dimensional single RF ablation that is typically involved clinical practice. The active portion of the probe is embedded into a 60 mm × 60 mm × 100 mm cubic region that simulates the tissue surrounding. Previous study has observed that temperature distribution is symmetric between the two sides of electrode during RF ablation [122]. Therefore, only half of simulation domain is computed. The distal 20 mm of the electrode is an electrically conductive metal (i.e. stainless steel) while the rest portion is covered with an electrically insulating material. The diameter of the electrode is 2 mm. The bottom surface is set as the ground pad with a constant voltage of 0 V.

Figure 3.2(b) shows the divided meshes that implemented during the simulation. Only a quarter of the total domain was simulated with 29462 elements. The mesh elements close to the RF probe were refined to improve the thermal resolution and model accuracy.
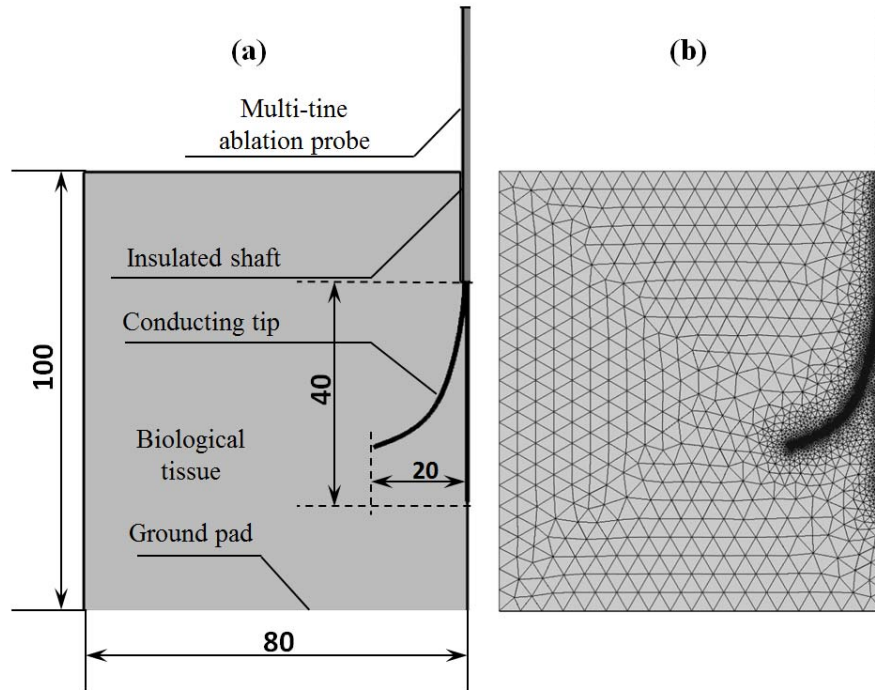
Figure 3.3 Symmetric model geometry of a multi-tine RF probe. (a) dimensions of the

multi-tine probe and biological tissue; (b) corresponding mesh for finite element model. Unit: mm.

The multi-tine RF probe is commonly used in the treatment of large tumors. Figure 3.3 (a) shows a symmetric diagram of a three-dimensional multi-tine ablation during RF ablation. The RF probe is embedded into a 160 mm × 160 mm × 100 mm cubic region that simulates biological tissue. The distal 40 mm of this RF probe is an electrically conductive metal to transfer the alternative current. The RF probe has 9 multiple tines that can be deployed at the tip. One tine is at the central and the rest tines are equally distributed at the surrounding. The largest distance between the central electrode and the surrounding electrode are 20 mm. We will further discuss the multi-tine RF probe in Section 4.2.5. Figure 3.3 (b) shows only a quarter of the cubic domain was simulated with 53106 elements.

3.3. Orthogonal experiment analysis

The advantage of orthogonal experiment design is that it only employs a fraction of all possible combinations. In an orthogonal experiment design, the setting of parameters involves allocating quantitative levels by using an orthogonal array [123]. It has been widely used in many experimental studies [124-128]. Parameters are referred to as "factors" and all variables are converted into discrete "levels". Matrices are built with each column representing a factor and each row standing for a combination of factor levels. Thus, experiments conducted using this selection are also labeled as matrix experiments [129]. Orthogonal arrays are usually denoted by $L_N(l^k)$, where N represents for the number of performed experiments, l is the number of levels per factor and k is the number of factors.

Our experimental test involves three factors at three different settings. Pressure, flow rate and liquid level of freezing medium are identified as three important

influencing factors in the orthogonal experiment design. A complete factorial test requires 27 experiments while the orthogonal experiment reduces the number to 9. Three factors (pressure, flow rate and nitrogen liquid level) were chosen to form $L_9(3^3)$ matrix (l=3, k^*=3). According to $L_9(3^3)$ design, 9 experiments were carried out. The minimum temperature and initial freezing of the different combinations can be obtained via experiments. The initial freezing refers the duration that the cryoprobe needs to reach the lowest temperature. The lowest temperature is denoted as $Y^{(1)}_{A,B,C}$, while the initial freezing is expressed as $Y^{(2)}_{A,B,C}$, where A, B, C are the selected factors, representing for pressure, flow rate and liquid level.

Sum of the evaluation indexes of different factors at all levels can be calculated according to the orthogonal array. Briefly, we illustrate the evaluation of factor A as an example. The sum of the evaluation index of factor A at factor level 1 to 3 were calculated as follows:

$$F^{(1)}_{1,A} = Y^{(1)}_{A1,B1,C1} + Y^{(1)}_{A1,B2,C2} + Y^{(1)}_{A1,B3,C3} \tag{3.27}$$

$$F^{(1)}_{2,A} = Y^{(1)}_{A2,B1,C2} + Y^{(1)}_{A2,B2,C3} + Y^{(1)}_{A1,B3,C1} \tag{3.28}$$

$$F^{(1)}_{3,A} = Y^{(1)}_{A3,B1,C3} + Y^{(1)}_{A3,B2,C1} + Y^{(1)}_{A3,B3,C2} \tag{3.29}$$

The mean value of the evaluation index of factor A at level 1 to the target function 1 ($\bar{f}^{(1)}_{1,A}$) can be calculated by $\bar{f}^{(1)}_{1,A} = F^{(1)}_{1,A}/l$. The range value is defined as

$$R(x_l) = (\bar{f}^{(A)}_{max} - \bar{f}^{(A)}_{min}) \tag{3.30}$$

where $\bar{f}^{(A)}_{max} = \max\{\bar{f}^{(1)}_{1,A},\ldots,\bar{f}^{(1)}_{l,A}\}$ and $\bar{f}^{(A)}_{min} = \min\{\bar{f}^{(1)}_{1,A},\ldots,\bar{f}^{(1)}_{l,A}\}$. The contribution ratio is defined as the ratio of the R value of each factor to the total R value [127]. Thus, the contribution ratio of each parameter to the target function of the minimum temperature and initial freezing can be obtained.

3.4.   Damage function of thermal injury

To realize greater cryoablation success, several repeatable freeze-thaw cycles are often employed [37]. Cellular damage is an accumulation of different reactions and denaturation of chromosomal proteins [9, 130]. Temperature is a key parameter which quantifies the degree of cellular tissue damage. Other contributing factors include post-thaw vascular injury characterized by stasis, thrombosis and increased vascular permeability [131]. The protein denaturation follows the *Arrhenius function* [132-134] given as:

$$D_s = \gamma T P_k^{-1} e^{-\Delta G / RT} \tag{3.31}$$

The universal form of this equation can be expressed in terms of a pre-exponential factor ε and activation energy E_a and is re-written as

$$D_s = \varepsilon e^{-E_a / RT} \tag{3.32}$$

Thus far, there is no common consensus among researchers on the best damage function of thermal therapy. However, it is reasonable to believe the cell damage rate is markedly dependent on the localized tissue temperature [49]. A standard clinical procedure, known as the critical isotherm protocol, assumes that the complete ablation occurs within the threshold tissue temperature [71]. Damage functions for freezing cycle and thawing cycle are proposed as:

$$D_{s,freezing}^n = \begin{cases} \varepsilon_2 e^{\alpha T} + \varepsilon_3 e^{\kappa T}, & T \in [T_{fc}^*, \ T_1^*) \\ 1, & T \in [-\infty, \ T_{fc}^*) \end{cases} \tag{3.33}$$

$$D_{s,thaw}^n = \begin{cases} 1, & T \in (T_{tc}^*, \ \infty) \\ \varepsilon_1 e^{-E_{a,tc}/RT}, & T \in [T_2^*, \ T_{tc}^*) \\ 0, & T \in [T_1^*, \ T_2^*) \end{cases} \tag{3.34}$$

Eq. (3.33) shows the damage function in the freezing cycle. The damage rate is 1 when the temperature drops below the critical value T_{fc}^*. When the temperature is in range between T_{fc}^* and T_1^*, the damage function is determined by exponents with ε_2 and ε_3. Increasing temperature around body

temperatures in range of T^*_1 and T^*_2, thermal damage is considered to be zero. Further temperature raise generates heating damage in Eq. (3.34) according to the *Arrhenius function.*

One freeze-thaw cycle contains a cryo-freezing process followed by a thawing process. The probability of the survived tissue after the first freezing process can be explained as ($1-D^n_{s,freezing}$). The probability of survived tissue after the first freeze-thaw cycle can be explained by $[(1-D^1_{s,freezing})(1-D^1_{s,thawing})]^{\tau_1}$. τ_1 is the factor for a combined freeze-thaw cycle. The damage function for the n freeze-thaw cycle is shown as

$$D^n_s = 1 - [(1 - D^n_{s,freezing})(1 - D^n_{s,thawing})]^{\tau_1} \qquad (3.35)$$

Accumulating damage within all freeze-thaw cycles, the overall damage function for *n* cycles can be described by

$$D^n_s = [1 - (1 - D^1_s)(1 - D^2_s)(1 - D^3_s)\cdots(1 - D^n_s)]^{\tau_2} \qquad (3.36)$$

Chapter 4: Experimental Facility and Procedure

4.1. Experimental setup and measurements

This chapter describes major experimental facilities, measurements, operating procedures and uncertainties of experiments. A series of experiments have been conducted with topics on the performance of a conventional cryosurgical system, effects of crucial parameters during cryosurgery, generation of irregularly shaped ablation zones, bioheat transfer in large vascular tissue and incorporation of the peripheral Joule heating and RF-generated heating. The uncertainties of the measurements are given. The experiments are designed to enhance the feasibility and efficacy of cryosurgery. The experimental results lay the foundation for the cryosurgical planning.

4.1.1. Cryoprobe

The schematic diagram of the cryoprobe is shown in Figure 4.1. The cryoprobe usually contains a coaxial inner tube. The downstream of the inner tube is a small chamber enclosed within the cryoprobe, preventing the direct interaction between freezing medium and tissue. When the pressurized liquid freezing medium passes through the inner tube, the medium vaporizes at the small chamber. The gas-liquid flow streams back through an interlayer between the inner tube and the wall of insulation.
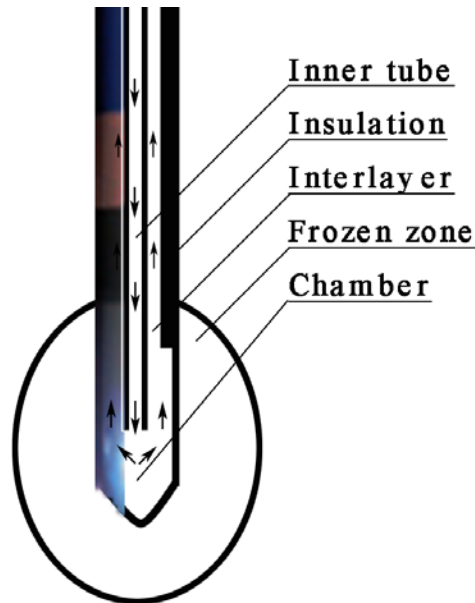
Figure 4.1 Schematic diagram of a conventional cryoprobe.

A series of lab-designed cryoprobes have been produced. The diameters are in the range between 4 mm and 12 mm. Each of cryoprobe has two ports: one inlet and one outlet. The inlet is connected to the homocentric inner steel tube, while the outlet is connected to the interlayer. The process of freezing during cryosurgery is characterized by the application of a cryoprobe and the propagation of the freezing interface from the outer surface of the probe to the interior of the tissue in the direction of temperature gradients.

4.1.2. Bifurcate cryoprobe

Multiple-probe approach is currently a primary cryosurgical solution to adapt the tumors in irregular shapes [94]. However, with the increased number of multiple probes, new challenges have to be taken into considerations, such as the additional incisive trauma, complex cryosurgical planning and accurate allocation of probes. To provide an integrated solution, we have proposed a novel cryo-device called as a bifurcate cryoprobe. Compared to the conventional cryoprobe, the bifurcate cryoprobe is capable of transforming its profile and producing irregularly shaped cryoinjury.
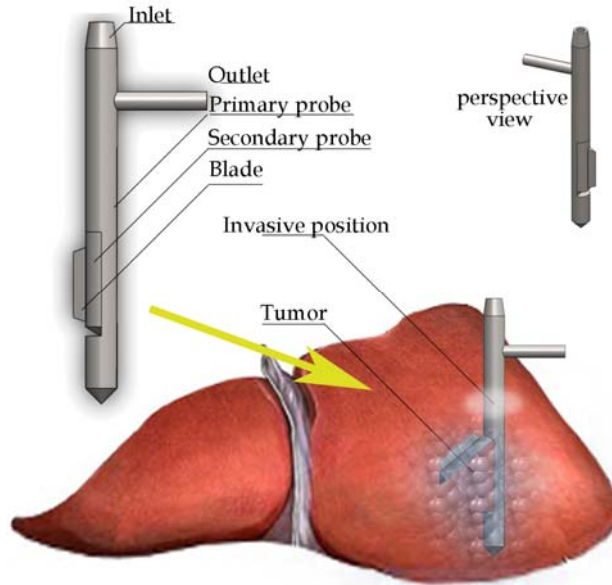
Figure 4.2 Components and application of a bifurcate cryoprobe.

Our proposed bifurcate cryoprobes employ freezing mechanism similar as that of conventional cryoprobes. However, the bifurcate cryoprobe incorporates a supplementary secondary probe in order to produce irregularly shaped freezing zones. Figure 4.2 shows the main components and the perspective view of the bifurcate cryoprobe. The secondary probe has the capability to regulate its position and hence enables the bifurcate cryoprobe to change its overall shape profile. For example, the junction can be made of shape changing material such as shape memory alloy NiTi. The alloy changes from austenite (at 310 K) to martensite (from 208 K to 77 K) upon cooling [135]. In addition, the tube, made of NiTi, is known to be capable of generating a large rotation bending [136]. The performance of a shape-changing NiTi tube has been reported in a recent work [136]. The bending feature of the NiTi tube would provide the secondary probe to regulate its angular motion according to the temperature. In the room temperature, the primary probe and the secondary probe are designed to adhere closely so that the bifurcate cryoprobe can seamlessly insert into tissue. When temperature drops to the predetermined range, the secondary probe is reformed. The reformation of internal structure can be shown in Figure 4.3.
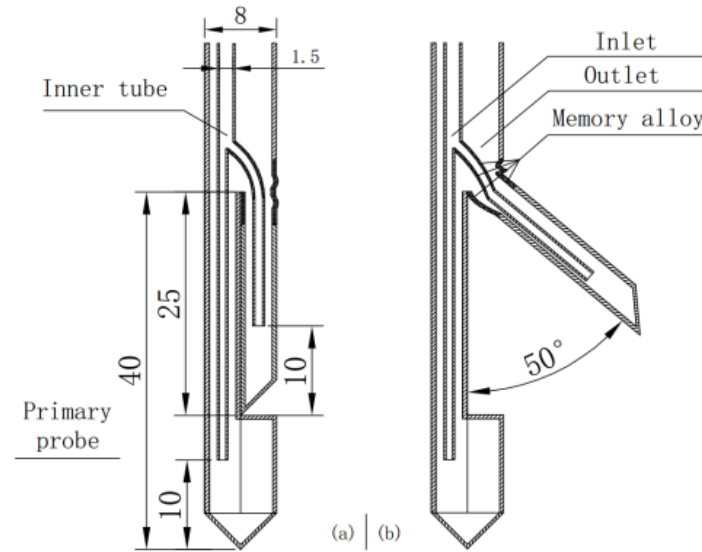
Figure 4.3 Inner structure of the bifurcate cryoprobe. (a) folded status;
(b) open status.

A representative bifurcate probe can comprise an inner cooling tube with two open ends, positioned within the exterior wall of the cryoprobe. Preferably, the inactive portion bifurcate cryoprobe is formed to have a low thermal conductivity so as to significantly reduce the transfer of heat between the body and the refrigerant in the inner chamber during a cryosurgical procedure. This can be realized by incorporating an external vacuum chamber as well. The fabrication of vacuum chamber has been widely used in the commercial cryoprobe. The primary probe and secondary probe are the active freezing portions of bifurcate cryoprobe. The fabrication of primary probe can follow the same fabrication process of the conventional probe as the primary probe has no moving part. The secondary probe requires welding the memory alloy with the primary probe.

When the temperature of the bifurcate cryoprobe drops to a controllable range, the secondary probe unfolds and detaches itself from the primary probe. The blade at the side assists the secondary probe to make minor tissue incision. When the secondary probe arrives at the targeted location, both freezing at primary and secondary probes commences and an irregularly shaped freezing

profile is induced. Once the process of the cryo-freezing has been completed, surgeons are required to warm up the bifurcate cryoprobe so that the secondary probe closes up and the bifurcate cryoprobe returns to the folded status. Active heating of the cryoprobe to control its mechanical motion has been successfully studied and interested readers are referred to the reference [44]. Besides shape memory alloy, there are several other driving mechanisms that can be employed to provide strong invasive cutting. Readers are referred to these work for comprehensive details [137, 138].

4.1.3. Radiofrequency ablation system

The electrosurgical radiofrequency generator (1500X, AngioDynamics Inc., Albany, Ny) is designed to provide the monopolar radiofrequency (RF) energy to be used for coagulation and ablation of soft tissue. The generator is indicated for use in the percutaneous, laparoscopic, or intraoperative coagulation and ablation of soft tissue, including the ablation of non-resectable liver lesions. The 1500X electrosurgical RF generator is capable of delivering up to 250 W of RF power. The output frequency is 460 kHz and the maximum output current is 6 Amp. It has multiple temperature displays as well as efficiency and power displays to assist the physician in monitoring the ablation throughout the process.

The large dispersive ground pads placed on patient's skin to provide a return path for the applied RF current. The ground pad consists of a flexible, thin-layered electrical conductor covered by an adhesive polymer gel layer, which enhances the area of the surface contact between the ground pad and skin. The ground pads applied in this work is RITA® ThermoPad. It consists of two dispersive electrodes that each has a temperature sensor at the distal end and a main cable for connecting the dispersive electrodes to the RF generator. ThemoPads are non-sterile, disposable, single use devices.

4.1.4. Temperature sensors

Type T (SCPSS-040U-6, OMEGA Engineering Inc., Stamford, Ct) thermo-couples were used to measure tissue temperatures. The diameter of thermocouples was 1.6 mm. The thermocouples are suited for the temperature range from 73 K to 623 K. Conductive adhesive transfer tapes (8805, 3M Inc., St.Paul, Mn) provide high thermal conductivity by focusing on the bulk conductivity and interface conductivity. The tapes were used to attach a thermocouple wire to the tip of cryoprobe. All thermocouples and the thermocouple wire were connected to a data logger (34970A, Agilent Inc., Santa Clara, Ca) to collect data at every 10 s. The temperature data was then transferred to an external computer for the post-processing. The thermocouples were allocated by the tailor-made thermocouple holder.

There are two marked downsides associated with this temperature monitoring technique. Firstly, the insertion of thermocouples into tissues is invasive. Secondly, the readings obtained through the local monitoring are only confined to the measured site. Hence, this technique has limitation in quantifying the extent of freezing.

The infrared thermography system has been employed to assist the monitoring the temperatures during cryosurgery. Infrared camera (VarioCAM, Jenoptik Inc., Jena, Germany) is a modern thermographic system for the precise, prompt and non-contact measurement of surface temperature of tissue. It equips with a digital color video camera for the photographic documentation of the prevailing measuring condition. It is a thermographic system for the long wave infrared spectral range of 7.5 μm to 14 μm. The lens images the object scene onto a microbolometer array at a maximum resolution of 640×480 pixels.

The working principle of the thermographic camera is based on the concept of emissivity. An object at a temperature higher than absolute zero emits electromagnetic radiation. The thermographic camera detects radiation in the infrared range of the electromagnetic spectrum. This infrared thermographic equipment has temperature resolution better than 0.08 K at 303 K. The auto-focusing lens embedded within the camera helps to deliver bright and rich contrast thermal images. The thermographic camera is capable for detecting temperature range of 233 K to 1473 K. During experiments, the thermographic camera was placed at an angle above the experimental samples. Images were acquired every 10 s and analyzed with the software of IRBIS$^{®}$ *Remote 3 Professional*.

4.1.5. Experimental samples

4.1.5.1. *Gelatin*

The study on gelatin study employs the gelatin with similar thermal properties to tissue [94] and allows observation of ice front by naked eyes. The gelatin phantom was produced by mixing the agarose power (SeaKem, Lonza Inc., Basel, Swiss) and distilled water. The solution was made of 2 % of gelatin and 98 % of water by weight to simulate the biological tissue. Heating up and disturbing the distilled water could accelerate the dissolving process. After thorough mixing, the gelatin phantom samples were naturally cooled down and allowed to solidify in a clear acrylic container.

4.1.5.2. *In-vitro tissue study*

Liver cancer in men is the second most frequent cause of cancer death while in women, it is the sixth leading cause of cancer death [1]. In view of this, experiments were also conducted with *in-vitro* livers. Experiments tested in

porcine livers have been proofed to be reliable and they have been used in many experimental studies [13, 44, 139].

4.1.5.3. *Blood vessels*

A 3.2 mm OD/1.6 mm ID Teflon tube was used to simulate the large blood vessel as the thermal conductivity (0.21 $W\ m^{-1}K^{-1}$) is close to that of blood vessel (0.2-0.5 $W\ m^{-1}K^{-1}$) [140]. To simulate the blood vessel, the Teflon tube was passed through holes drilled on opposite boards as shown in Figure 4.4 (a). Similarly, the Telflon tube embedded in a porcine liver is shown in Figure 4.4 (b).

(a)   (b)
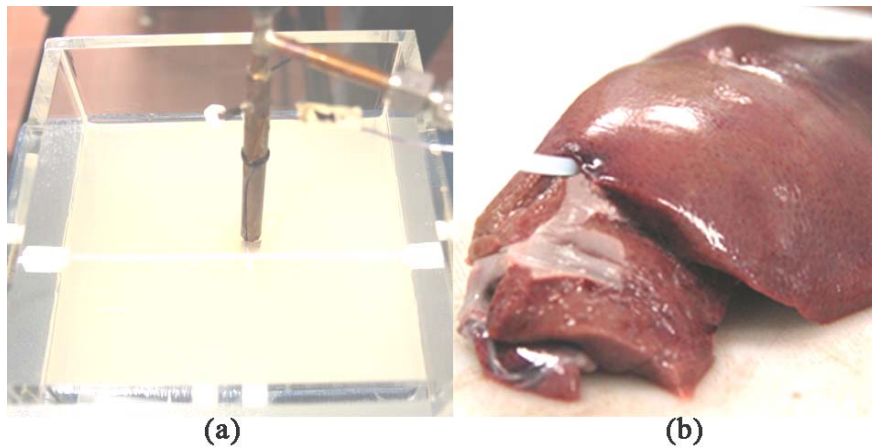
Figure 4.4 Snapshots of samples embedded with a vessel. (a) a blood vessel in the gelatin phantom study; (b) a blood vessel in the porcine liver sample.
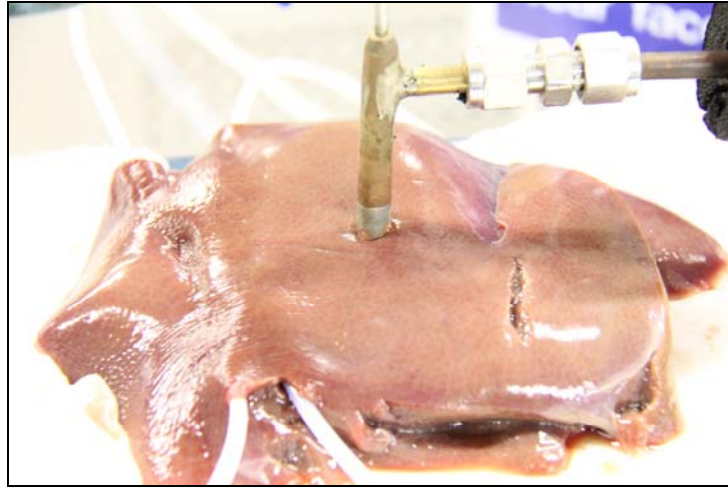
Figure 4.5 porcine liver with countercurrent vessels.

To facilitate the model validation, we also conduct experiments in *in-vitro* samples with countercurrent flow as shown in Figure 4.5. The same type Teflon tube was inserted in liver as shown. Circulating water controlled by temperature controlled bath was used to simulate the blood flow.

4.2.   Experimental procedure

4.2.1. Conventional cryosurgical system

This section illustrates the conventional cryosurgical system.   The rationale is to use liquid nitrogen to freeze experimental samples via the phase change of the freezing medium. It is a simple and common design.
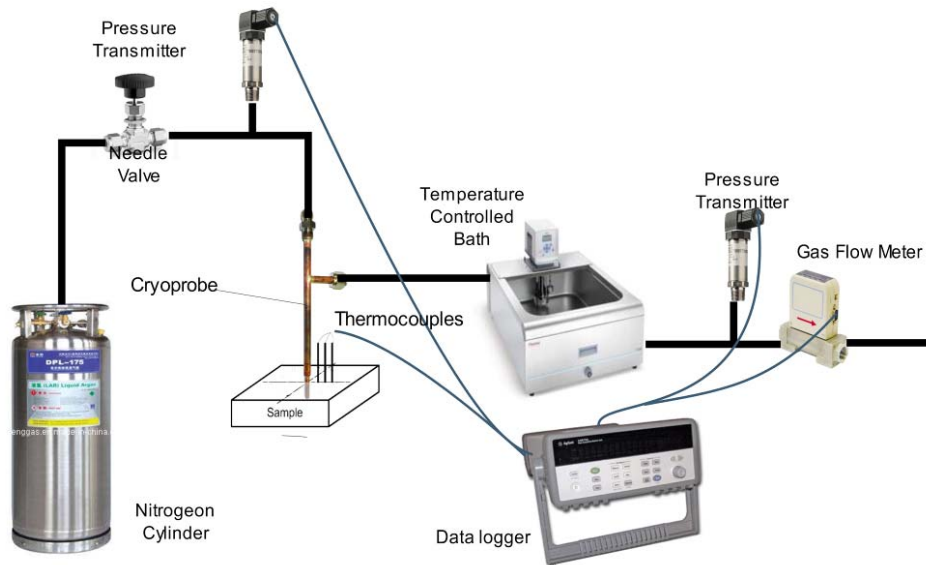
Figure 4.6 Schematic diagram of a conventional cryosurgical system.

A schematic diagram of the conventional cryosurgical setup is shown in Figure 4.6. Liquid nitrogen flow was controlled by a high-sensitive needle valve (S8-1HM4, Swagelok Inc., Solon, Oh) and the pressure was monitored by a pressure transmitter (0-16 bar, control type 500, Huba Control Inc., Switzerland) located at the downstream of needle valve. The liquid freezing medium was passed into a freezing cryoprobe through a homocentric inner steel tube within the cryoprobe. When the liquid nitrogen was released at the tip of the cryoprobe, cryo-freezing was initiated due to the fluid evaporation when its pressure dropped. The flow was piped into a water temperature controlled bath (SAHARA S49, Thermo Fisher Inc., Waltham, Ma) . The water temperature controlled bath raises the temperature of nitrogen flow and avoids unintended cryoinjury at outlet. The pressure and the flow rate of the exhausted outlet gas were measured by a pressure transmitter (0-8 bar, control Type 500, Huba Control Inc., Switzerland) and a gas flow meter (MTF4130-D-01, Malema Sensor Inc., Boca Raton, Fl), respectively. T-type thermocouple probes (SCPSS-040U-6, OMEGA Engineering Inc., Stamford,

49

Ct) were used to measure sample temperatures while a thermocouple wire was used to measure the tip temperature of the cryoprobe.

4.2.2. *In-vitro* samples embedded with large blood vessels

The experiment in this section was designed to study the thermal importance of large vessels. The structure of large blood vessels can produce steep temperature gradients subjected to the location and induce inadequate cooling during cryosurgery [20, 42]. The influence could be even significant for the cryotherapy in hepatic tumor treatments, where the total hepatic blood flow amounts to approximately a quarter of total cardiac output at rest [141], even though it constitutes only 2.5% of body weight [142]. Therefore, we studied the vascular effect of large vessels.

Blood contains a large amount of water. Study shows that about 55% of blood is blood plasma, which is essentially an aqueous solution containing 92% water [143]. Blood has an average density of approximately 1060 kg/m^3, very close to water's density of 1000 kg/m^3[144]. Due to the similar thermal properties between blood and water, there are several existing articles using water to simulate the blood flow during cryosurgery [20, 145]. The experimental sample can be found in Figure 4.4. In this section, distilled water was used to simulate the blood flow. The water temperature was controlled by a water temperature bath maintained at 310 K. The circuit pressure driving the water flow was achieved by a peristaltic pump. The mass flow of water was controlled at 60 g/min. The water flow was circulated to the Teflon tube for 10 min ahead of the commencement of freezing. The inlet temperature of water was set as 310 K.

4.2.3. Stabilize the conventional cryosurgical system

This section contributes to produce a stabilized system to facilitate controlling

and monitoring during cryosurgery. It was established based on Section 4.2.1 by including new components. Compared to the conventional system, the proposed system includes new devices stabilizing the piping system. The liquid use valve was connected to a pressure regulator (RG125, REGO Inc. Houston, Tx) followed by a safety relief valve (9400, REGO Inc. Houston, Tx). The pressure regular is a valve that automatically cuts off the flow at certain pressure and reduces the usable pressures. It was applied to stabilize the pressure at the upper stream of cryoprobe.

Although many efforts have devoted to cryosurgery planning [4, 9, 34, 35], specific studies dedicated to investigating parameters that enhance the control of the cryosurgical system are very few. Basic thermal properties such as the flow rate, temperature, and pressures at essential locations in the common cryosurgical system can potentially affect the outcome of the surgery. The correlation between the performance of the cryo-device and the liquid level of the freezing medium ought to be investigated.
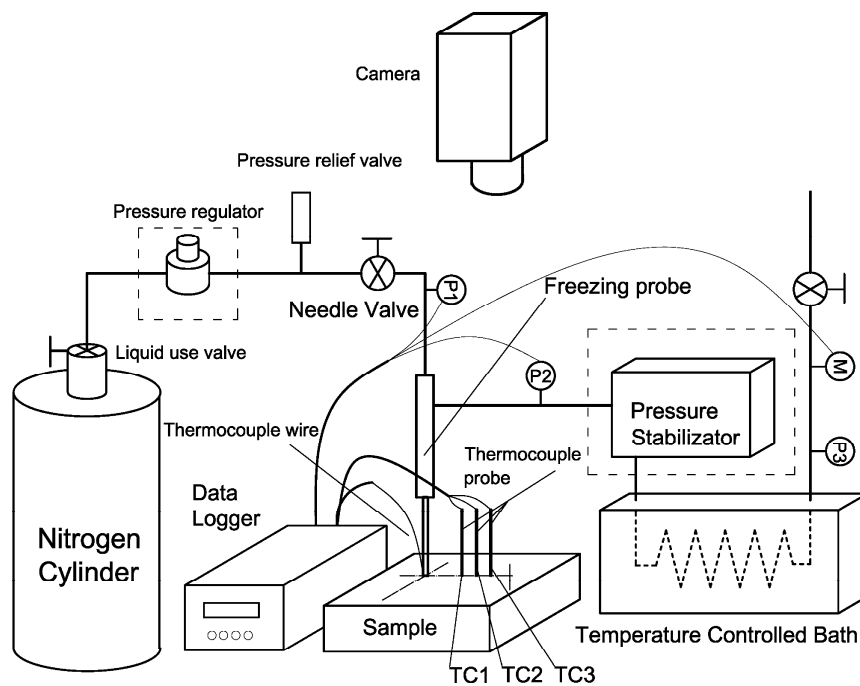
Figure 4.7 Schematic diagram of the modified experiment setup.

51

To enhance the control of freezing process, new components were employed to the conventional system as shown in Figure 4.7. The new devices stabilizing the piping system were highlighted with dot lines. The liquid use valve was connected to a pressure regulator (RG125, REGO Inc. Houston, Tx) followed by a safety relief valve (9400, REGO Inc. Houston, Tx). The pressure regular is a valve that automatically cuts off the flow at certain pressure and reduces the usable pressures. It was applied to stabilize the pressure at the upper stream of cryoprobe. When the flow rate of liquid nitrogen was significant, large amounts of liquid nitrogen experienced an incomplete phase change within the cryoprobe. The phase change in the water temperature bath could be intensive to affect the downstream pressure of the cryoprobe. Therefore, a lab-made pressure stabilizer was connected at the downstream of the cryoprobe to reduce the pressure fluctuation. The pressure stabilizer was a large container to reduce the pressure variance.

4.2.4. Cryosurgery incorporating peripheral Joule heating elements

This section contains two parts. The first part tests the freezing probe together with heating probe. These experiments tests provide basic data for model validation of freezing and heating process. The validated model was used to test the performance of hybrid cryoprobe and freeze-thaw cycles. The second part tests a new device named heating coil. The experiment was designed to visualize temperature contours and provided experimental data for model validation.

4.2.4.1.   *Reducing the unwanted frozen zone for internal tumors*

The schematic diagram of the cryosurgical system involving an 8 mm diameter cryoheater is shown in Figure 4.8. The cryoheater is a concept based on heating the tissue as a means of shaping the frozen region [117]. It is a

complementary device to the cryosurgery. In experiments, the cartridge heater was placed 24 mm from the cryoprobe. Six thermocouples (Omega, Type T) were used to measure the tissue temperature with the essential labels marked. TC1 to TC2 and TC2 to TC3 were linearly aligned at equidistance of 6 mm. The distance between TC1 and the cryoprobe center was 7 mm while the distance between TC4 and cryoheater center was 5 mm.
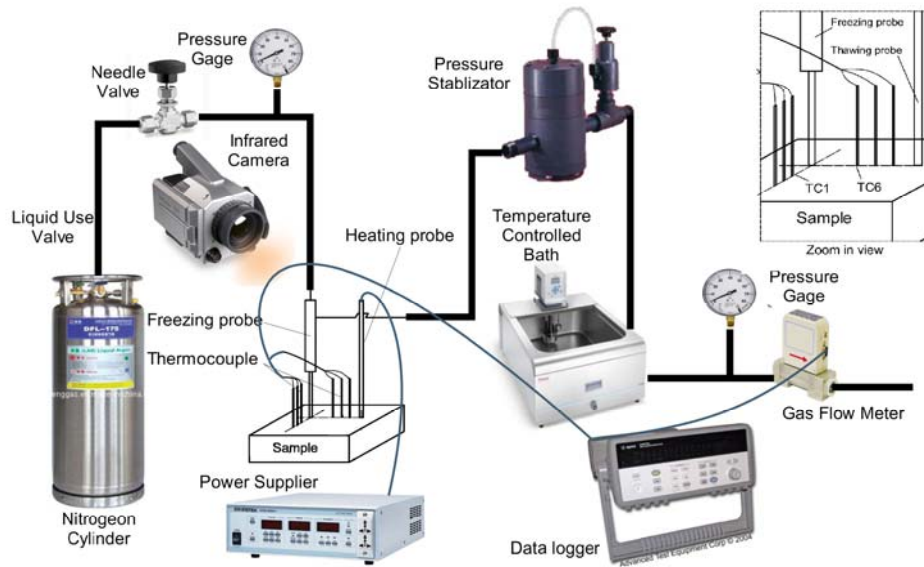
Figure 4.8 Experiment setup of the complete setup with heating and freezing probe. The thermocouple allocation is shown in the zoom in view.

An adjustable power supplier (APS-9102, GW Instek Inc., Taipei, Taiwan) was used to power the cryoheater. The GW Instek is a dual output, linear AC power source with the output capacity of 1 kVA. The maximum output current at 220 V is 4.2 A. In experiments, the GW Instek was set to produce either 9 W or 12 W for the cryoheater and sustain a desired heating temperature for 10 min [146].
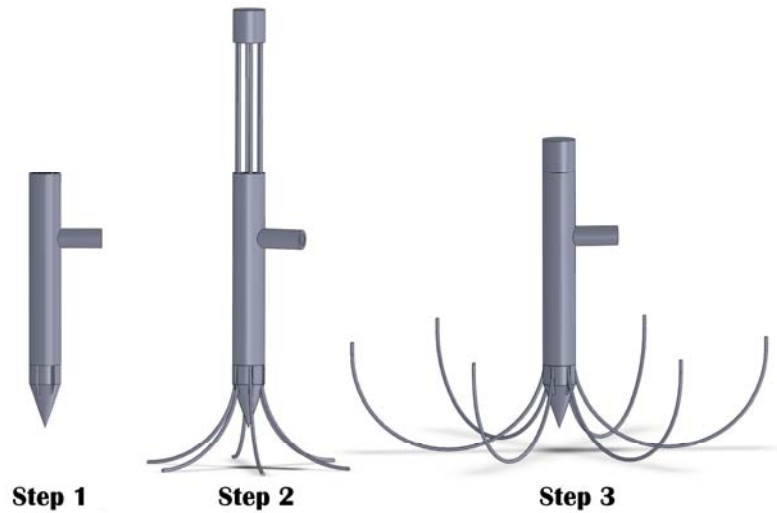
Figure 4.9 Procedure of employing the hybrid cryoprobe into the targeted location.

Combining the Joule heating and cryo-freezing, a hybrid cryoprobe was developed. The hybrid cryoprobe comprised a single cryoprobe with several thin hook-shaped cryoheaters as secondary probes. The procedure of employing the hybrid cryoprobe is shown in Figure 4.9. Such a probe design allows the flexibility of freezing and heating controls. During a clinical operation, the cryoheaters are stored within the channels of the primary freezing probe as Step 1. When the hybrid cryoprobe is delivered to the targeted location, the cryoheaters can be deployed at the tip of the main probe in Step 2 and Step 3. The retractable hook-shaped cryoheaters can be designed to carry out heating effectively at the distance near their tips. In short, the freezing probe generates the central cryolesion while cryoheaters regulate the size of unwanted frozen zone.

4.2.4.2. *Reducing the unwanted frozen zone for surface tumors*

A schematic diagram of the experiment setup to reduce the unwanted frozen tissue in the cryoablation of surface tumors is similar to Section 4.2.4.1. During experiments, an infrared camera was faced to samples at a distance of around 25 cm. The thermocouple allocation is shown in Figure 4.10. Heating coils were made of Kanthal Nikrothal 80 wire with an electric resistance of

54

11.13 Ω/m. The heating coil, designed to connect to the power supplier, was strategically placed at a predetermined position; enclosing the designated solid tumor. Two types of heating coil with 35 mm and 50 mm diameter were used during experiments. The heating coil of 50 mm diameter during experiment is shown in Figure 4.11.
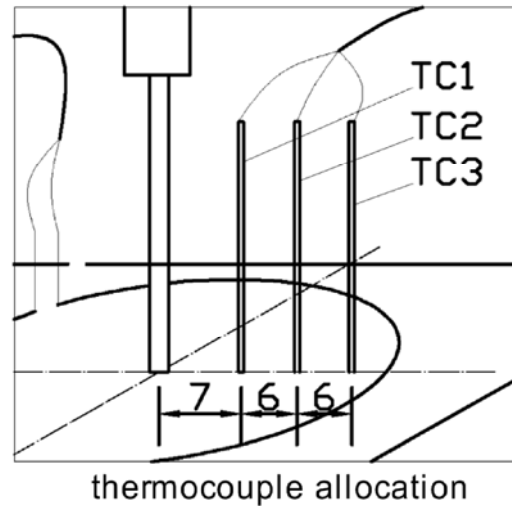
Figure 4.10 Schematic diagram of reducing the unwanted frozen zone for surface tumors.
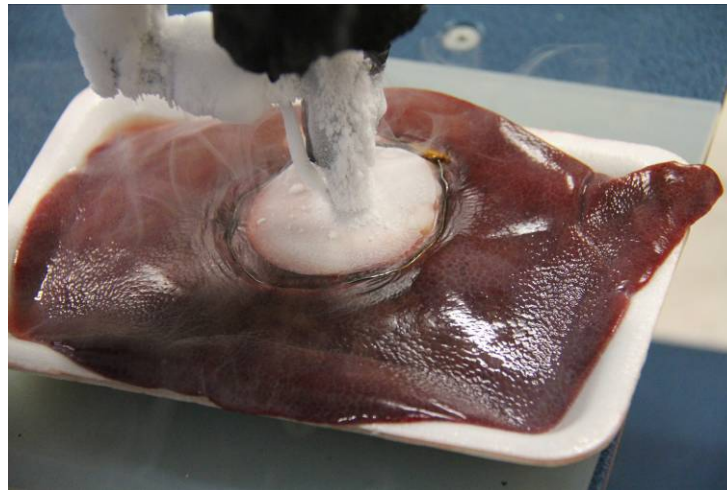
Figure 4.11 heating coil during experiment when the thermocouples are removed.

4.2.5. RF-assisted cryosurgical ablation

This section focuses on the experimental study on radiofrequency ablation and combination of RF ablative process and cryosurgical process. The purpose of studying RF ablative process is to evaluate the heating features. We

investigated the single RF probe and multi-tine RF probe. The purpose of combining RF ablation with cryoablation was to assess the cryosurgical process with RF-generated heating.
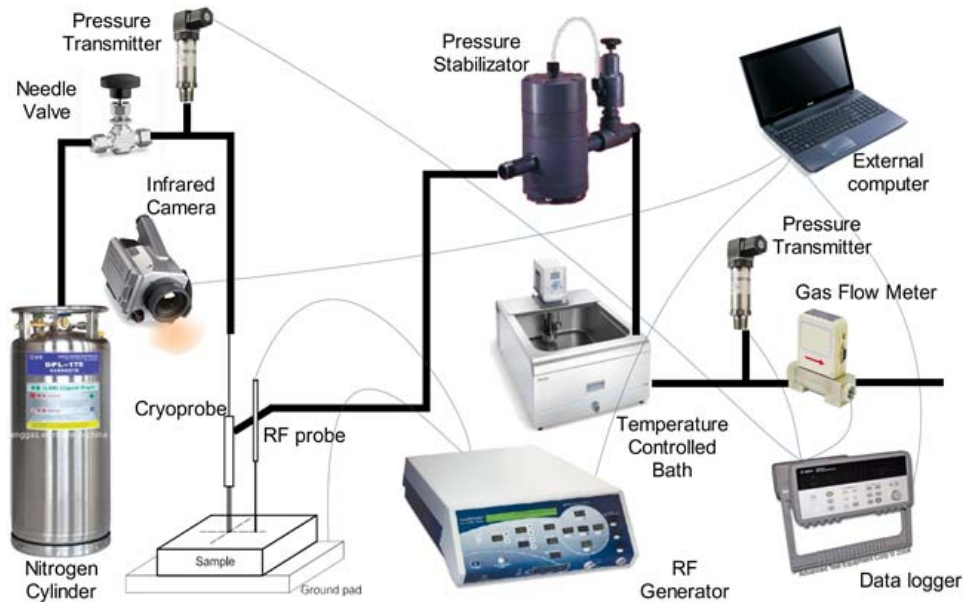
Figure 4.12 Experimental setup of the RF-assisted cryosurgery.

A schematic diagram of RF-assisted cryosurgery is shown in Figure 4.12. The cryosurgical setup was identical with the conventional cryosurgical system. The electrode was powered by a RF generator (RITA 1500X, AngioDynamics Inc, Latham, NY). The RF generator had a maximum output power of 250±2 W. The output frequency was 460 kHz±5%. The automatic temperature control (ATC) mode is a preinstalled mode of the RF generator. It uses selected temperature readings from temperature sensors as the feedback to control the delivery of power. In other words, the power delivery is automatically controlled based on the temperature readings of the thermal sensors. The ATC mode is always followed by a cool down mode. Once the ablation cycle is complete, the system enters the cool down mode for 30 s. The cool down is a measure of the robustness of the ablation. When the average temperature of the ablation after 30 s is below 328 K, the ablation is likely to be under

developed. An additional ablation is recommended to ensure a complete ablation.
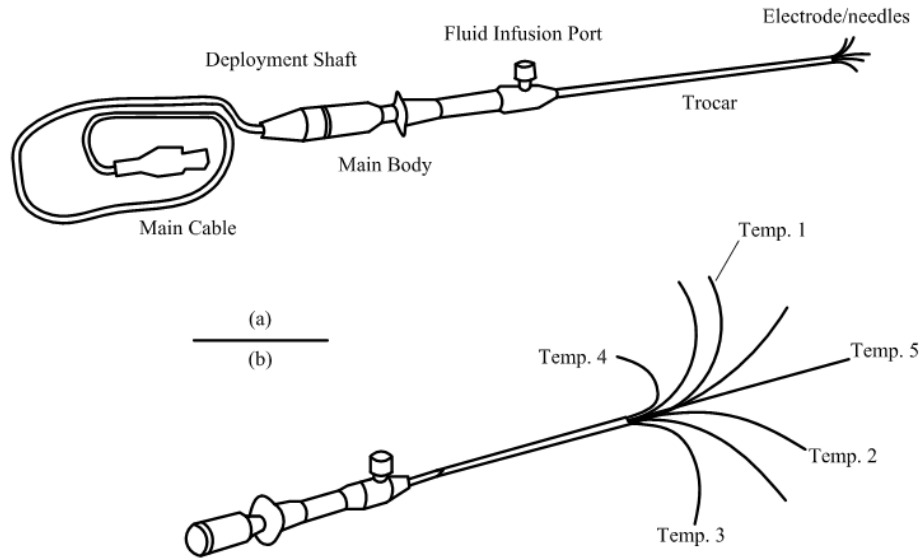
Figure 4.13 (a) Components of a multi-tine RF probe; (b) the deployed electrodes with the temperature sensors (Temp.1 to Temp.5) marked.

The schematic diagram of nine-tine RF probe is shown in Figure 4.13(a). It contains a main cable, deployment shaft, a fluid infusion port and a movable hub of 9 curved electrodes that can be retracted or deployed from the tip of the needle. Five temperature sensors are incorporated into tips of electrodes to register the temperature of the heated tissue. The respective number of the temperature monitors is shown in Figure 4.13(b).

The temperature data set of electrodes was recorded by 1500x data collection software installed in an external computer. Temperature contours during experiments were monitored by a high resolution thermographic camera (VarioCAM, InfraTec Inc., Plano, Tx). The camera has a thermal resolution of better than 0.03 K at 303 K and can capture temperatures spanning 233 K to 1473 K.
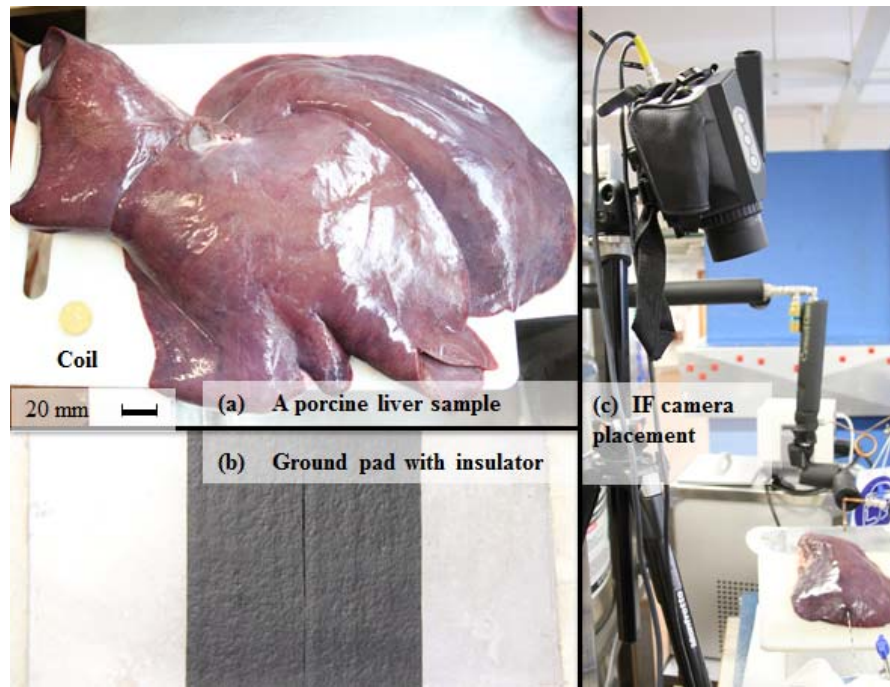
Figure 4.14 Facilities used during experiments. (a) a porcine liver sample; (b) a ground pad with rubber insulator; (c) placement of infrared camera.

Figure 4.14 shows the facilities used during experiments, including a porcine liver sample, a ground pad and an infrared camera. The porcine liver in Figure 4.14 (a) is more than 350 mm long. Large livers promote the monitoring and allow the formation of large ablation zone. Figure 4.14 (b) shows the ground pad with the rubber insulator. The rubber insulator can be attached to the surface of the ground pad so that the covered portion of the ground pad is ineffective in conducting currents. Figure 4.14 (c) shows the placement of infrared camera during experiments.

4.3.   Measurement uncertainties

VarioCAM® HR has a measurement accuracy of ±1.5 K in the range from 273 K to 373 K and the accuracy reduces to ±2% beyond this range. The temperature resolution of the thermographic image at 313 K is better than 0.08 K. The premium mode of temperature resolution is up to 0.05 K. The

thermocouples are calibrated with precision bath thermometer in the positive and negative scales. The uncertainty due to the calibration for the temperature readings is ± 2.5%. The maximum output power of the RF generator is 250 W and the power accuracy is ±2%. The temperature measurement accuracy in the RF ablation system is ±3% from 288 K to 398 K while the accuracy increases to ±5% below 288 K and above 398 K. The output frequency of the RF ablation system is 460 kHz, with the uncertainty of ±5%.

Chapter 5: Improving the Efficacy of Freezing Process

This chapter contains three sections to enhance the freezing process during cryosurgery. The first one is an experimental study of crucial parameters on the control of freezing delivery. The cryosurgical system is tested under different operating protocols and the influence of controlling parameters is analyzed. Several improvements have been incorporated into the conventional system. The other two sections involve numerical simulations on how to generate customized ablation zones for irregular tumors and how to embed a clinically-extracted vascular network in the cryosurgery planning. Results obtained in this chapter have promote the efficacy of the freezing process during cryosurgery.

5.1.   Effects of crucial parameters on the control of freezing process

It is generally believed that rapid freezing, slow thawing and repetition of freeze-thaw cycles improve surgical outcomes. A well-controlled freeze-thaw cycle requires the adequate regulation of key parameters in the cryosurgical system. This section investigates key parameters that significantly influence on the performance of cryoprobe. In a conventional system, the inlet pressure of cryoprobe and the flow rate are found be highly unstable under certain circumstances. These could induce intense difficulties in monitoring the real-time treatment response and analyzing their impacts on the system performance. We have proposed a modified system that stabilizes pressure and flow rate. With this system, the thermal impacts of the controlling parameters can be regulated with accuracy.

5.1.1. Stabilizing the flow rate of freezing medium

In section 4.2.3, the conventional system has been modified to enhance the stabilities of the pressure and flow rate. The experiments are tested at a targeted flow rate of 300 L/min. The results of the two systems are compared in Figure 5.1. The flow rate of the freezing medium is a key factor that provides the desired freezing power of the cryoprobe; however, a dominant problem embedded in the conventional system is the large variance of the flow rate as shown in Figure 5.1(a). The intense fluctuation induces tremendous difficulties in monitoring and adjusting the real-time flow rate in cryosurgical procedures. To reduce the instability, a pressure regulator and a pressure stabilizer are employed. Figure 5.1(b) shows the experimental results of the system performance with the same targeted flow rate. The fluctuation of flow rate after 200 s becomes stable. The minimum temperatures that the two systems achieve are similar around 113 K. It is also evidenced that the adoption of the stabilizing devices markedly enhance the stability of both coolant flow rate.
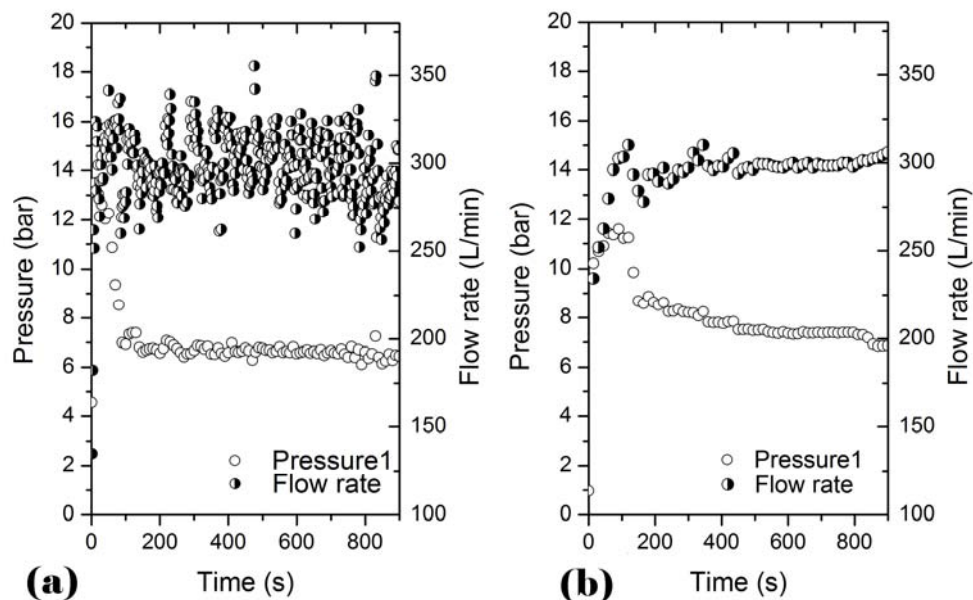
Figure 5.1 variation of pressure and flow rate in the two systems. (a) the conventional cryosurgical system without stabilizing devices; and (b) the enhanced cryosurgical system with stabilizing devices.

5.1.2. Ice front and thermal injury

Pathological changes in the cryozone can be divided into five parts as a central necrosis zone, an inflammation zone, a hyperemia zone, a granulation zone and an apoptosis zone [147]. The first four zones are generally classified as the complete ablation zone. The key portion of complete ablation zone is the central necrosis zone. A previous study has revealed that the remaining three zones are very narrow for only one or several millimeters in radius [147]. Examining the pathologic changes can produce more accurate and reliable results; however, it is almost impossible to take a series of samples to confirm during cryosurgery.
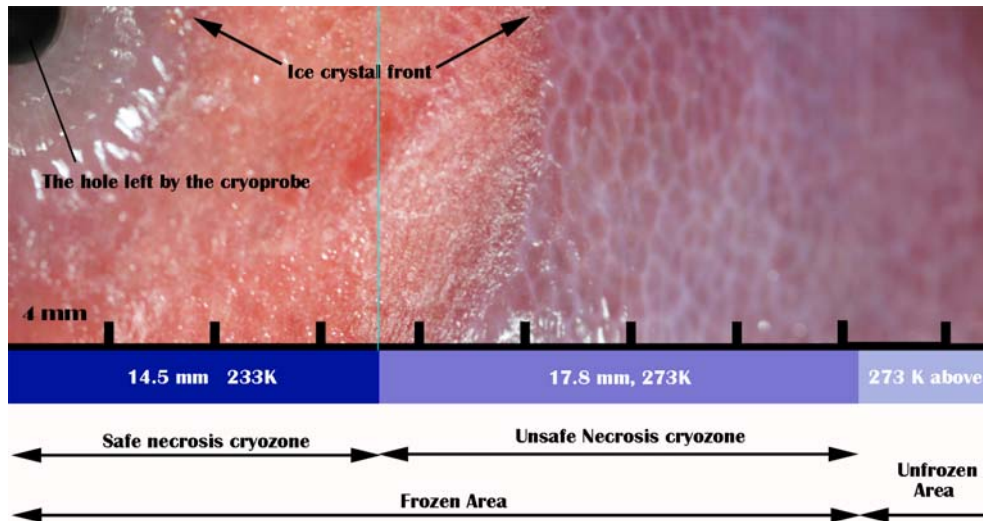
Figure 5.2 Demarcation of tissue cryo-zones in *in-vitro* porcine liver tissue.

Figure 5.2 shows the tissue damage in the cryozone at a freezing duration of 1600 s when the flow rate is 250 L/min. 233 K is chosen as the critical temperature, demarcating the central zone of complete ablation (safe necrosis cryozone). The rest frozen zone is assumed as the unsafe or unwanted ablation zone since the ablation is incomplete. According to the thermal camera's readings, key isothermal lines are identified in the radial direction. The radius of 233 K isotherm was observed to be 14.5 mm while the radius of the ice front was 32.3 mm.

5.1.3. Protocol of constant flow rate

The stabilized system shown in Figure 4.7 has reduced the fluctuation of the cryosurgical system. The flow rate was used as the dominating monitor to regulate the freezing power during cryosurgery. Figure 5.3 shows the inlet pressure (P1) responses to four predetermined flow rates within a constant freezing duration of 1600 s. The maximum pressures obtained under flow rates of 100 L/min, 150 L/min, 250 L/min and 300 L/min are observed to be 4.6 bar, 6.8 bar, 10.9 bar and 11.8 bar, respectively. Large flow rates typically are associated with high entrance pressures. To reach the predetermined flow rate, a "pressure jump" is observed to be effective at the beginning of freezing. The pressure subsequently drops to prevent the flow rate from building up beyond the targeted range. Pressure drops during constant flow rate can be divided into three stages. The first stage includes a sharp pressure drop which occurs just few minutes after reaching the maximum pressure. The second stage has a gentler pressure depreciation followed by the final stage which is an even subtler pressure reduction. These three stages can be observed in Figure 5.3 as depicted by the three different gradients (slope 1 to 3).
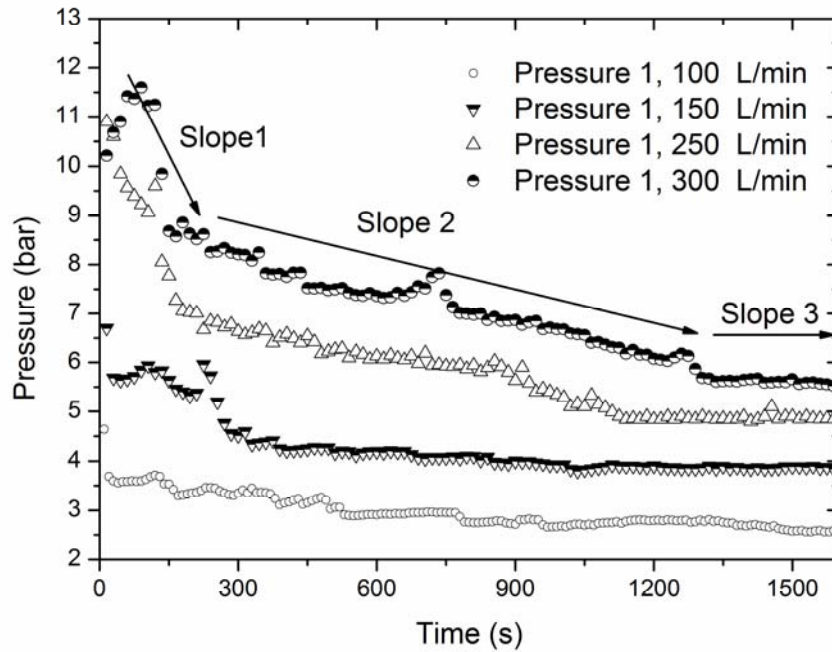
Figure 5.3 Entrance pressure in respond to flow rate of freezing medium.

Sustaining a cooling flow rate is of paramount importance when the surgeon desires a uniform freezing rate. A stabilized flow rate delivers a relatively steady freezing ability. The pressure jump at the initial stage can be attributed to the mechanism of continuous phase changes. When the liquid freezing medium flows into the piping system, there is a possibility of intense phase change due to the large temperature difference with surroundings. The intense phase change induces a large back pressure at the downstream of the cryoprobe. In other words, the "resistance" of fluid entering the piping system is extremely high at the beginning. To achieve the predetermined flow rate rapidly, a higher pressure is required to compensate the "resistance" at the start of experiments.
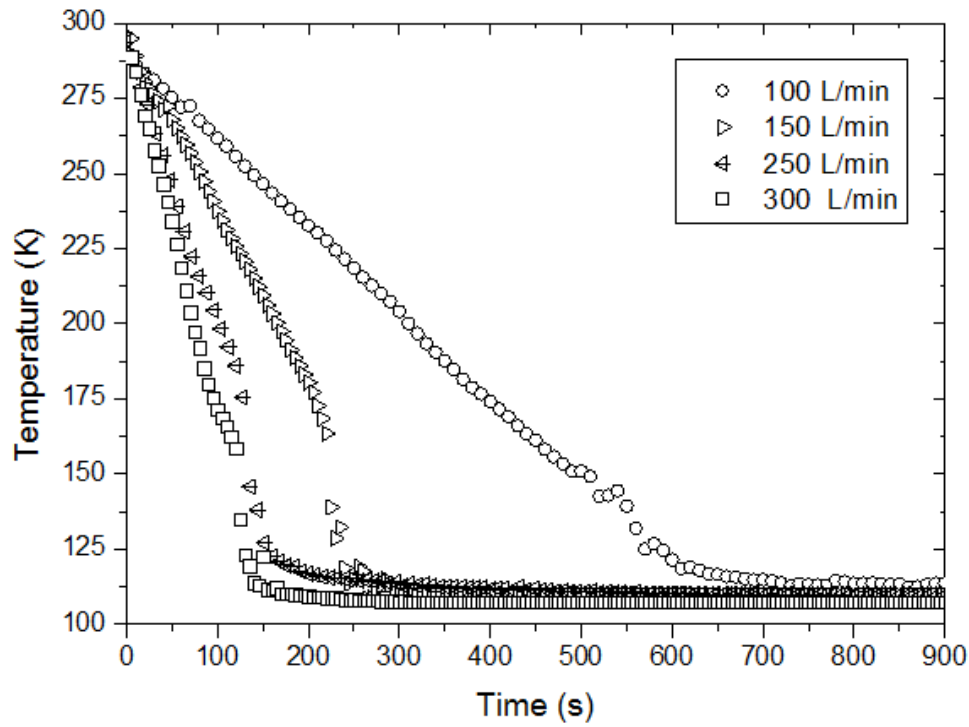
Figure 5.4 Cryoprobe temperature in response to the flow rate.

Figure 5.4 compares the cryoprobe temperatures at the initial stage. Minimum temperatures of the cryoprobe, controlled at four flow rates, are around 108 K. A reduced flow rate has observed to extend the duration of reaching the lowest temperature. The duration of reaching the lowest temperature is defined as the initial freezing $IF(\delta,t^*)$. t^* suffices for the duration to achieve a relative stable temperature. δ refers to the percentage of temperature drop of the cryoprobe within t^*. A high value of δ is commonly associated with a large $IF(\delta,t^*)$. Based on the results shown in Figure 5.4, the $IF(\delta,t^*)$ at the four flow rates when $\delta=90$ and $\delta=95$ are shown in Table 5.1.

Table 5.1 Duration of initial freezing at a constant flow rate

Duration of *IF* (*s*)	$\delta=90$	$\delta=95$
100 *L/min*	575	560
150 *L/min*	240	230
250 *L/min*	173	151
300 *L/min*	150	125

It is noteworthy that the above results were obtained when the freezing medium during cryosurgery was sufficient. Instances when the source of the freezing medium is inadequate are discussed in section 5.1.5. It is apparent from the presented results that with an adequate freezing medium, an increase in the flow rate results in a depreciated $IF(\delta,t^*)$ at a decreasing rate.

5.1.4. Passive control mechanism

A passive control mechanism maintains the settings of pressure regulator and needle valve without any manual regulations during cryosurgery. As the pressure regulator is predetermined, the pressure change is considered to be small. This operating mode enables to study the development of flow rate and the cryoprobe temperature. Four experiments at targeted pressures are conducted and their flow rates are shown in Figure 5.5. Results show that large entrance pressures are associated with large flow rates. Under the passive controlling mode, the development of flow rate can be categorized into two levels. When experiments initiate, the flow rate raises rapidly from zero to the first level within few seconds. A high entranced pressure produces a large flow rate at the first level. Thereafter, the flow rate shots up gradually to a higher level.
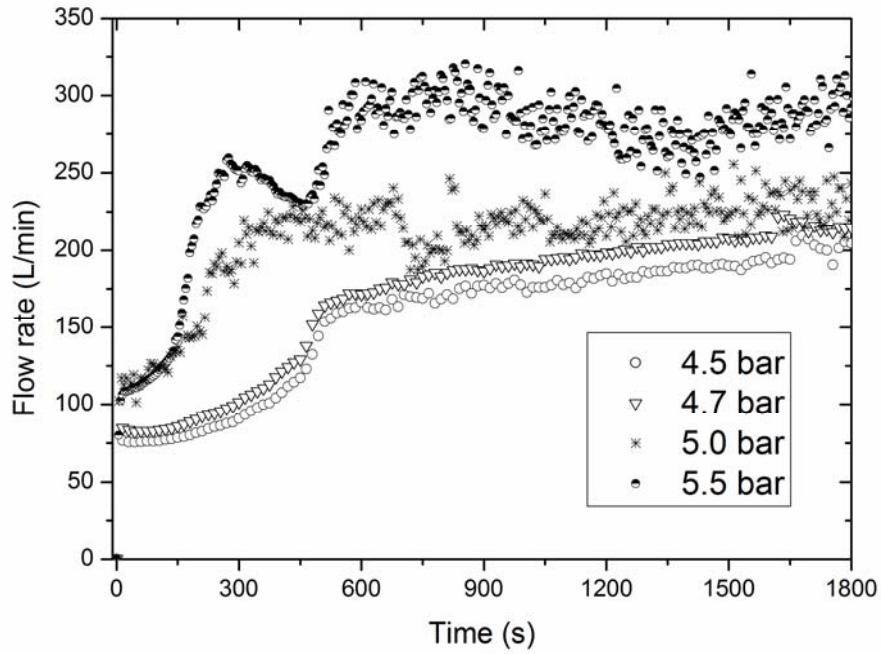
Figure 5.5 Comparison of flow rates at different inlet pressures.

The tip temperature of cryoprobe under the passive control mode is shown in Figure 5.6. Albeit an improved inlet pressure from 4.5 bar to 5.5 bar, the flow produces only a marginal difference on the minimum temperature but $IF(95, 800)$ shortens from 492 s to 163 s. In contrast to the constant flow rate mode, the temperature drop is observed to accelerate as the temperature is close to the minimum temperature.
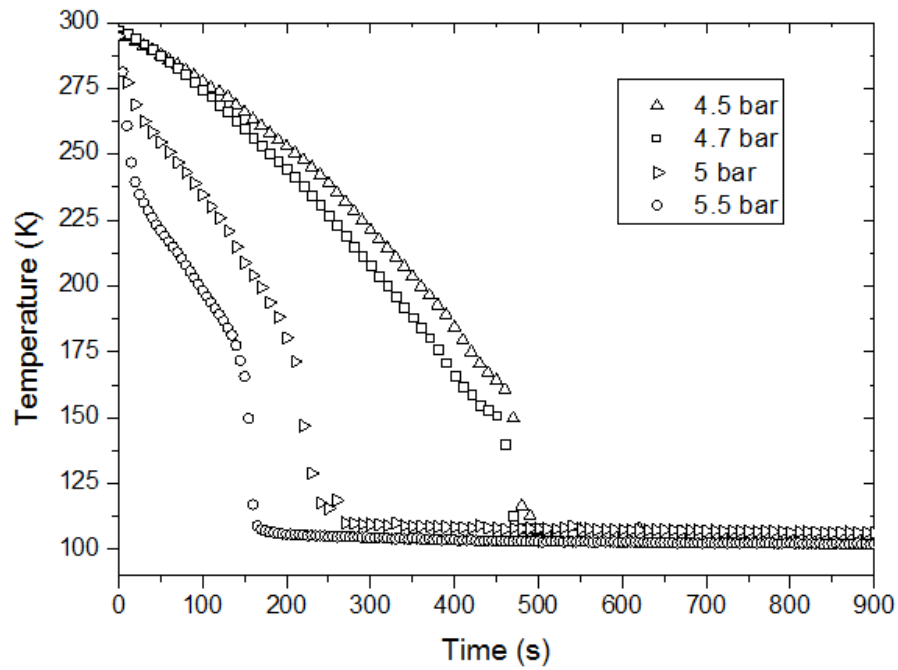
Figure 5.6 Variations of cryoprobe temperatures at different inlet pressures.

5.1.5. Influence of the liquid level of nitrogen
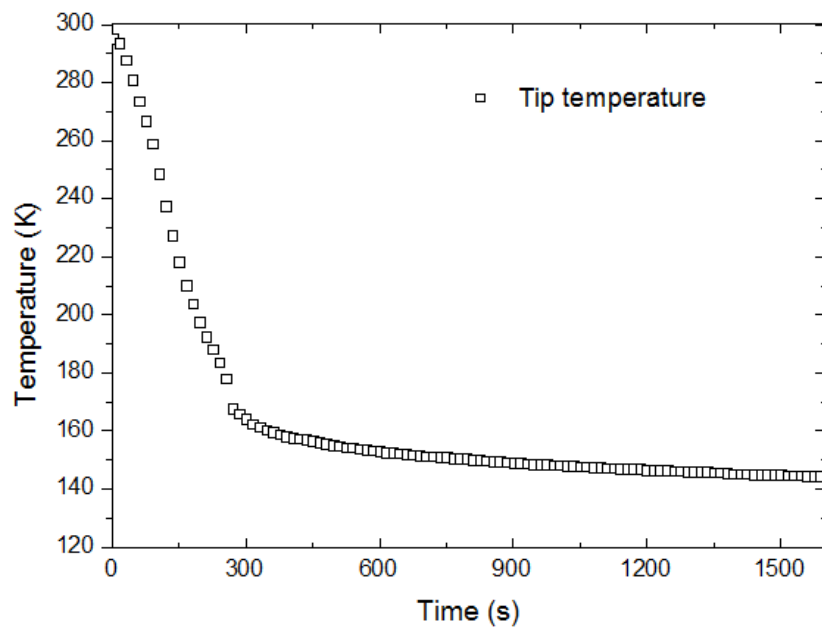
Figure 5.7 Development of the tip temperature when level of the liquid nitrogen is
0.28 of the full capacity.

The liquid level of nitrogen stored in the container falls as the cryosurgical

68

process proceeds. A low nitrogen level can potentially undermine the efficacy of surgery due to the insufficient freezing power. The primary objective of this section is to investigate how the amount of the freezing medium impacts the performance of the cryoprobe. Figure 5.7 demonstrates the thermal characteristics of the system when the liquid level drops to 0.28 of its full capacity. The experiment was controlled by adjusting the pressure regulator to sustain the flow rate at 250 L/min. The nitrogen level was continuously monitored using a liquid level indicator. The cryoprobe temperature inserted in porcine liver samples droped sharply within the first 300 s and the minimum temperature was 142 K at 1600 s. Comparing with results in section 5.1.4, the minimum temperature in this case is substantially higher. The result reveals that the liquid level in the cylinder is indeed an important factor that impacts the freezing ability of cryoprobe.
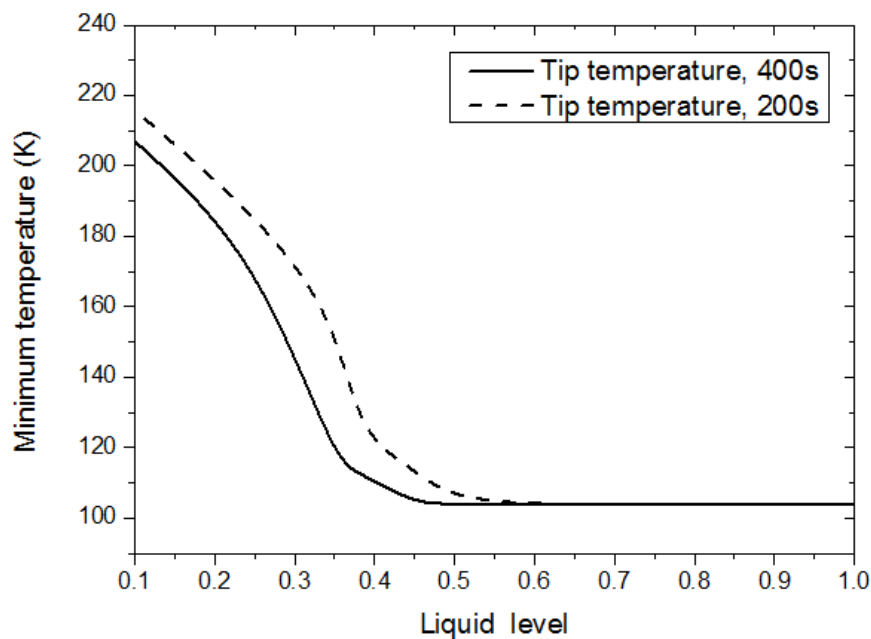
Figure 5.8 Minimum temperatures of cryoprobe in response to liquid levels within 200 s and 400 s.

Figure 5.8 illustrates the influence of the liquid level of freezing medium on the minimum temperature of cryoprobe. Results have indicated that the capacity of the freezing medium markedly affects the reliability of the

cryosurgical process. When the liquid level dropped to a range below 0.6, we observed a major difference in the minimum temperature. Regular periodic checks were necessary to ensure sufficient freezing power. When the liquid level dropped to below 0.4, the minimum temperature of cryoprobe was significantly compromised.

5.1.6. Orthogonal experiment analysis

The first step involved in the orthogonal experiment analysis is to choose a suitable orthogonal array. According to $L_9(3^3)$ design, 9 experiments are carried out. The minimum temperatures and initial freezing of the different combinations are calculated as shown in Table 5.2 with $\delta=90$ and $t^*=1400$ s. The range of pressure spans 4.5 bar to 5.5 bar, the range of flow rate is from 100 ml/s to 250 ml/s and the liquid level varies from 0.3 to 0.9. Table 5.2 indicates that the range of the lowest temperature varied from 148 K to 104 K while the period for the initial freezing reduced from 750 s to 146 s.

Table 5.2 Results of orthogonal experiment $L_9(3^3)$ design. Selected combinations are scattered uniformly over the space of all possible combinations.

Experiment Number	Factor A	Factor B	Factor C	Lowest temperature $Y^{(1)}$	Initial freezing $Y^{(2)}$
	Pressure	Flow rate	Liquid level		
	(*bar*)	(*L/min*)	-	(*K*)	(*s*)
1	4.5	100	0.3	148	750
2	4.5	150	0.6	111	238
3	4.5	250	0.9	109	146
4	5.0	100	0.6	110	580
5	5.0	150	0.9	109	223
6	5.0	250	0.3	142	290
7	5.5	100	0.9	118	560

	8	5.5	150	0.3	145	402
	9	5.5	250	0.6	104	152
Minimum temperature(K)	$F_{1,j}^{(1)}$	368	376	435	-	-
	$F_{2,j}^{(1)}$	361	365	325	-	-
	$F_{3,j}^{(1)}$	367	355	336	-	-
	$\bar{f}_{1,j}^{(1)}$	668.7	671.3	691	-	-
	$\bar{f}_{2,j}^{(1)}$	666.3	667.7	654.3	-	-
	$\bar{f}_{3,j}^{(1)}$	668.3	664.3	658	-	-
	$R^{(1)}$	2.3	7.0	36.7	-	-
Initial freezing(s)	$F_{1,j}^{(2)}$	1134	1890	1442	-	-
	$F_{2,j}^{(2)}$	1093	863	970	-	-
	$F_{3,j}^{(2)}$	1114	588	929	-	-
	$\bar{f}_{1,j}^{(2)}$	378	630	480.7	-	-
	$\bar{f}_{2,j}^{(2)}$	364.3	287.7	323.3	-	-
	$\bar{f}_{3,j}^{(2)}$	371.3	196	309.7	-	-
	$R^{(2)}$	13.7	434	171	-	-
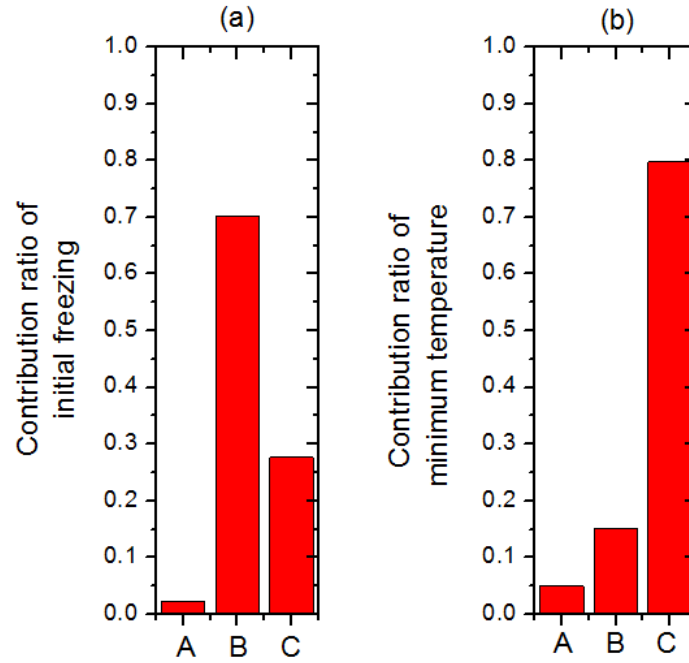
Figure 5.9 Contribution ratios (a) initial freezing of cryoprobe; and (b) minimum temperature of cryoprobe due to different factor values.

Figure 5.9 shows the contribution ratios of the initial freezing of cryoprobe and the minimum temperature. According to Figure 5.9 (a), the initial freezing largely depends on the flow rate while Figure 5.9 (b) shows that the minimum achievable temperature can be significantly affected by the liquid level of nitrogen. Considering the target function of producing the lowest temperature, the optimal combination consists of the following parameters: 5 bar, 250 L/min and liquid level at 0.6. In contrast, to achieve the shortest initial freezing duration, the best combination is made up of the following parameters: 5 bar, 250 L/min and liquid level at 0.9.

5.2. Cryosurgery planning based on the shape factor of complete ablation zone

The objective in this section is to investigate the irregularity index of a desired ablation zone. This index serves to measure freezing efficacy and quantify cryoinjury to the surrounding healthy tissue. Additionally, we propose a

unique cryoprobe that is specifically catered to the treatment of irregularly shaped solid tumors. Results obtained in this work enable cryosurgeons to analyze the efficacy specifically tailored for irregularly shaped tumors.

5.2.1. Thermographic images with a conventional cryoprobe
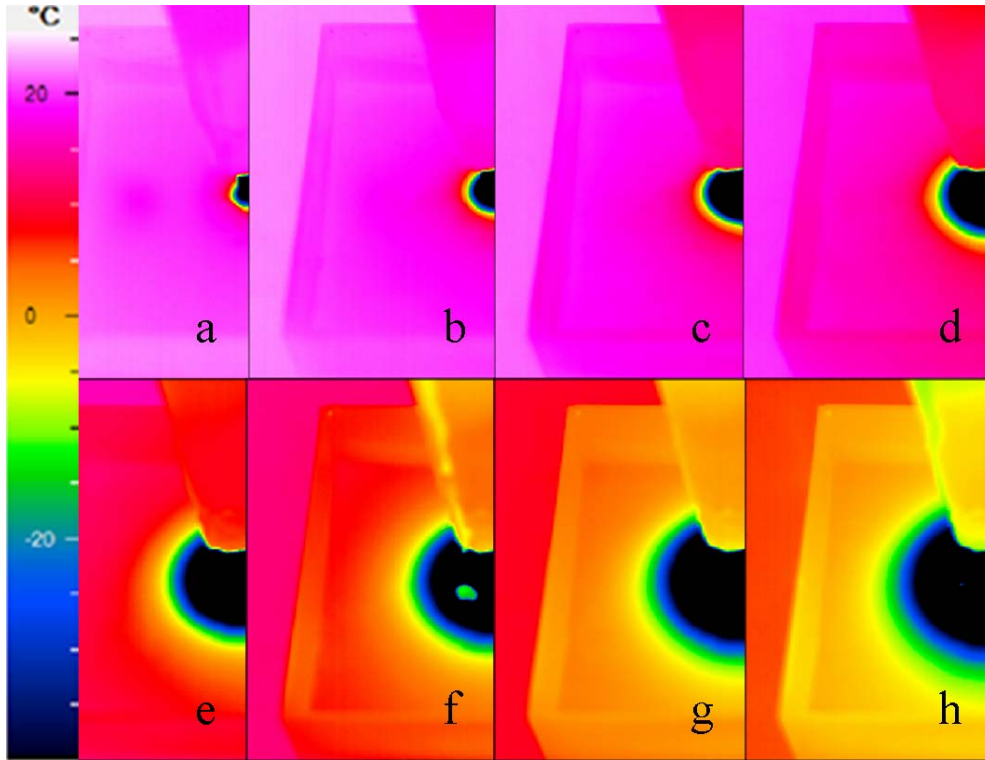
Figure 5.10 Symmetrical views of infrared thermographs of gelatin with a conventional cryoprobe. The temperature distributions from (a) to (h) are at 2 min, 4 min, 7 min, 11 min, 16 min, 22 min, 30 min and 40 min, respectively.

Tissue temperatures were monitored using an infrared thermography system. A conventional 6 mm diameter cryoprobe was inserted into samples to a depth of 2 cm. Tissue temperature contours captured from the gelatin phantom and porcine livers are shown in Figure 5.10 and Figure 5.11, respectively. Taking into account the symmetrical development of thermal profiles [20], only half-sections of infrared thermographic images are displayed. The complete ablation zone induced by cryo-freezing is then identified based on a critical temperature [36, 37] obtained from the images.
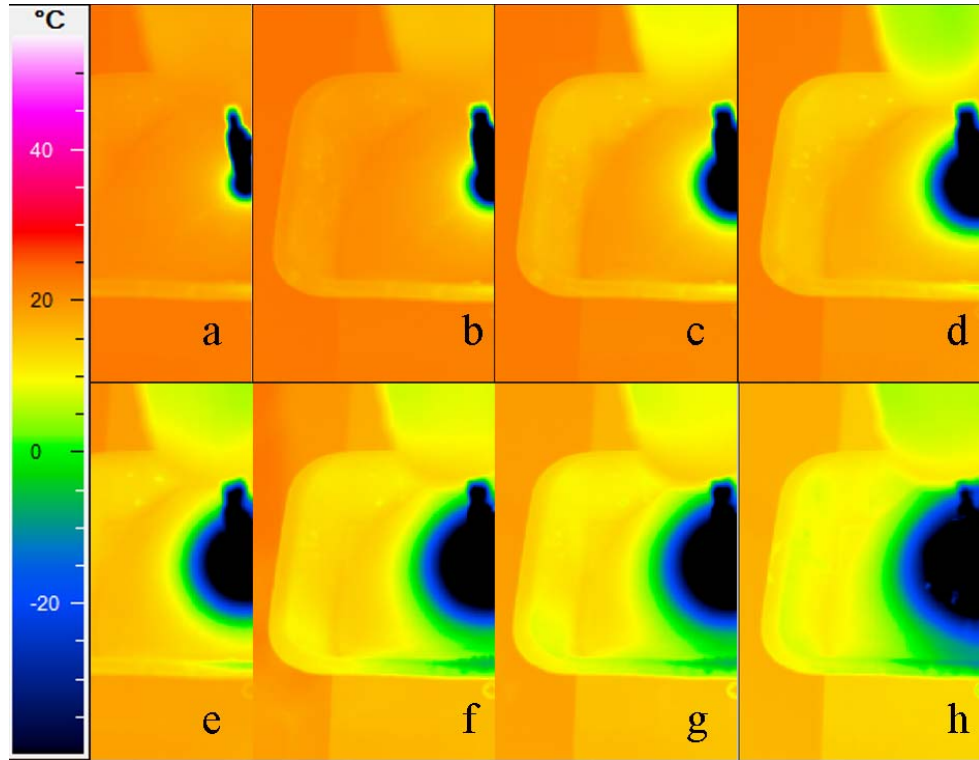
Figure 5.11 Symmetrical views of infrared thermographs of a conventional cryoprobe conducted in porcine liver. The temperature distributions are at 2 min, 4 min, 7 min, 11 min, 16 min, 22 min, 30 min and 40 min, respectively.

5.2.2. Model validation

The numerical simulation was conducted using the transient thermal module in Ansys Workbench 2.0. The mesh division is shown in Figure 5.12. Properties on porcine liver are widely available in literatures [4, 148, 149]. Table 5.3 lists typical model properties used in this dissertation.
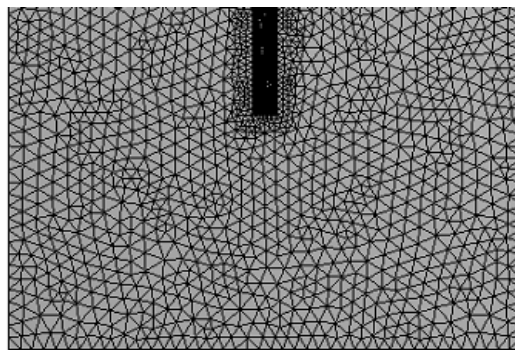
Figure 5.12 mesh division of numerical simulation. The mesh around cryoprobe is refined.

Table 5.3 The properties used in simulations

Thermophysical properties (unit)	Value	Ref.
Thermal conductivity of liver tissue, unfrozen ($W\,m^{-1}K^{-1}$)	0.5	[149]
Thermal conductivity of liver tissue, frozen ($W\,m^{-1}K^{-1}$)	1.76	[149]
Density of liver tissue, frozen ($kg\,m^{-3}$)	970	[28]
Density of liver tissue, unfrozen ($kg\,m^{-3}$)	1,000	[28]
Specific heat of liver tissue, unfrozen ($J\,kg^{-1}K^{-1}$)	1,673	[4]
Specific heat of liver tissue, frozen ($J\,kg^{-1}K^{-1}$)	3,347	[4]
Latent heat ($MJ\,m^{-3}$)	300	[35]
Metabolism of liver ($W\,m^{-3}$)	420	[150]
Blood perfusion heating effect, $\omega_b c_b$ ($kW\,m^{-3}K^{-1}$)	40	[35]

$$E = \frac{\sum\limits_{i=1}^{n}\left|\varphi_l^i - \varphi_l^{i-1}\right|}{\sum\limits_{i=1}^{n}\left|\varphi_l^i\right|} \tag{5.1}$$

A grid independence test was conducted to investigate the impact of using different grid sizes on the accuracy and stability. Simulations were performed with 21020 cells, 105308 cells and 150405 cells. Three thermocouples in each grid division were selected. The time step in each grid independence test was set to be 1 s. Variations between simulated and experimental data are compared by Eq(5.1). The metabolism and the blood perfusion terms are deactivated for the model validation since the experiments employed *in vitro* samples. The simulation errors are compared in Figure 5.13. Simulation with 21020 cells, 105308 cells and 150405 cells incur the largest difference of 9.4%, of 8.2% and 8.0%, respectively. It is apparent that when the mesh size increases from 105308 cells to 150405 cells, there is only marginal improvement on the model accuracy. With the balance of the computation time and model accuracy, the 105308 cells was chosen. Temperatures at the three predetermined locations between the simulated results and experimental data are used to calculate simulation errors. Errors of mesh resolution are shown in

Figure 5.14. The variations of temperatures at key locations in experiments are obtained by repeating four experiments conducted in *in-vitro* porcine livers under the same operating condition.
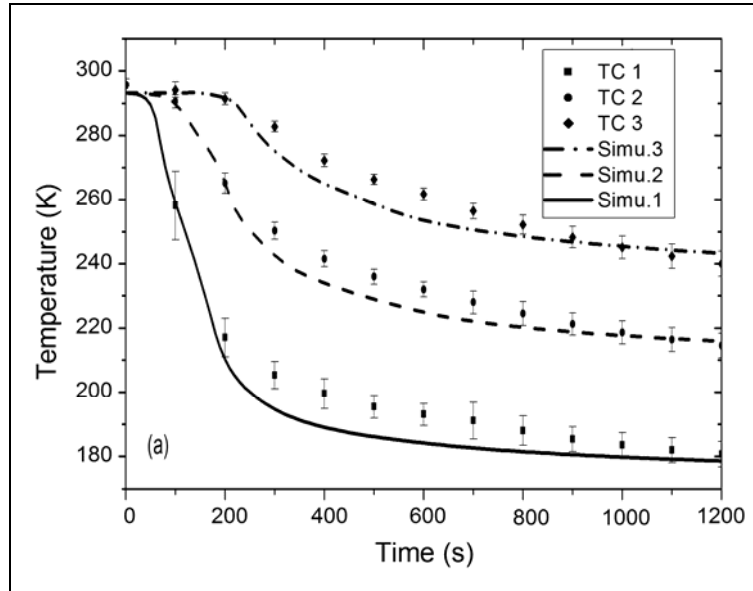
Figure 5.13 Model validation: temperature comparison at three predetermined locations between the simulated results with mesh B and experimental data.
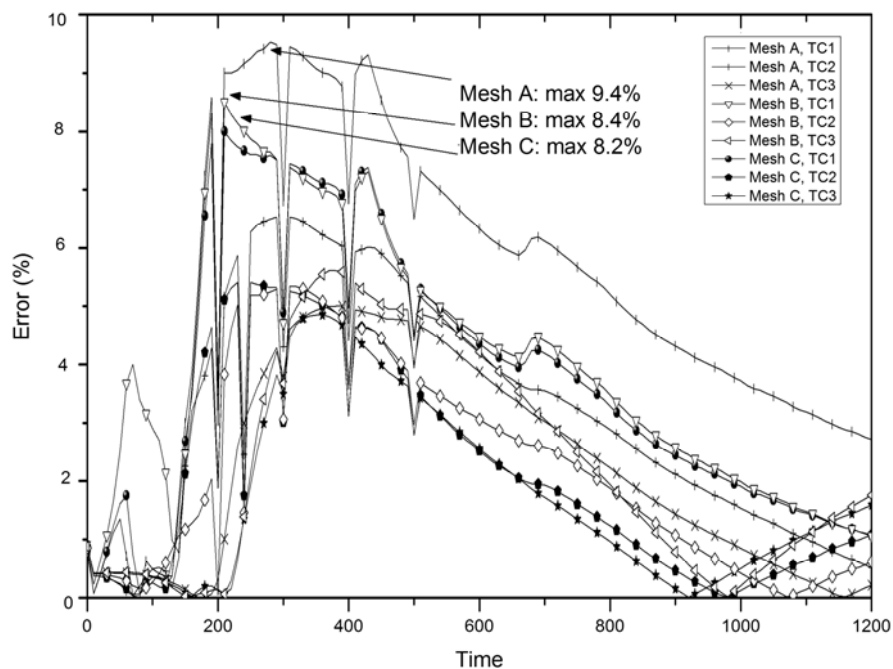
Figure 5.14 Model validation: errors in a grid independent test.

A three-dimensional bioheat transfer model is constructed with 105308 cells.

The moving ice front is identified based on the 265 K isotherm [118] and boundary of the complete ablation zone is derived from the 233 K isotherm [36, 37]. These two isotherms obtained from both experiments and simulations are compared in Figure 5.15.

Figure 5.15 validates the numerical model by making comparison between simulated and experimental data. Experimental data of 265 K and 233 K isotherm were derived from temperatures in thermographic images. Comparison illustrates that the deviations for the ice front and the complete ablation zone are 5.42 % and 4.82 %, respectively.
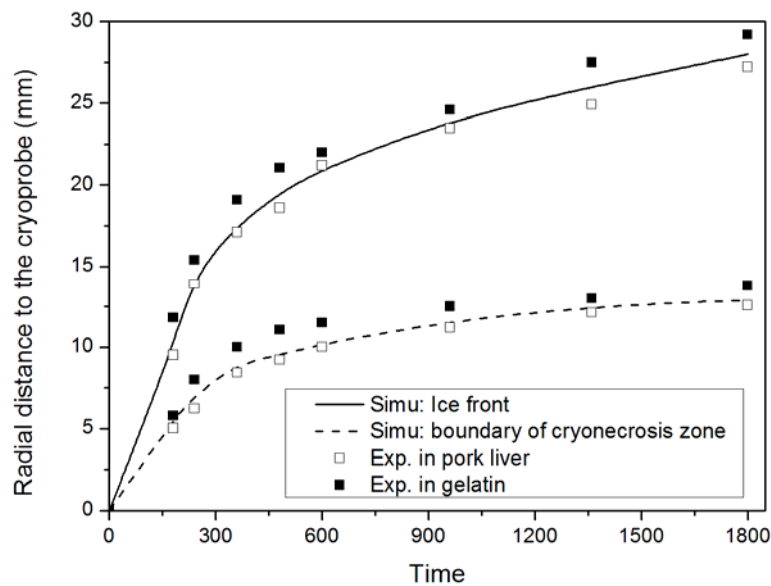
Figure 5.15 Development of the ice front and the boundary of the complete ablation.

Additionally, the gap distance between these two boundaries enlarged as freezing proceeded. For example, simulation results indicated that the gaps of the two radii are 7.5 mm at 240 s and 15.1 mm at 1800 s. The zone between the two isotherms can be referred to as an incomplete ablation zone. It is of great important to reduce the size of incomplete ablation zone.

5.2.3. Shape analysis of irregularly shaped ablation zone

A profile can be perceived as irregular if either its overall shape is irregular or it has an irregular border [88]. Figure 5.16 (a) shows four types of typical profiles. To identify the degree of irregularity, a shape factor known as "cryosurgery bulkiness (CB)" is introduced. The term "bulkiness" here characterizes the dynamics of rigid bodies and is capable of evaluating the overall shape of profiles [88, 89]. The CB is defined as $CB=V_{equ}/V_{tum}$. It characterizes the dynamic irregularity change of an isotherm. V_{tum} is the volume of the targeted tumor profile. V_{equ} is the volume of an equivalent ellipsoid. The equivalent ellipsoid is the minimum oblate spheroid covering the tumor with the consideration of the accessible insertion (main axis of the ellipsoid) of the cryoprobe. It is apparent that CB is no less than 1. When CB is close to 1, the targeted complete ablation zone is potentially well treated by a single conventional cryoprobe. When CB is very large, the targeted ablation zone is associated with a degree of irregularity. Therefore, the irregularity of the targeted ablation zone can be defined by $I_{rr}=1-1/CB$. For a better understanding of the term "CB", two examples with the same targeted profile are shown in Figure 5.16 (b) and Figure 5.16 (c). Figure 5.16 (b) has no limitation in the invasive direction while Figure 5.16 (c) is an extreme case that the invasive direction has to be vertical. Figure 5.16 (b) employs a smaller equivalent ellipsoid than Figure 5.16 (c) and the irregularity of the profile in Figure 5.16 (b) is smaller than the profile in Figure 5.16 (c).
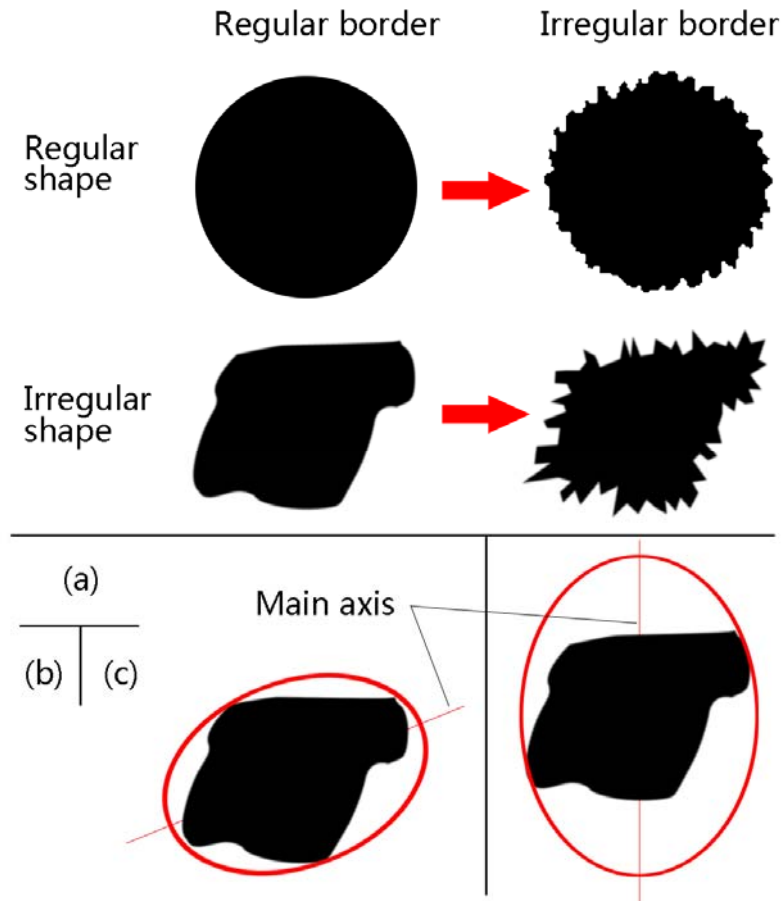
Figure 5.16 Classification of profiles and equivalent ellipsoid: (a). classification of profile in terms of border and shape; (b). the smallest external tangent ellipsoid; (c). the smallest external ellipsoid with a vertical main axis.

To investigate the thermal effect of cryoprobe, a prototype of bifurcate cryoprobe was fabricated. To investigate the ice formation of this cryoprobe, gelatin gel was used to provide semitransparent condition. The ice formation was visualized in Figure 5.17 at 600 s and 960 s.
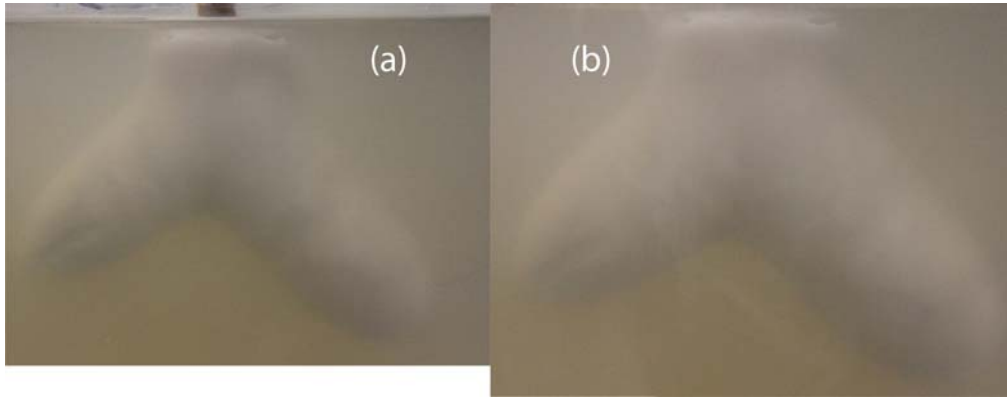
Figure 5.17 Visualization of ice formation for bifurcate cryoprobe. (a) freezing at 600 s; (b) freezing at 900 s.

Figure 5.18 shows developments of complete ablation zones induced by four cryoprobes. The temperature of cryoprobe at the initial stage in simulation was obtained from the experimental data. Temperature of the cryoprobe reduces to 123 K within 120 s. The rationale of bifurcate cryoprobe is to provide a compact design and easy procedure for cryosurgeons to employ. Cryosurgeon may apply these profiles by comparing them with solid tumors to decide a suitable bifurcate cryoprobe in the cryosurgical procedure. Results show that complete ablation zones increase with freezing durations in the direction of reducing their irregularities.
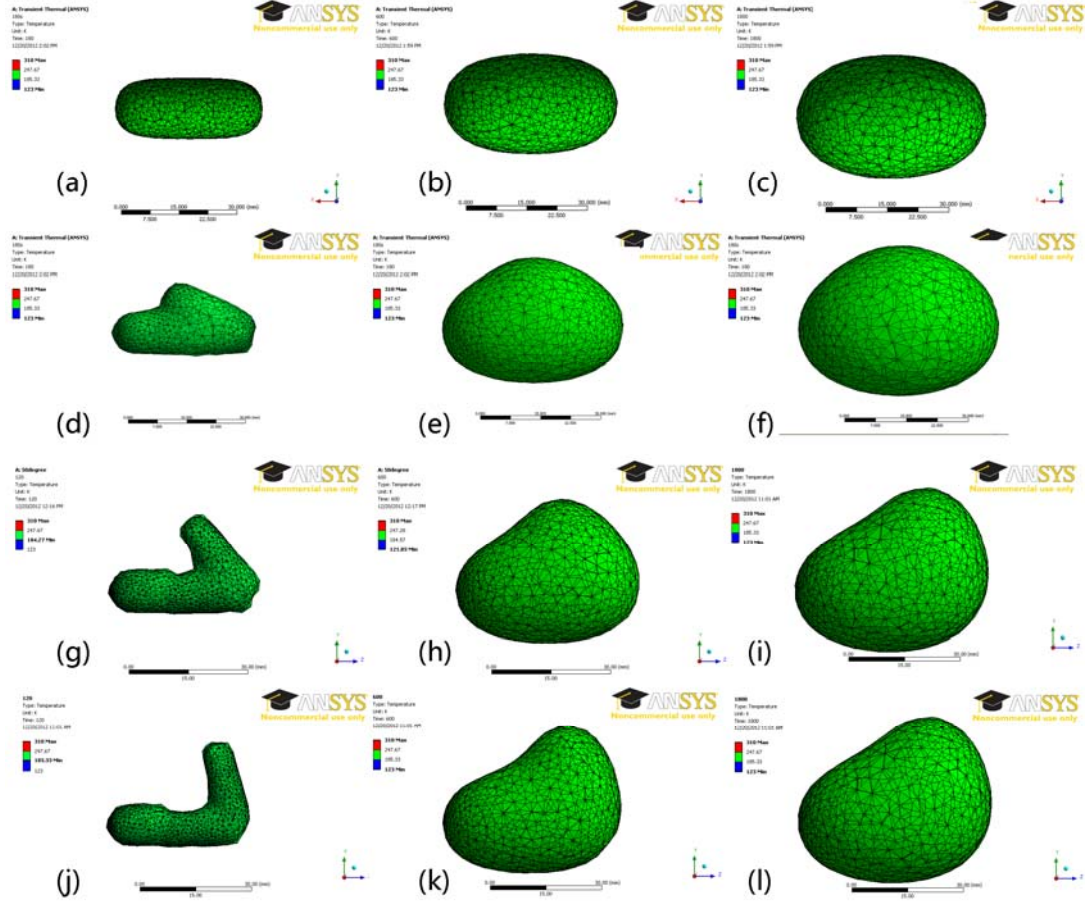
Figure 5.18 Development of the complete ablation zone (233 K isotherm): (a) a conventional cryoprobe at 120 s; (b) a conventional cryoprobe at 600 s; (c) a conventional cryoprobe at 1800 s; (d) a bifurcate cryoprobe β=25º at 120 s; (e) a bifurcate cryoprobe β=25º at 600 s; (f) a bifurcate cryoprobe β=25º at 1800 s; (g) a bifurcate cryoprobe β=50º at 120 s; (h) a bifurcate cryoprobe β=50º at 600 s; (i) a bifurcate cryoprobe β=50º at 1800 s; (j) a bifurcate cryoprobe β=75º at 120 s; (k) a bifurcate cryoprobe β=75º at 600 s; (l) a bifurcate cryoprobe β=75º at 1800 s.

The acute angle between the primary probe and secondary probe is denoted by β. When β is close to 0°, the bifurcate cryoprobe is in the folded state, whose profile is similar to a conventional cryoprobe. When β is close to 90°, the invasive procedure is not desirable as significant tissue need to be cut through. To study the performance of the bifurcate cryoprobe, we have selected three angles within the range from $0°$ to $90°$ for the purpose of illustration. Equal angular intervals were chosen to investigate the effects of varying β on the performance of the bifurcate cryoprobe. The chosen angles were $\beta=25°$, $\beta=50°$ and $\beta=75°$. Ablation zones generated by bifurcate cryoprobes were compared

with those produced by the conventional cryoprobe.
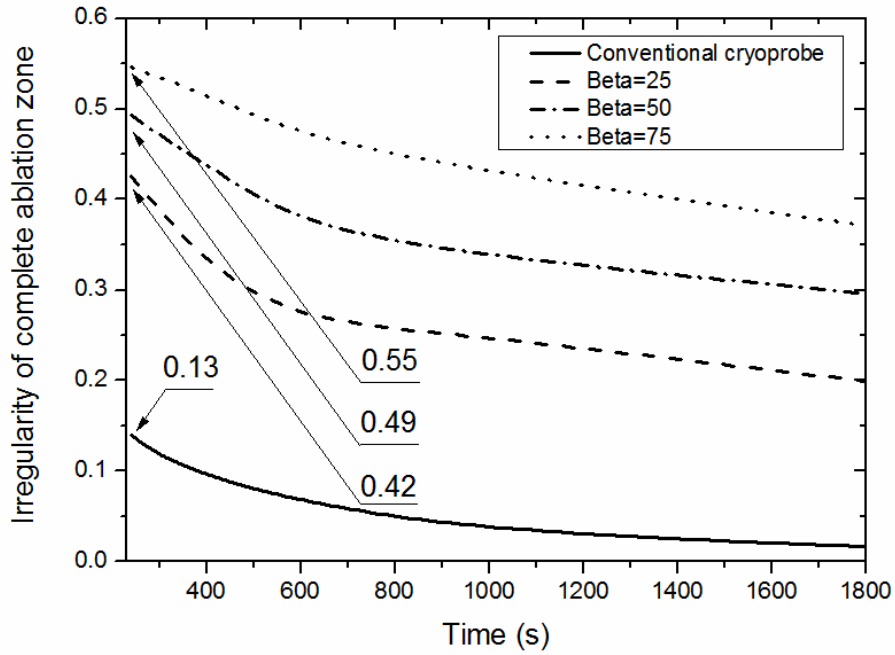
Figure 5.19 Comparison of the irregularities of complete ablation zones
produced by four cryoprobes.

Figure 5.19 computes and compares the irregularities of complete ablation zones. These complete ablation zone were produced by a conventional cryoprobe and three bifurcate cryoprobes. Comparatively, the complete ablation zone induced by the bifurcate cryoprobe has significantly higher irregularity than the one induced by the conventional cryoprobe. Among the four cryoprobes, the complete ablation zone generated by the bifurcate cryoprobe β=75° achieves the highest degree of irregularity, producing about 4.4 times higher level of irregularity than the conventional cryoprobe at 600 s. Furthermore, the irregularity is inversely related to the freezing duration. The bifurcate cryoprobe β=75° can reduce I_{rr} from 0.55 at 200 s to 0.37 at 1800 s.

5.2.4. Invasive damage induced by bifurcate cryoprobe

Figure 5.20 shows the sizes of complete ablation zones at the symmetric plane for four cryoprobes. It is apparent that bifurcate cryoprobes are capable of generating larger complete ablation zone than the conventional cryoprobe. Bifurcate cryoprobe with $\beta=75°$ produced the largest complete ablative area of 1703 mm^2 at 1800 s, whereas the conventional cryoprobe only produced 1127 mm^2 at the same freezing time which translates to an improvement of 51.1% greater coverage.
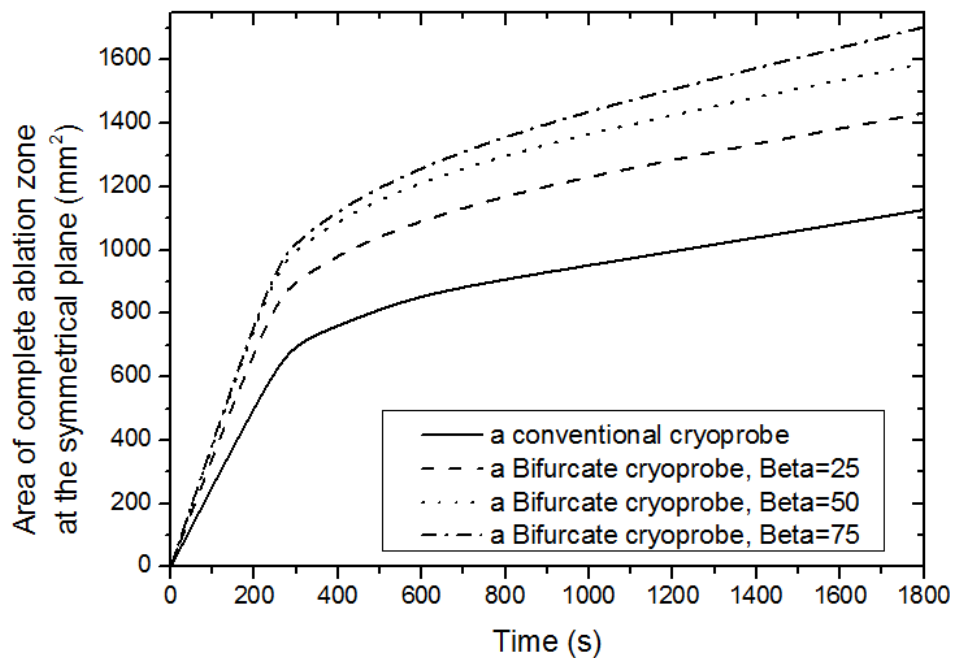
Figure 5.20 sizes of complete ablation zones at the symmetrical plane.

An in-depth examination of tissue injury indicates that the total tissue damage contains a large portion of thermal damage and a small portion of the invasive trauma. The invasive trauma refers to the tissue damage due to the process of the cryoprobe implant.It is, measured by the volume cut during the transformation of bifurcate cryoprobe. The invasive trauma is a method to compare the performance of bifurcate cryoprobe with different degree of transformation. Although bifurcate cryoprobes have the distinct advantage of generating large freezing zones with high degree of irregularities, compared to

83

conventional cryoprobes, they induce large invasive trauma.
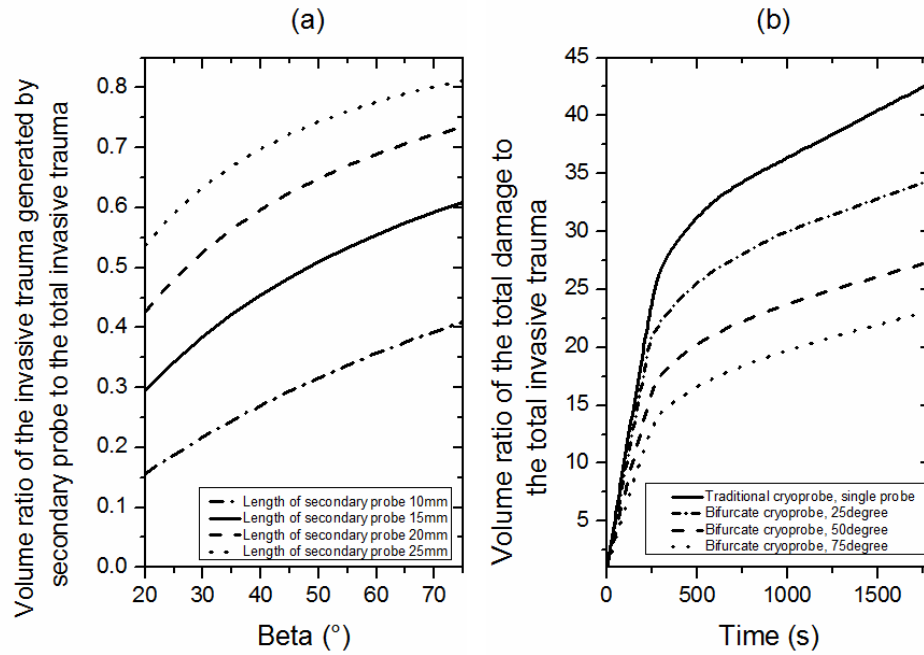
Figure 5.21 (a) Volume ratio of the invasive trauma generated by the secondary probe to the total invasive trauma; (b) Volume ratio of the total damage to the total invasive trauma produced by one conventional cryoprobe and two bifurcate cryoprobes.

As β increases, the secondary probe unfolds at greater angles necessitating more incision through tissue for it to reach the targeted position. As far as cryosurgery, characterized by its minimally invasive nature, is concerned, higher levels of invasive trauma is undesirable as patients experience more bleeding and pain. Therefore, the level of invasive trauma is studied. Figure 5.21 (a) shows the volume ratio of the invasive trauma generated by secondary probe to the total invasive trauma (primary and secondary probes) against β. The length of the active freezing cryoprobe is 30 mm. The lengths of secondary probes are 10 mm, 15 mm, 20 mm, and 25 mm, respectively. Results showed that the volume ratio increases at a large β and a long designed length of secondary probe. Figure 5.21 (b) depicts the volume ratio of the total damage to the total invasive trauma. When the probe is placed in tissue, the volume ratio is around one as the total volume damage closely equals to the

invasive trauma. Once the freezing is initiated, the tissue around the probe is injured. Therefore, the volume ratio is interpreted as the magnitude of total damage that the cryoprobe has generated based on the volume of invasive trauma.

Computed volume ratios for a conventional cryoprobe and three bifurcate cryoprobes are compared in Figure 5.21 (b). Results show that the total damage is 41.8 times higher than the invasive trauma induced by the conventional cryoprobe. In contrast, the values for the bifurcate cryoprobes at $\beta=25°$, $\beta=50°$ and $\beta=75°$ are only 33.5, 26.4 and 22.2, respectively. The chief reason why generally bifurcate cryoprobes have lower ratios is because they induce greater invasive trauma. Based on the simulation results in Figure 5.20 and Figure 5.19, it is conclusive that of the three bifurcate cryoprobes studied, the one with $\beta=75°$ generates the greatest tissue damage with the highest irregularity but incurs the penalty of higher invasive trauma compared to the total tissue damage.

5.3.   Thermal effects on the clinically-extracted vascular tree

Large vessels in a complex blood network are important for cryosurgery. The thermal functionality of the blood circulatory system depends on the structure and flow arrangement. Due to the irregular branching pattern of blood vessels, the simulation was constructed with a clinically-extracted vessel network. The freezing duration, relative distances to vessels, blood flow rates and sizes of blood vessels were investigated in determining the optimized outcome of the cryo-ablation. This section provides surgeons with essential information on how to tune key parameters to promote success rate of cryosurgery.

5.3.1. Extract the blood vessel network

A clinical procedure for the cryosurgery planning in this section is described as follows:

(a). Obtain the vascular image to localize blood vessels. This can be achieved by CT angiography after injecting non-ionic contrast medium. The contrast medium flows through a catheter positioned in a vessel that feeds the tumor [151]. Many technologies have been employed to reconstruct organ vessels [21, 52, 53].

(b). Import the image(s) to an external workstation for the mesh reconstruction, identifying the blood vessels and the tumor. The cryoprobe is positioned at the center of exterior contact circle of the tumor.

(c). Install the boundary conditions (i.e. blood flow rate) and the various thermal properties used in the model.

(d). Simulate cryosurgical process and monitor the development of temperature contours. Identify the duration that the targeted isotherm covers the profile of tumor.
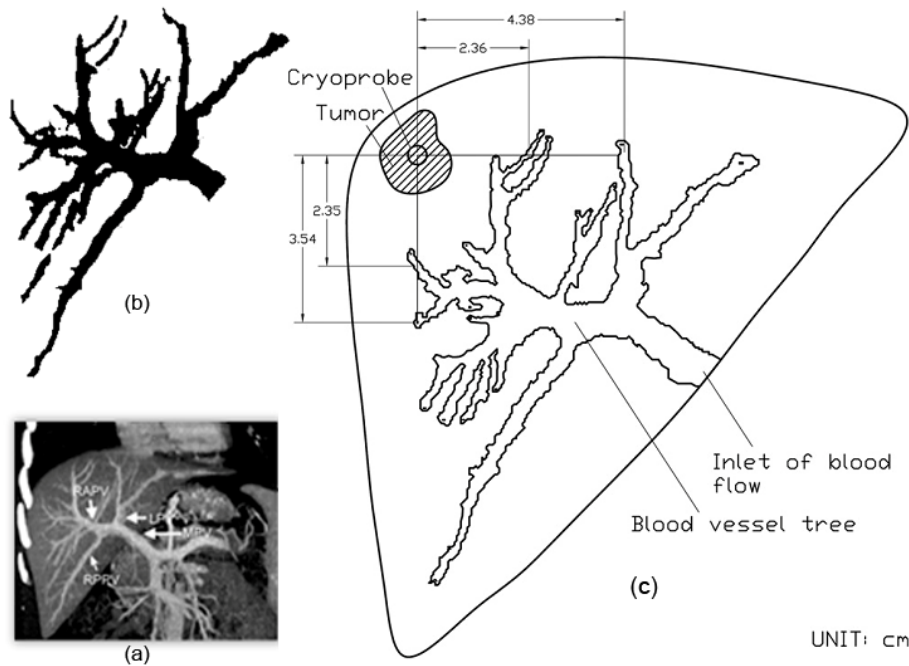
Figure 5.22 Schematic diagram of 2D biological model embedded with a clinically

86

extracted vascular tree.(a). CT image of 31-year-old patient [152]; (b) extracted large vessels; (c) simulation domains.

The model was applied to simulate the cryosurgical process of a 31-year-old patient with hepatic vascular network [152]. A 16-detector row CT scanner (LightSpeed, GE Medical Systems, Milwaukee, WI) was employed to detect the structure of blood vessels. A contrast-enhanced multiphasic scanning was used after injecting non-ionic contrast medium (iohexol, Omnipaque 350, GE Healthcare) into the antecubital vein. The image was processed and digitized the boundary of the vascular tree. The schematic diagram of simulation is shown in Figure 5.22. The blood flow inlet is at the root of blood vessel tree and outlets are at tips of the branches. Commercial software Fluent 6.3 was used to simulate the thermal development during cryosurgery.

5.3.2. Model validation

Experimental samples for model validation are displayed in Section 4.1.5. In the first part of this section, we validate the model with one direction flow. To enhance our model validation, we also conduct the counter-current model validation and *in-vivo* model validation. Experiments conducted with porcine livers showed that the temperature of cryoprobe stabilized at 123 K with a freezing duration of 120 s. The tissue and blood properties applied to the model are listed in Table 5.3. To reduce errors, the experiments are repeated four times with variances portrayed in error bars in Figure 5.23.
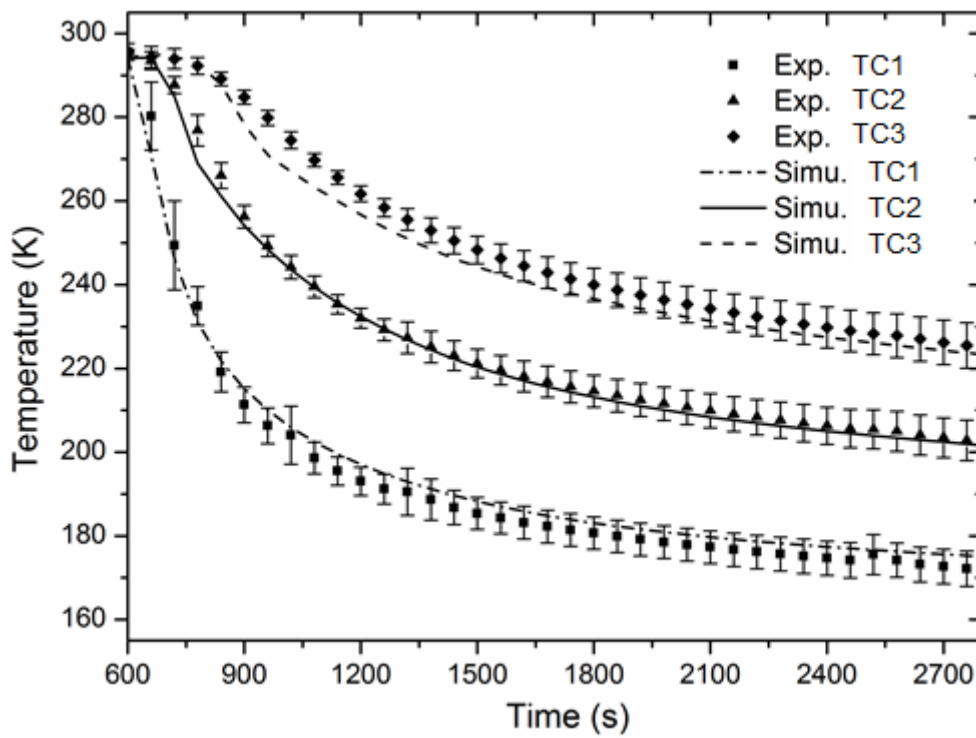
Figure 5.23 Numerical model was validated with experimental results at TC 1, TC2 and TC3 with a blood flow rate of 1000 ml/min. The time step of simulation was selected as 1 s with 858822 cells.

Gird independence tests were conducted to enhance the model sensitivities in response to different mesh sizes. Temperatures at three points in each mesh cell are selected to compute the maximum errors in Table 5.4. The time step of each grid independence test was designed at 1 s and the simulated duration was 2520 s.

Table 5.4 Errors in the gird independence test. TC: thermocouple.

	Position	Max. Error	Time
858822 Cells	TC 1	3.33%	60s
	TC 2	2.85%	180s
	TC 3	3.22%	360s
524983 Cells	TC 1	5.32%	60s
	TC 2	3.66%	200s
	TC 3	7.18%	400s
300985 Cells	TC 1	5.44%	60s

TC 2	4.1%	190s
TC 3	8.28%	380s

Comparative results indicate that a refined mesh size reduces the simulation difference. The model agrees well with the experimental data by adopting the mesh size of 858822 cells.

The model validation is also conducted by perfused liver with countercurrent flow. The temperature of countercurrent flow was controlled at 310 K. The countercurrent flow can be identified in Figure 5.24(a), (c) and (d).
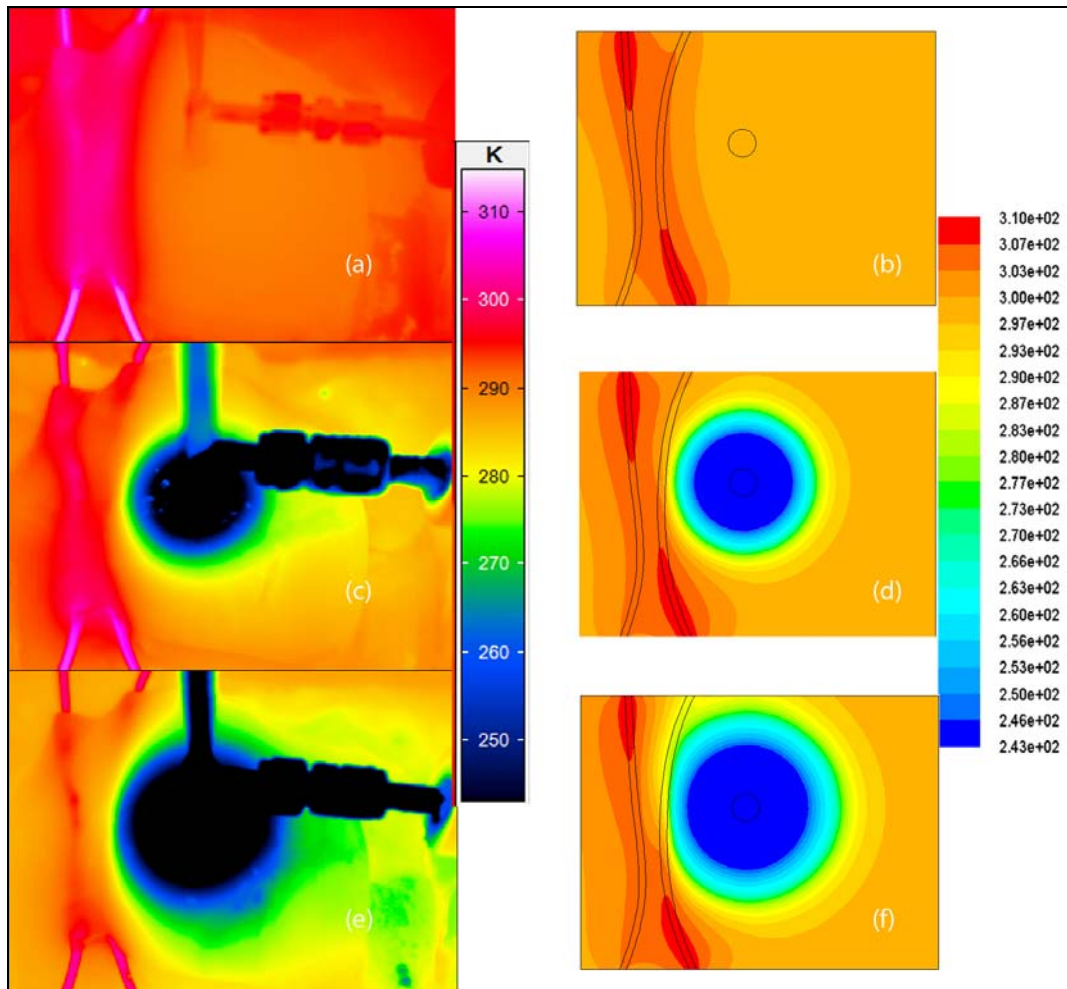
Figure 5.24 Comparison of experimental data and simulated results. (a) and (b) show the temperature distributions 15 min after initiating countercurrent flow ; (c) and (d) are at 10 min after the commencement of freezing; (e) and (f) are 20 min after the commencement of freezing. (a), (c) and (e) are the experimental results captured by infrared camera; (b), (d) and (f) are the corresponding simulated results

The simulation was constructed with the same dimensions as shown in the experiments. The *in-vitro* simulation contain 653043 meshes. The freezing process was initiated 15 min after the water flow circulation. Temperature contours at 15 min, 25 min and 35 min was shown in Figure 5.24 (b), (d) and (f). To quantify the validation, we compare the distance between the ice front and the cryoprobe. The result is shown in Figure 5.25
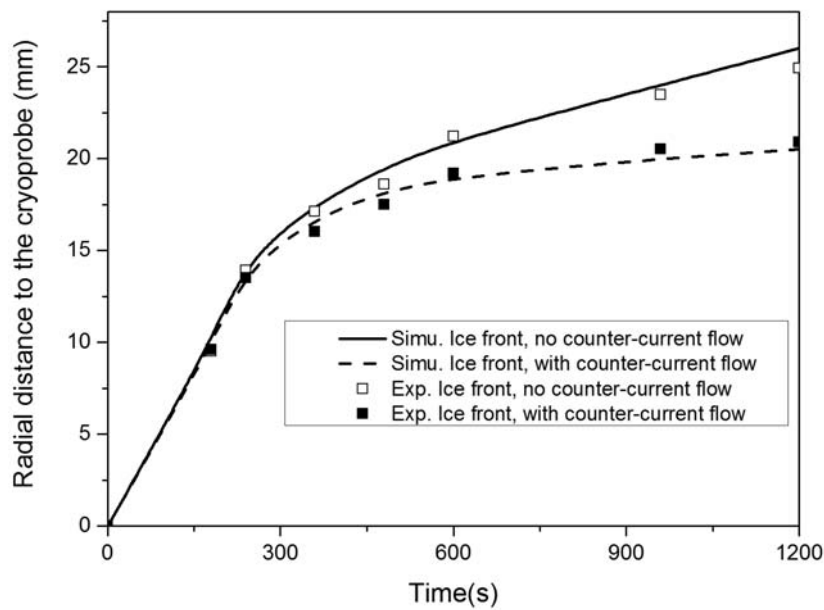
Figure 5.25 model validation by the ice front with counter-current flow and without counter-current flow.

The model is also compared with experimental data from *in-vivo* porcine liver samples. We use the data from an existing article [7] to validate the model as shown in Figure 5.26. The figure shows that the simulated data has a good agreement with data obtained from the reference. The largest error is found in the temperature reading of TC1. The largest error was found to be 5.6 %.
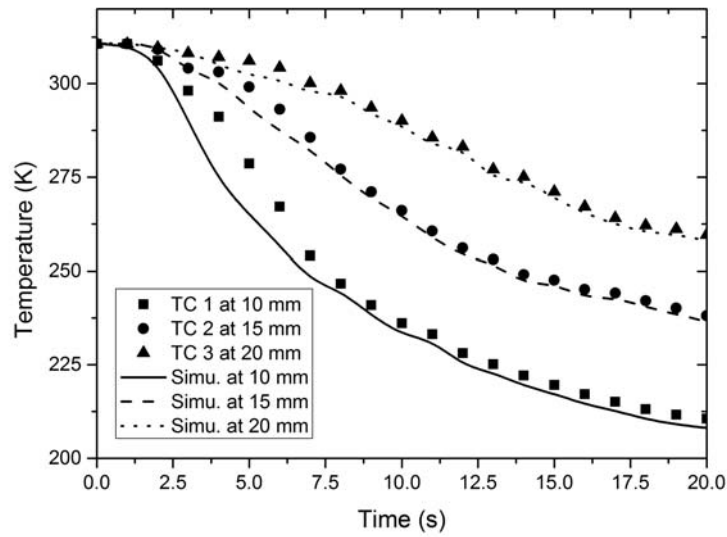
Figure 5.26 Model validation by in-vivo experimental data.

5.3.3. Temperature contours during cryosurgery in vascular tissue

The validated model was applied to investigate the thermal development of a liver tumor surrounded by complex blood vessels. The initial temperature of biological tissue was 305 K while the inlet temperature of blood flow was 310 K. The diameter of the cryoprobe in simulations was 4 mm. The body fluid around the liver was 305 K. The mass flow rate of the blood in the model was 1000 ml/min [153]. It was maintained for 10 min before the commencement of freezing. The temperature contours at 9 min, 15 min, 25 min and 40 min are shown in Figure 5.27. The dotted line shows the boundary of vascular tree. As the freezing proceeded, the cryoprobe exerted greater freezing effects on the region associated with fewer vessels.
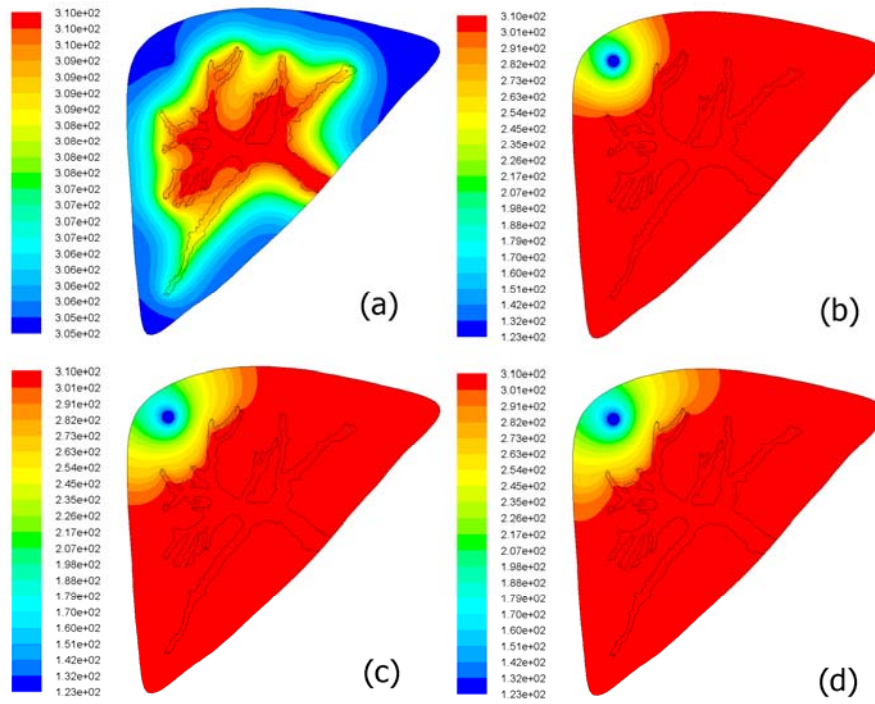
Figure 5.27 Transient study of temperature contours with a blood flow rate at 1000 ml/min. (a) temperature contour at 9 min, (b) temperature contour at 15 min, (c) temperature contour at 25 min, (d) temperature contour at 40 min.

The cross-sectional temperature distributions help to demarcate the complete ablation zone by monitoring isotherms at the critical temperature. The 233 K and 273 K isotherm are identified in Figure 5.28. The 273 K isotherm is observed to be 11 mm at 15 min and it potentially extends to 25 mm within 40 min.
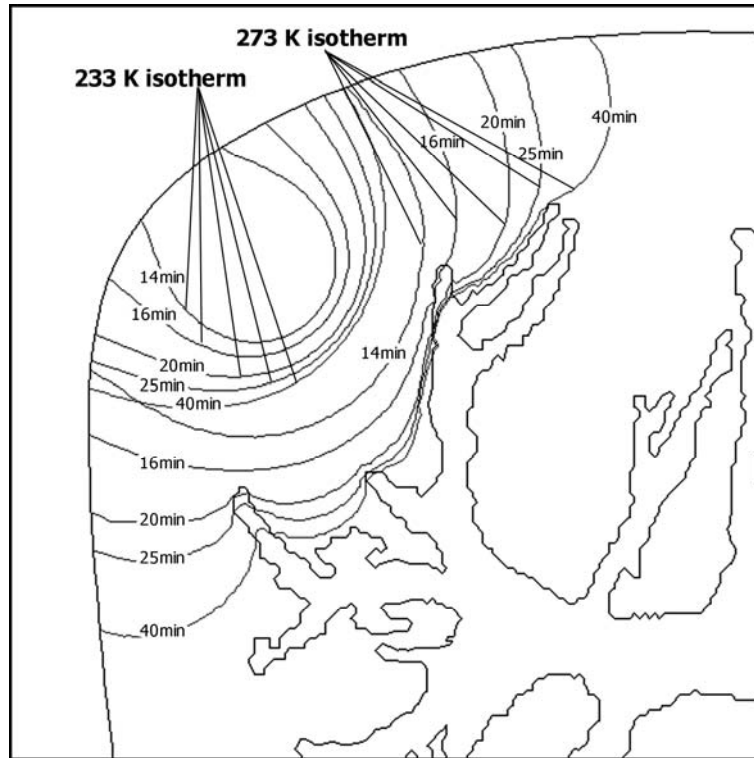
Figure 5.28 The development of 233K and 273K isotherm when the blood flow rate is 1000 ml/min. The freezing is initiated at 10 min.

Studies have shown that a portion of cells near the edge of the frozen zone survive because they experience only extracellular cell destruction [42]. The critical temperature was chosen as 233 K, which is believed to be sufficient to destroy tumor cells permanently [154, 155]. Figure 5.28 shows that 2.87 cm^2 complete ablation zone is formed at 16 min. The size of the complete ablation zone extends to 5.18 cm^2 at 40 min's freezing, inducing 44.6 % undesired ablation. In other words, the case study shows that it is possible to protect healthy tissue by 44.6 % of the size of ideal complete ablation.

5.3.4. Influence of blood flow on freezing

The total hepatic blood flow rate has been observed to be significant and it can account for approximately a quarter of the total cardiac output at rest [156]. The amount of flow rate in fact varies substantially. For example, the increase

in maximal hepatic blood flow after a meal could vary from 20% to 70% [157, 158]. Other study concluded that flow rates were around 1000 ml/min [153]. Therefore, it is reasonable to assume that the typical blood flow rate spans 600 ml/min to 1200 ml/min. The temperature contours in response to blood flow rates are compared in Figure 5.29.
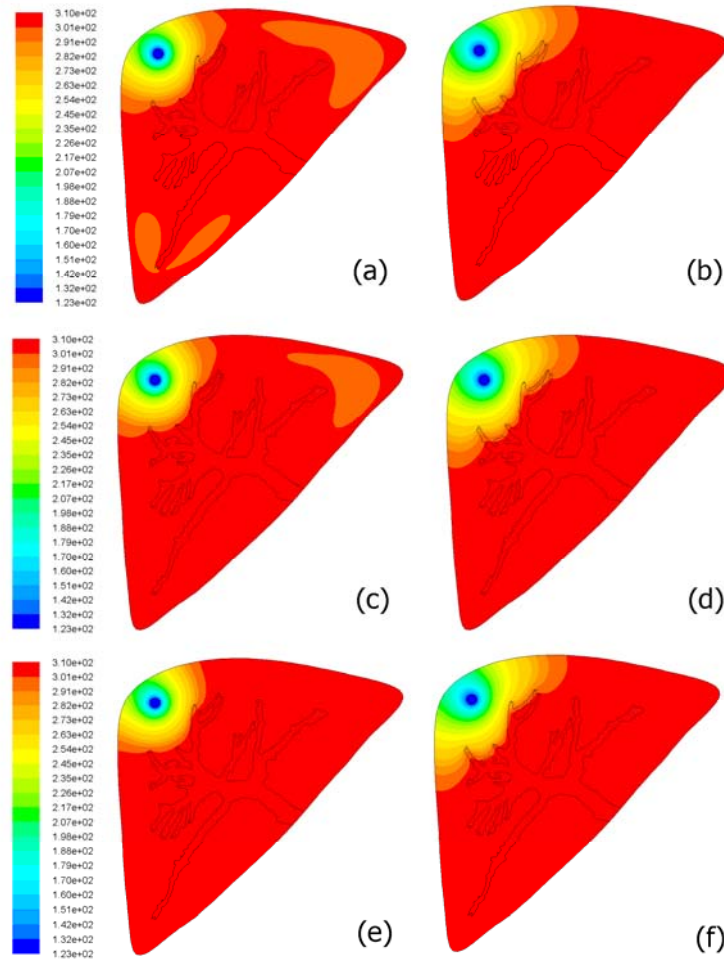
Figure 5.29 Influence of the blood flow rate on the temperature development. (a) 600 ml/min at 15 min; (b) 600 ml/min at 40 min; (c) 800 ml/min at 15 min; (d) 800 ml/min at 40 min; (e) 1200 ml/min at 15 min; (f) 1200 ml/min at 40 min.

With different blood flow rates, it is found that only subtle influence on the growth of 233 K isotherm in this vascular structure. It is apparent that a decrease in blood flow rate with a long freezing duration permits the cryoprobe to generate greater thermal injuries. The blood vessel with large flow rate exerts greater influence on how the frozen tissue can be shaped

externally.
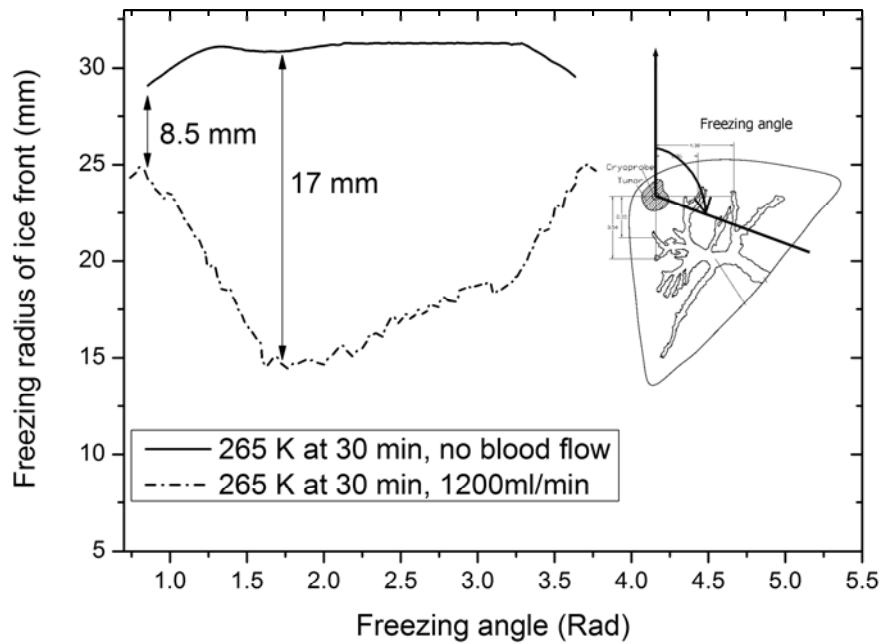
Figure 5.30 Thermal effects of blood flow on 265 K isotherm across freezing angles with a freezing duration of 30 min.

5.3.5. Vascular effects on the ice front and 233 K isotherm

To better understand the temperature development in an inhomogeneous and anisotropic tissue during cryosurgery, two parameters, a freezing radius and a freezing angle, are used to measure and compare the profiles of isotherms at targeted temperatures. The freezing radius refers to the distance between the cryoprobe and a point along the isotherm while the angle between two freezing radiuses is defined as the freezing angle. As shown in the previous section, the flow rate of hepatic flow is around 1000 ml/min[153] and with the range varying from 20% to 70%[157, 158]. To investigate the effect of a vascularized blood system on the isotherms, we compute the freezing angles at specific temperature isotherms with a blood flow rate of 1200 ml/min as illustrated in Figure 5.30. The solid line, graphed in Figure 5.30, presents the

265 K isotherm in the absent of blood network while the dotted line is the 265 K with a blood flow of 1200 ml/min. The vascular heating effects reduced freezing radius from 31 mm to around 20 mm. The minimum 265 K isotherm with 1200 ml/min blood flow is 14 mm with a freezing angle of 1.7. The range of difference between the two cases is 17 mm and 8.5 mm respectively.
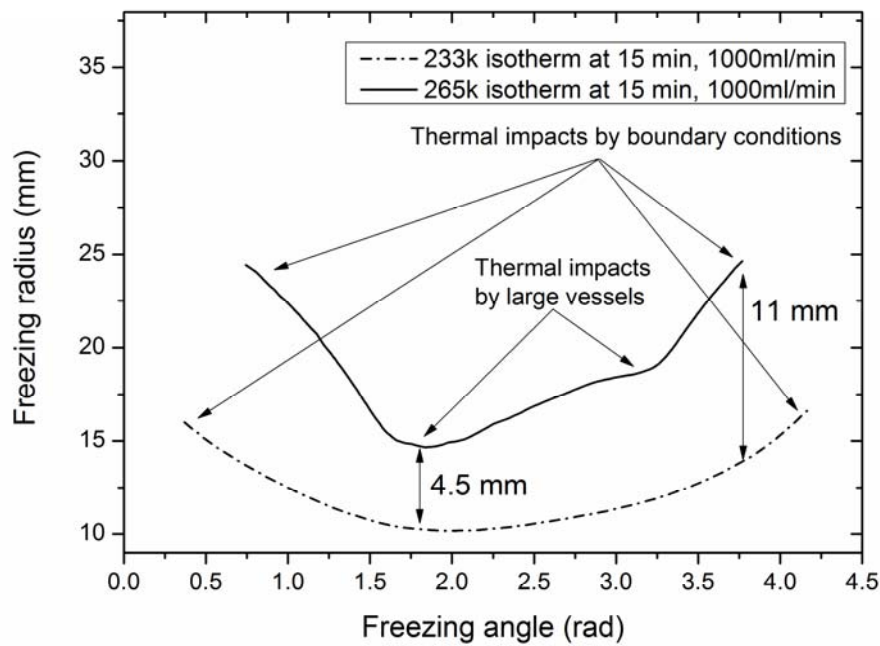
Figure 5.31 Freezing radius versus freezing angle at a flow rate of 1000 ml/min at a freezing duration of 15 min.

Figure 5.31 shows the freezing radii in response to varying freezing angles. It is apparent 233 K isotherm is more uniform than 265 K isotherm. This implies that the neighboring vessels generated less thermal impacts on 233 K isotherm. Results show that dominant vessels influence the distance between the 233 K and 265 K isotherms varying from 4.5 mm to 11 mm within a freezing duration of 15 min.

There is no vascular heating within a complete frozen zone (i.e. 265 K). The zone between the 233 K isotherm and 265 K isotherm can be treated as a

thermal "buffer zone". The buffer zone, siting at the periphery of 233 K isotherm, is considered with no vascular effects and reduces the thermal influence due to blood flows in the unfrozen zone. Figure 5.31 illustrates how the vascular structure affects the irregular gap between the 233 K isotherm and 265 K isotherm. Large vessels have largely reshaped freezing radii at 265 K isotherm; however, they only induce marginal thermal impact on the freezing radii at 233 K isotherm. The present of "buffer zone" decreases the vascular effects on 233 K isotherm.

Chapter 6: Cryosurgery with Peripheral Joule Heating Elements

The complete eradication of all tumor cells while inflicting minimal collateral cryoinjury to the surrounding healthy tissue is the key wish-list of cryosurgeons. However, the minimal invasive nature of cryosurgery at times generates clouds of uncertainty in identifying the boundary of complete ablation zone, resulting in a large probability of recurrence [159]. A well-controlled cryosurgical process needs the knowledge of deleterious effects of low temperatures on cells. In this chapter, the Joule heating elements are incorporated into cryosurgery to reduce the undesirable cryoinjury.

6.1. Classification of tissue cellular state and tissue phase

The degree of cell damage largely depends on the variation of temperature. A minor temperature change only causes an inflammation but a drastic temperature difference leads to the tissue destruction due to protein denaturation [139] and intracellular ice crystallization [95]. In terms of phase demarcation during tissue freezing, a frozen region, a mushy region and an unfrozen region are identified while the complete ablation zone, the incomplete zone and the thermally unaffected zone are differentiated based on the cellular functionality.
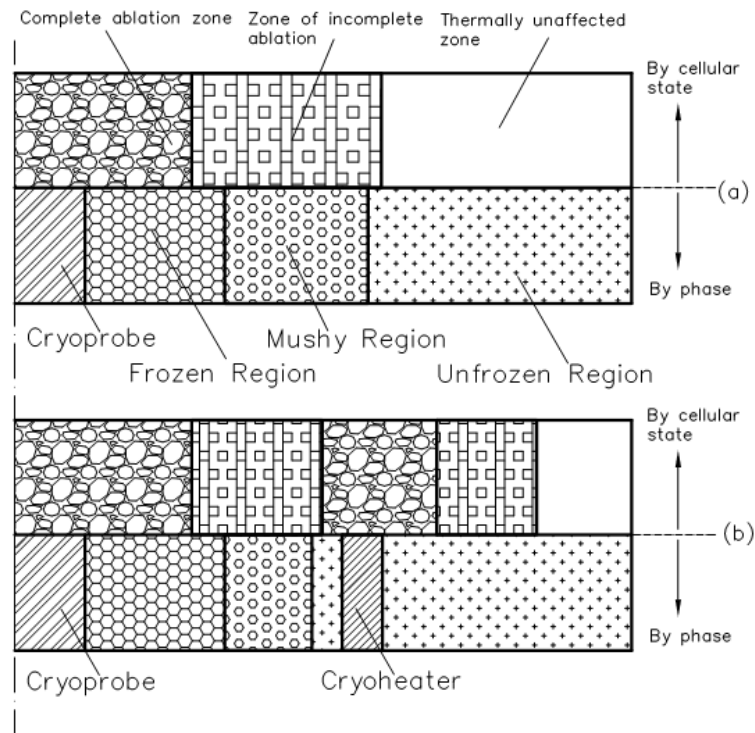
Figure 6.1 Symmetrical diagram of the tissue classification by phase demarcation and cellular states: (a) a conventional cryoprobe; and (b) a hybrid cryoprobe.

Figure 6.1 shows the classification of these zones. The divisional zones in a tissue undergoing freezing due to a cryoprobe are shown in Figure 6.1(a). The complete ablation zone arising from the inflicted thermal injury is located within the frozen region while the incomplete ablation zone contains the mushy region, a section of the frozen region and a part of the unfrozen region. Figure 6.1 (b) highlights the zone variation when a heating probe is introduced to the mushy region, which is allocated at a distance to the cryoprobe. In this case, an additional complete ablation zone may evolve due to the effect of hyperthermia. One chief goal of proposing a hybrid cryoprobe with Joule heating element is to minimize the incomplete ablation zone and maximize the coverage of the complete ablation.

6.2. Reducing the unwanted frozen zone for internal tumors

In this section, a hybrid cryoprobe is proposed to promote surgical efficacy by improving tumor ablation while reducing the unwanted cryoinjury. The thermal impacts of employing the hybrid cryoprobe on tissue temperature distributions have been studied. Evaluating the control ability, we have simulated the thermal impacts of the device. To evaluate the performance of the probe operating under cyclic freeze-thaw conditions, a detailed bioheat transfer model incorporating tissue death functions is applied. The performance of hybrid cryoprobe potentially leads to a portable and cost-effective device that may prove beneficial for the purposes of surgical planning, rehearsal and control.

6.2.1. Experiments and model validation

The experiment setup of this section has been described in Section 4.2.4.2. In contrast to freezing, the implementation of an active heating device requires more precise controls within a specific duration. Excessive heat is highly undesirable: it can dry up the tissue and induce charring. In the initial phase of experiments, eight experiments were conducted to determine the appropriate heating power for tissue heating/thawing. Of the eight experiments, four with lower heating powers of up to 19 W were observed to be suitable for clinical application. The other four with higher powers spanning 20-24 W induce a distinct coagulation region between the tissue and heater. Figure 6.2 illustrates several cross-sectional views of *in vitro* porcine liver samples after thermal ablation is administered by cryoheaters.
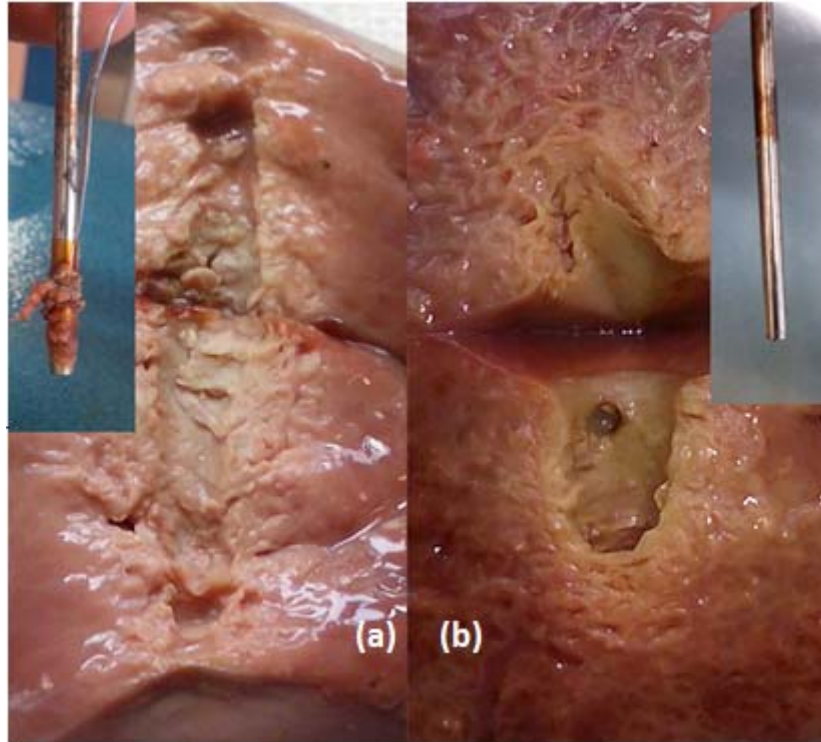
Figure 6.2 Experimental observations of *in vitro* porcine liver samples after the heating with their corresponding cryoheaters plugged out. Figure (a) and (b) are conducted with heating fluxes of 24 W and 19 W, respectively.

During the 24 W test, the cryoheater temperature reached the maximum temperature of 413 K while the 19 W test achieved the maximum temperature of 371 K. We further observed that the tissue in the vicinity of 24 W cryoheater became markedly dehydrates and subsequently stiffens. Tissue detachment was so considerable that a part of tissue could be tore off. This "sticking" phenomenon was also observed by Karin and co-researchers, claiming that the sticking tissue distorts the electrodes [146].

The model was first validated with *in-vitro* data generated from our experimental test-rig in Section 4.2.4.2. The porcine liver properties [4, 28, 35, 149, 150] applied to the simulation model are listed in Table 5.3. The transit thermal module in Ansys 12.1 was used to simulate the thermal process.

In the model validation, heating and freezing processes were conducted

separately using porcine liver samples. The respective heating and freezing durations were 600 s and 1200 s. The temperatures of thermocouples were collected at every 10 s. Heating and freezing processes were repeated 4 times to determine systematic errors. We compare experimental and simulated results in Figure 6.3. Variability of each experiment is represented by error bars.
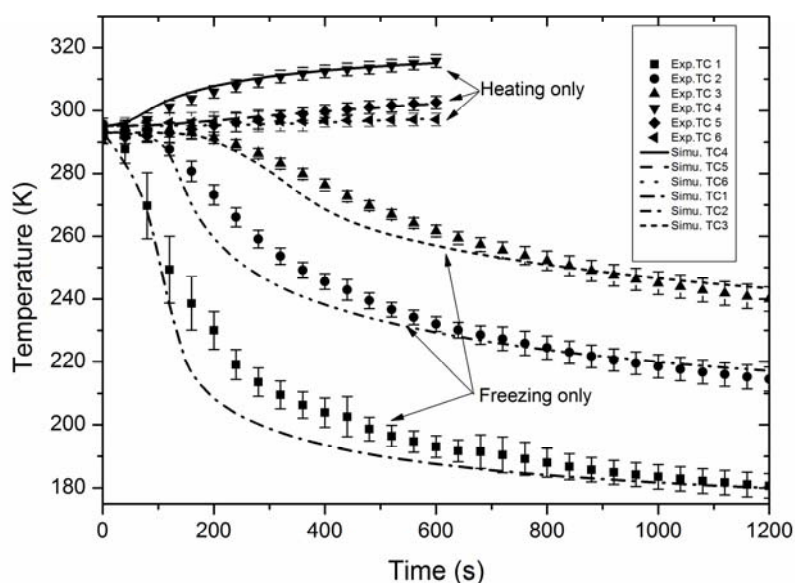
Figure 6.3 Model validation with thermocouple readings. Lines are the simulated results while points are experimental data. TC: thermocouple.

A grid independence test was conducted to establish the impact of using different grid sizes on the accuracy and stability. Simulations were performed with 117720, 196206 and 99457 cells. Three thermocouples in each grid division were selected. The time step in each grid independence test was set to be 1 s with a total duration of 1200 s. Variations between simulated and experimental data are duly compared and shown in Figure 6.4. Largest temperature variances for freezing and heating for the finest mesh (196206) are observed to be 6.73% and 2.7%, respectively.
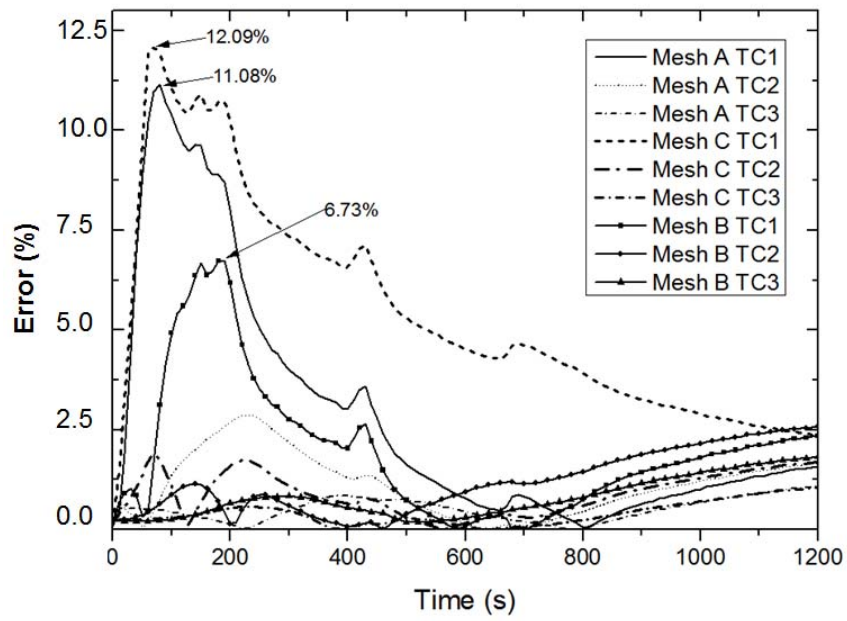
Figure 6.4 Errors in grid independence tests in response to time. Mesh A: 117720 cells, Mesh B: 196206 cells, Mesh C: 9945 cells.

6.2.2. Layout of the simulation
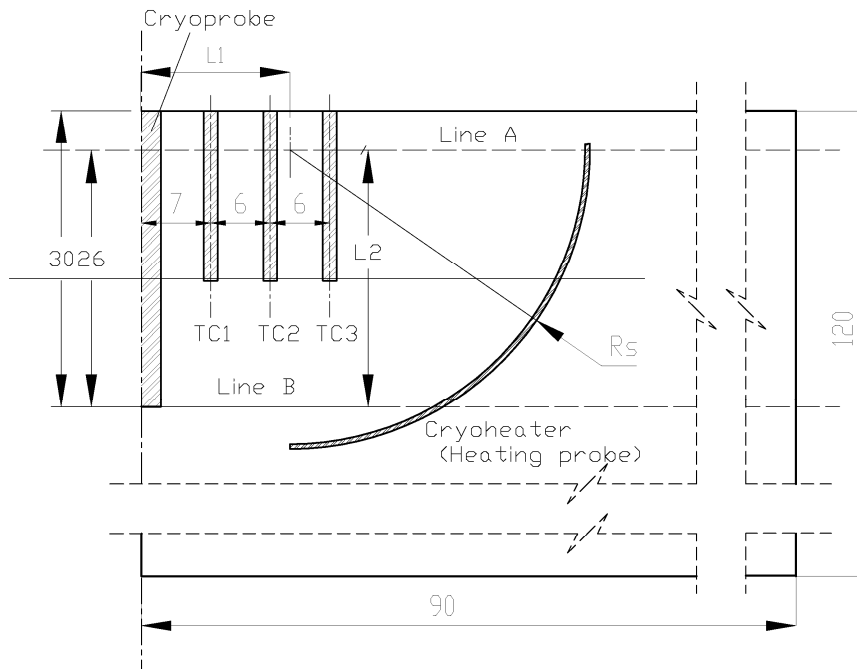
Figure 6.5 A symmetrical layout of the main cryoprobe with retractable cryoheaters and thermocouples. Unit: mm

Figure 6.5 depicts dimensions of the simulation incorporating a hybrid

103

cryoprobe in section 6.2. The diameter of arc representing the deployable cryoheater when fully opened is 60.5 mm. Lines A and line B are located at a depth of 4 mm and 300 mm to track the transient tissue temperature profiles at various depths. The cryoheaters are designed to be carried out in a designated circular arc path R_s.

6.2.3. Comparison of ice front and complete ablation

Previous studies have shown that the incomplete ablation zone generated by a conventional cryoprobe can be significant when compared to the zone of total cell annihilation [28]. Our proposed hybrid cryoprobe, on the other hand, has the capability to regulate ice front and shrinks the size of incomplete ablation. The cryoheaters are carefully set to the heating temperatures around 318 K and minimize detrimental effects of heating.
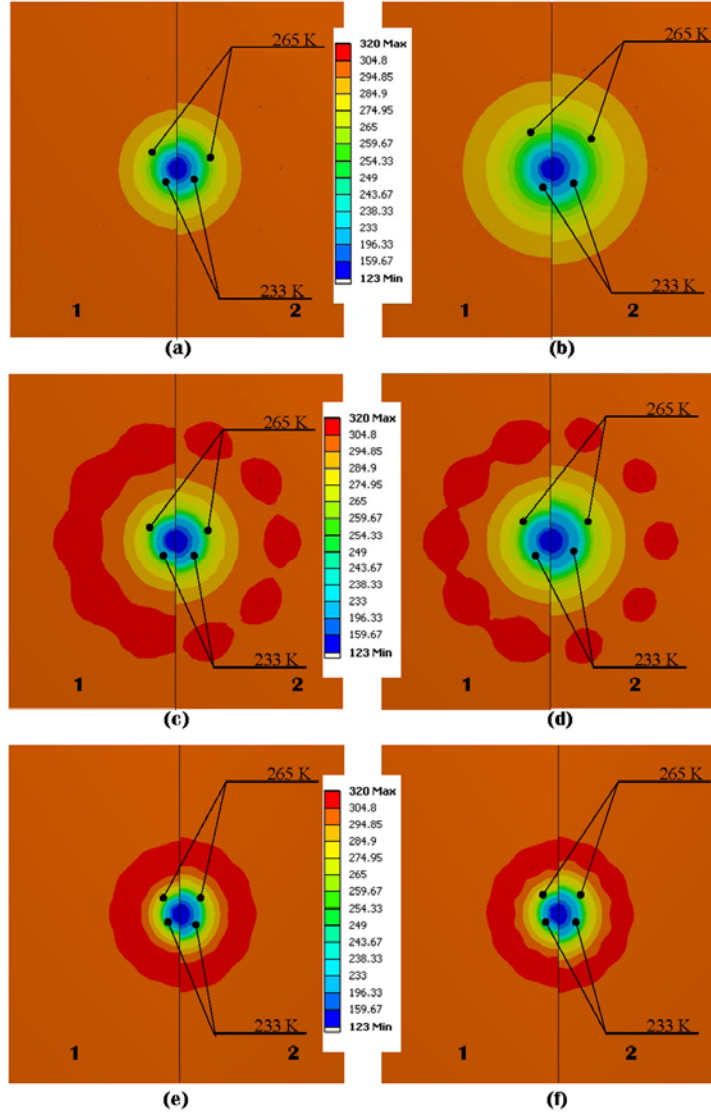
Figure 6.6 Comparison of temperature contours: (a) conventional cryo-freezing at 300 s; (b) conventional cryo-freezing at 720 s; (c) Hybrid cryoprobe A at 300 s; (d) hybrid A at 720 s; (e) hybrid cryoprobe B at 300 s; (f) hybrid cryoprobe B at 720 s. The left-half of graphs (1) is the temperature contour at the plane 15 mm to the end of the cryoprobe and the right half of the graph (2) is the temperature contour at the plane at the tip of the cryoprobe.

To study the temperature development, we have selected two reference planes that are perpendicular to the length of the cryoprobe. Temperature distributions are compared between conventional cryo-freezing and hybrid method. Results are shown in Figure 6.6. Physical parameters of the cryoheater A were $R_s^{(A)}=45$ mm, $L_1^{(A)}=15$ mm, and $L_2^{(A)}=25$ mm while physical dimensions of the cryoheater B were $R_s^{(B)}=25$ mm, $L_1^{(B)}=15$ mm, and $L_2^{(B)}=15$ mm.

Figure 6.6 portrays the temperature contours of three different cases at specific freezing time of 300 s and 720 s. The blood perfusion and metabolism were launched with the values given in Table 5.3. Due to the symmetrical nature of ice front development, only half-section of each temperature contour is shown. The left half (denoted as 1) shows the temperature contours in the reference plane at 15 mm above the cryoprobe tip and the right half (denoted as 2) is the temperature contours of the reference plane just at the tip of cryoprobe.

Based on the results showed in Figure 6.6, it is apparent that freezing conducted with the conventional cryoprobe produces the frozen zone almost doubled its original size as time elapsed from 300 s to 720 s. In contrast, the hybrid cryotherapy in Figure 6.6 (d) and Figure 6.6 (f) demonstrates that the size of 265 K isotherm is reduced with the regulation of cryoheaters.

When examining 233 K isotherm, we observe that the radius of the isotherm for the conventional probe at 720 s is 9.1 mm and isotherms for hybrid system A and B are 9.1 mm and 8.9 mm, respectively. Therefore, it leads us to infer that the hybrid cryoprobe indeed possesses the capability to regulate the growth of incomplete ablation zone while generate marginal impacts on the coverage of the complete ablation zone.

The simulated result has achieved our design rationale that the hybrid cryoprobe can regulate the frozen volume and reduce the size of incomplete ablation. It is worth to discuss the difference between the hybrid cryoprobe and multi-probe therapy. It is apparent that employing one freezing probe with multiple heating probes can also achieve a similar result by regulating the size of incomplete ablation. However, the multi-probe therapy requests more workload for both cryosurgery planning and probe invasions. For example,

implementing 8 heating probes (in the case study) into targeted positions could be problematic. Even with the cryosurgery planning of a proper probe ablation, the cryosurgeon may still need to conduct multiple insertions until probes are properly allocated. The design of hybrid cryoprobe avoids the undesirable invasive procedure. Cryosurgeon only needs to ensure the main probe is allocated in the right manner. This compact design of multi-probe has been widely used in radiofrequency probe. The details can be found in Section 4.2.5.

6.2.4. Response of tissue temperature due to freeze-thaw cycles

We conducted numerical simulations to evaluate the performance of the designed hybrid cryoprobe in freeze-thaw cycles. Each cycle comprises of a freezing process followed by a thawing process as shown in Table 6.1. The freeze-thaw cycles are repeated for three times. The durations of freezing and thawing process within one freeze-thaw cycle were 720 s and 480 s, respectively.

Table 6.1 Freeze-thaw temperature and cycle protocol of the hybrid cryoprobe
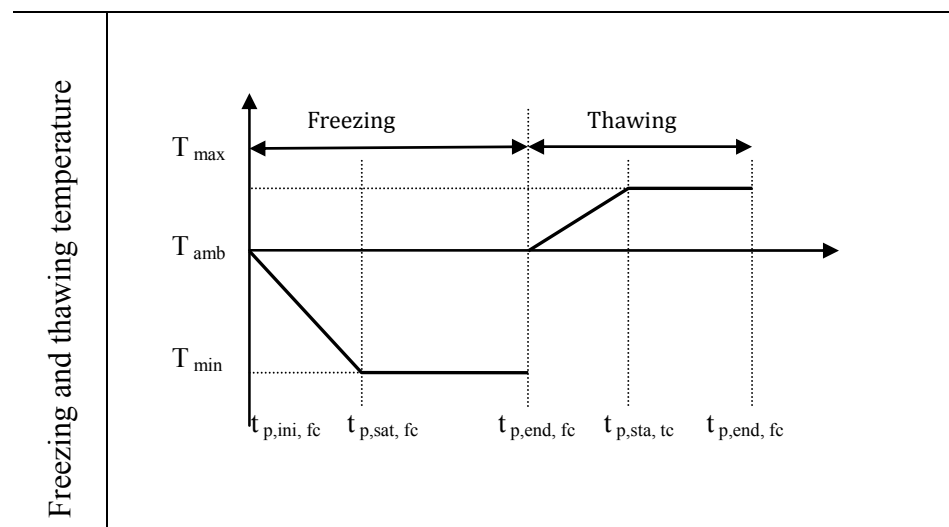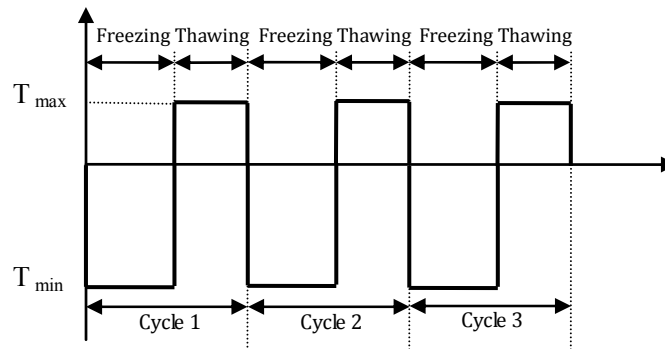
The tissue temperature responses at essential locations are shown in Figure 6.7. We observed that the first cycle generated very limited impact on the TC 5, which was situated 31 mm from the center of cryoprobe. The ablated tissue experienced lower minimum temperatures when the cycles were sequentially repeated.
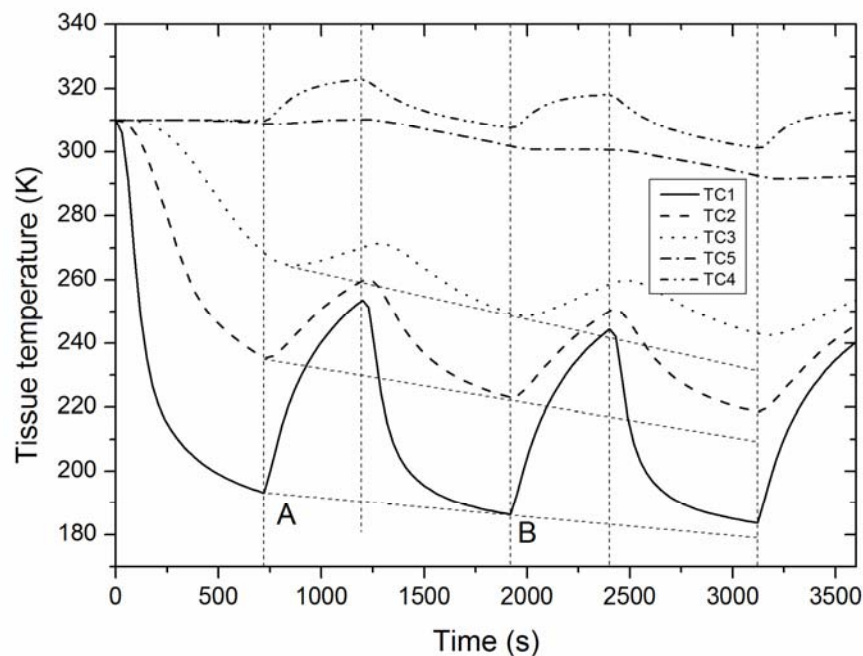
Figure 6.7 Tissue temperatures at essential locations after the commencement of freeze-thaw cycles. Five positions are selectively monitored. Each of the freeze-thaw cycles constitutes 720 s freezing and 480 s thawing. Point A is the minimum

temperature of TC1 in the first freeze-thaw cycle while point B is the minimum temperature of TC1 in the second freeze-thaw cycle.

The highest and lowest obtainable temperatures at monitoring locations of the three cycles were 322 K and 183 K, respectively. When comparing the lowest temperature in the first cycle (point A) with lowest temperatures in the second (point B) and third cycle, we observe a gradual and subtle reduction in the lowest achievable tissue temperature. Similar results are observed at other locations. The observation leads us to conclude that as the freezing cycle proceeds, the minimum temperature lowers further but at a comparatively subtler rate. We name this phenomenon as the "temperature diminishing effect" due to repeated cycles of freezing-thawing. The "temperature diminishing effect" is applicable to freeze-thaw cycles as long as the freezing power is higher than the thawing power. By this token, the same phenomenon is also true of conventional cryosurgery.
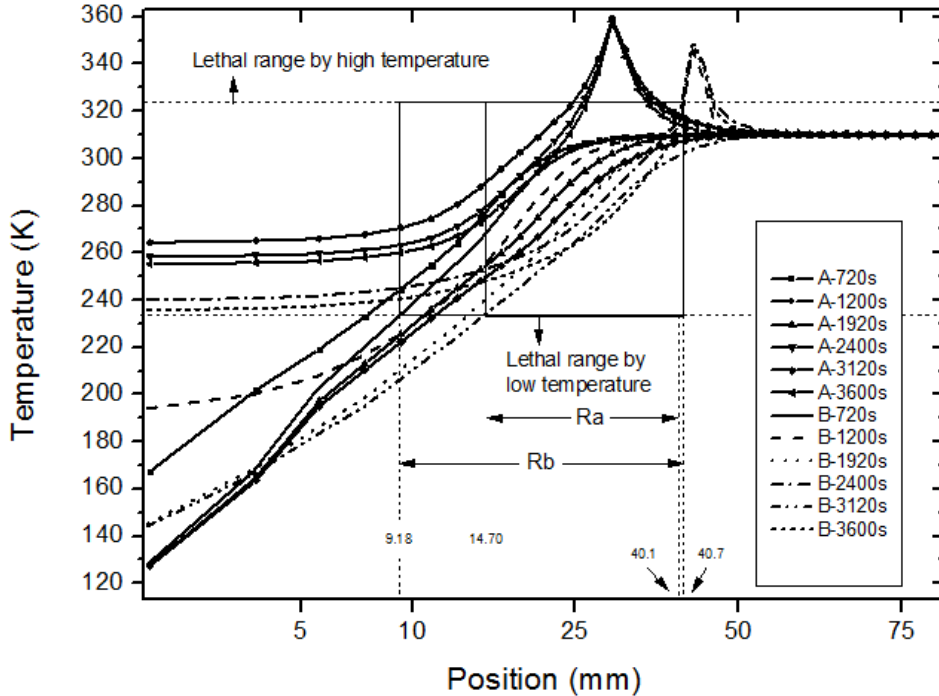
Figure 6.8 Temperature distribution along line A and B. Six time slots with three freeze-thaw cycles are selected.

Figure 6.8 shows the temperature distribution along line A and B. Tissue cells

become more susceptible to survival when their temperature is increased to 315 K, i.e. hyperthermia [160]. Studies have concluded that isotherms of 323 K and 233 K can be chosen as the critical temperatures for heating and freezing [37, 122, 154], which means cells can be assumed to be kill beyond this range. Based on the temperature, we can map and identify an approximate zone of complete ablation. As described earlier, one of the key objectives in this section is to maximize the ablation region within the tumor peripheral boundary while minimize the undesired thermal injury to neighboring region. Two physical indices, R_a and R_b, are employed to measure the size of the incomplete ablation along line A. Figure 6.8 shows that R_a=25.4 mm at 3600 s and R_b=31.52 mm at the 720 s. The similar reduction could also be observed along line B. The size of the incomplete ablation gradually decreases as the cryosurgical procedure proceeds.

6.2.5. Freezing and thawing rates

The freezing rate is a key factor that determines the degree of cell destruction during cryoablation. Cells are destroyed primarily due to the formulation of intracellular frozen tissue. If the cooling rate is higher than 200 K/min, the destruction rate decreases because of vitrification [161]. Upon fast freezing (above 20 K /min), small ice crystals and large surface area of ice-liquid interface are formed. They promote the exposure of protein molecules to the ice-liquid interface and, hence, induce greater damage to the proteins. Recrystallization exerts additional interfacial tension or shear on the entrapped proteins and causes additional damage to the latter [162]. Small ice crystals merge to form large crystals which readily disrupt cellular membranes. Recrystallization may enhance the tissue destruction induced by the preceding freeze cycle [163].
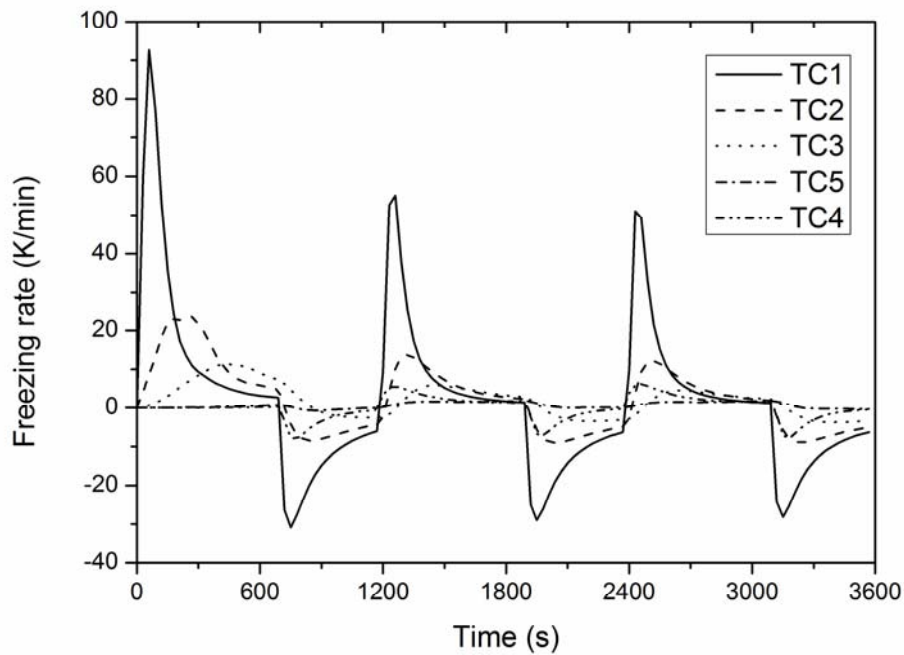
Figure 6.9 Computed freezing rates with respect to time in five locations

The computed freezing rates at different locations are illustrated in Figure 6.9. The positive section of the graph shows freezing rates while the negative section portrays thawing rates. The freezing rates are calculated at intervals of 10 s. Among the five locations, TC1 is found to experience the highest freezing rate and thawing rate. The maximum freezing rate of TC1 in freezing cycles is 92.72 K/min and the maximum thawing rate is 30.92 K/min. Comparatively, the variations of freezing rates are progressively lower at locations further away from the cryoprobe.

6.2.6. Damage rate during freeze-thaw cycles

Figure 6.10 compares the cell damage rate between the simulated result and the reference value [164] within a freezing duration of 720 s. The solid line shows cell damage rate based on in the reference [164]. The dotted line shows the simulated result of the cell damage rate obtained from the proposed freeze-thaw cycle. It is apparent that the simulation plot demonstrates a good

agreement with the reference when the cell damage rate is above 76.9%. Additionally, it can be inferred from Figure 6.10 that the cryoprobe could potentially produce a complete ablation zone with a radial distance up to 10 mm while achieving a 100% cell damage rate due to cryoablation.
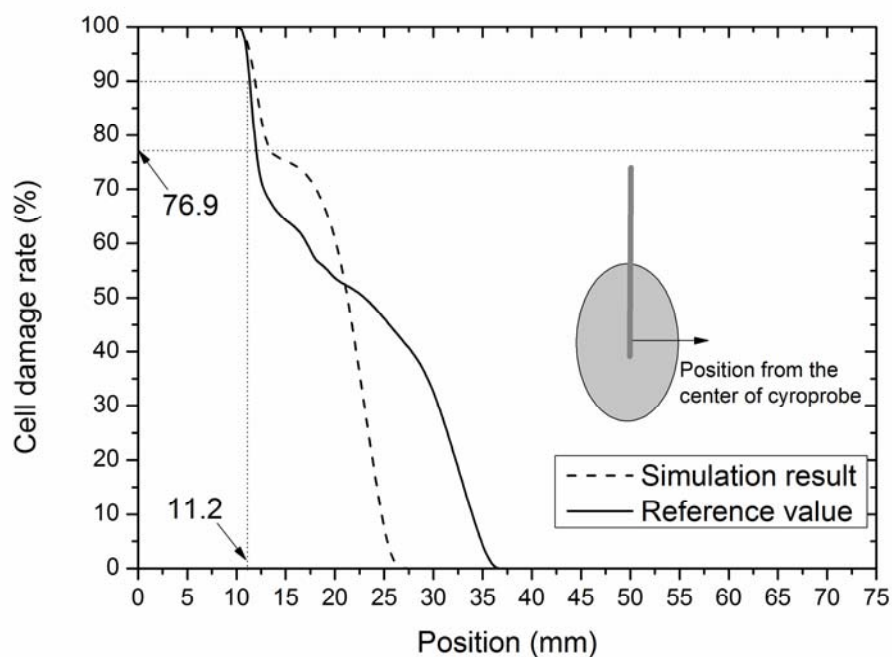
Figure 6.10 Comparison of cell damage rate between the simulation and the reference plots [164]. The x-axis is the radial distance from the center of cryoprobe.

Figure 6.11 illustrates the cell damage rates along the radial direction after the cells have experienced different number of freeze-thaw cycles. It appears from Figure 6.11 that the damage rates are very high in tissue near to the cryoprobe (from 0 mm to 10 mm). Likewise, cells in tissue close to the thawing probe (from 28 to 32 mm) are subjected to high degree of damage. In contrast, cells in the tissue between these two zones, however, experience a lower degree of damage rate. This "in-between" zone is the incomplete ablation that should be reduced. It is fairly indicative from the simulation results that the lowest cell damage rate of the incomplete ablation zone during the first freeze-thaw cycle in this area is only 53 %. Repeating the freeze-thaw process induced greater

112

cell damage in this zone. Degrees of cell damage are elevated to 75%, 90% and 97 % for the second, third and fourth freeze-thaw cycle, respectively.
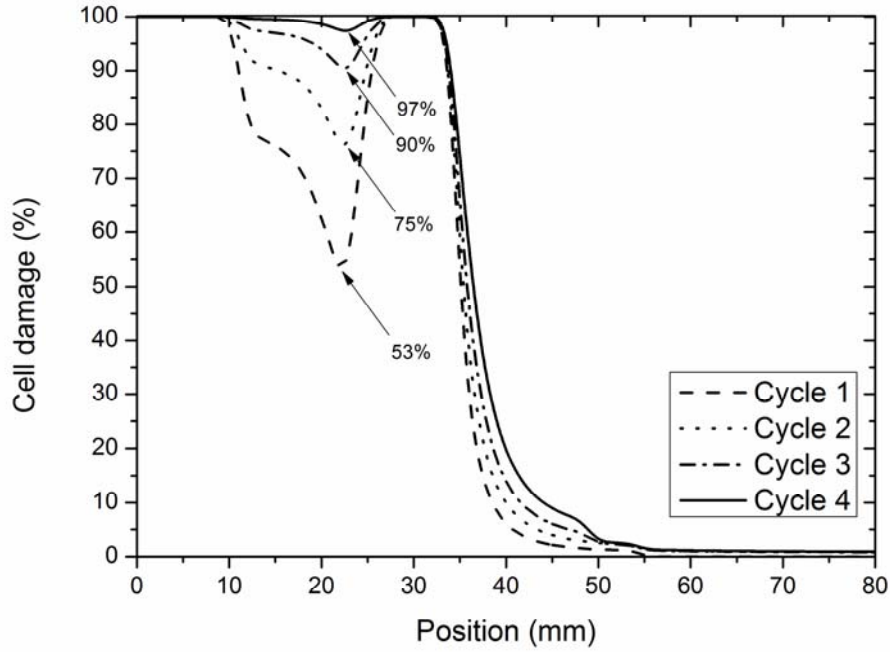
Figure 6.11 Repeating effects of freeze-thaw cycles on the cell damage rate.

With the increase of freeze-thaw cycles, cells within the zone of incomplete ablation began to experience greater cell damage. This observation of enhancing cell ablation with repeated cycles is consistent with the finding that freeze-thaw cycles can promote cryoablation of cells [49, 51]. For the simulations, the following parameters were adopted: $\mathcal{E}_1=10^{31}$, $\mathcal{E}_2=-8.73\times10^{-16}$, $\alpha=1.13\times10^{-1}$, $\beta=1.35\times10^{-3}$, $E_{a,tc}=3.17\times10^{4}$, $R=8.31$, $\tau_1=\tau_2=0.8$, $T_1^{*}=305$ K, $T_2^{*}=310$ K, $T_{tc}^{*}=333$ K, $T_{fc}^{*}=233$ K. To justify the validity of implementing repeated number of freeze-thaw cycles, we can quantify the success of an implemented cryo-protocol based on the regional volume that defines incomplete ablation zone. For example, the implementation of the first freeze-thaw cycle reduced this size of this region approximately from 47% to 25%, a marked reduction of 22%. Further implementation of additional freeze-thaw cycles achieved subtle reduction in the incomplete ablation zone

by approximately 15% and 7% for the second and third freeze-thaw implementation. An almost complete cancer tissue ablation zone could be achieved after the fourth freeze-thaw cycle.

6.3.   Reducing the unwanted frozen zone for surface tumors

We have proposed a simple heating device which could be easily incorporated into the current cryosurgical system for the treatment of surface tumors. Its chief aim is to reduce over-freezing of neighboring healthy tissue. A model to study the thermal process of a biological system is developed. Experiments are also conducted to validate simulated results. Both thermocouple probes and thermographic images are used to acquire essential tissue temperature profiles. A dimensionless parameter, coined as the heating coil coefficient, is defined to evaluate the performance of the boundary heating device. This numerical study establishes an essential framework to select the right size of the heating device to optimally reduce freezing of neighboring healthy tissue.

6.3.1. Performance of heating coil

The experiment setup of Section 6.3 is shown in Section 4.2.4.2. Several experiments were conducted to identify the threshold temperature of heating temperature to regulate the progression of ice front. When the heating coil temperature of heating coil is raised above 373 K, the tissue can be rapidly dehydrated; promoting adhesion between tissue and coil. Therefore, the heating coil temperature has to be judiciously regulated by varying its supplied current. Figure 6.12 illustrates how the coil temperature changes at different current settings. The lines in this figure are employed to calibrate the targeted heating temperature.
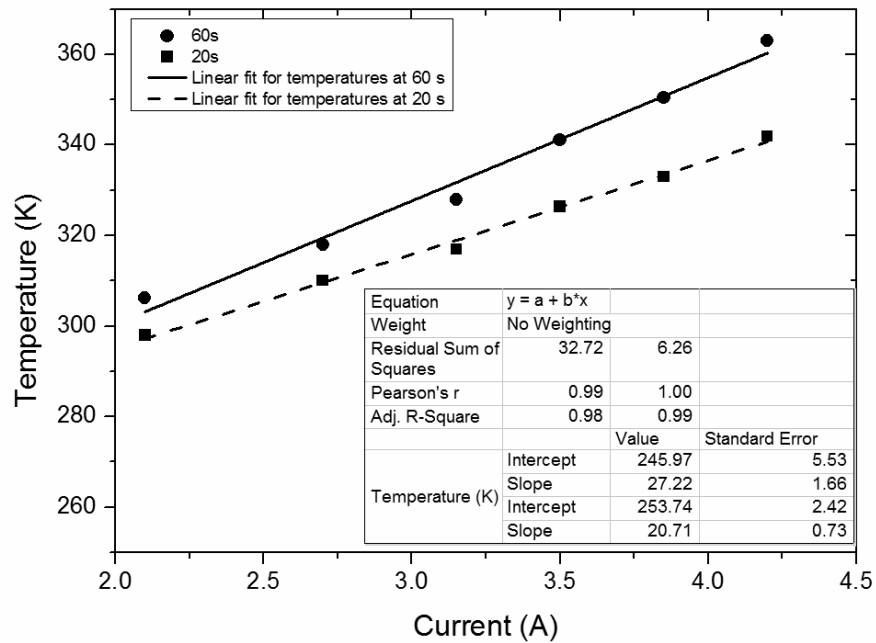
Figure 6.12 Heating coil performance calibrated at different supplied currents.

Figure 6.13 presents nine thermographic images for three different settings. Assuming temperature symmetry within the tissue [20], only a quadrant of each thermal image was chosen at 10 min, 15 min and 30 min. It is apparent that the heating coil exerted a marked influence on the growth of the 265K isotherm. For example, without the use of the heating coil, the diameter of the 265K isotherm was 70 mm at 30 min as shown in Figure 6.13 (c). When a heating coil with a diameter of 50 mm was applied, the size of the 265K isotherm shrunk to a diameter of less than 50 mm as depicted in Figure 6.13 (f).
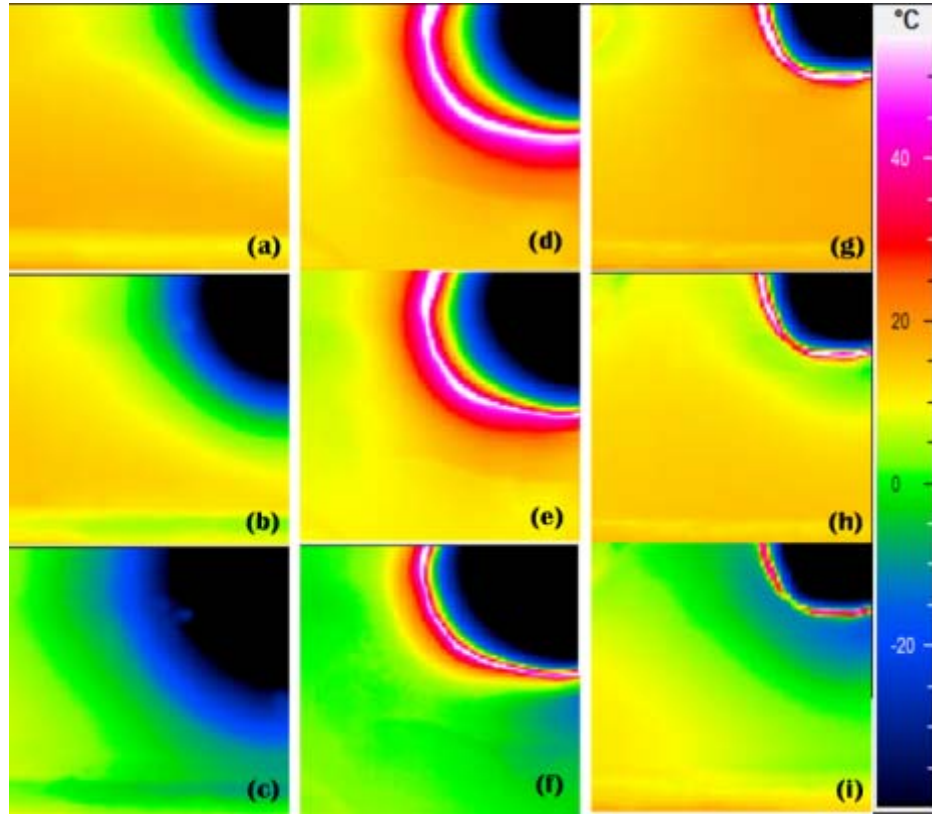
Figure 6.13 Thermographic images: (a) 10 min without heating coil; (b) 15 min without heating coil; (c) 30 min without heating coil; (d)10 mins with a heating coil of 50 mm diameter; (e) 15 min with a heating coil of 50 mm diameter; (f) 30 min with a heating coil of 50 mm diameter; (g) 10 mins with a heating coil of 35 mm diameter; (h) 15 min with a heating coil of 35 mm diameter; and (i) 30 min with a heating coil of 35 mm diameter.

6.3.2. Comparison between the experimental and simulated results

A grid independence test has been conducted to select an appropriate mesh size for simulations. Under *in vitro* experimental condition, both metabolism and blood perfusion terms are momentarily regulated to zero. To model clinical surgical conditions, the phenomena of metabolism and blood perfusion are reactivated in subsequent simulaitons. Tissue and blood properties applied to the model are listed in Table 5.3. In this present model development, the metabolism heat and the heat source of blood are considered to be relatively constant. This assumption is consistent with existing published works [98, 118, 165].

The thermal simulation algorithm was based on solving the transient energy equations using finite element method. The scheme used to solve the equation is based on a finite difference formulation. As the finite element method is widely used, the finite difference formulation is not included in this work. Interested readers can refer the references [35, 166] for details. The simulated data used in Eq. (5.1) was obtained by transit thermal module in Ansys 12.1. A grid independence test was carried out to choose a proper mesh size. Three meshes divisions of 39769 cells, 10240 cells, and 5923 cells are generated to study the impact of grid-size on model accuracy. Results shows that the variations for the finest mesh division, finer mesh division and the coarsest mesh division were 5.6 %, 6.3%, 14.6%, respectively. The mean relative deviation modulus of below 10 % typically indicates a good fit for practical purposes [167]. Considering the length of the computational time, the mesh comprising 10240 cells was selected and applied to all simulations.
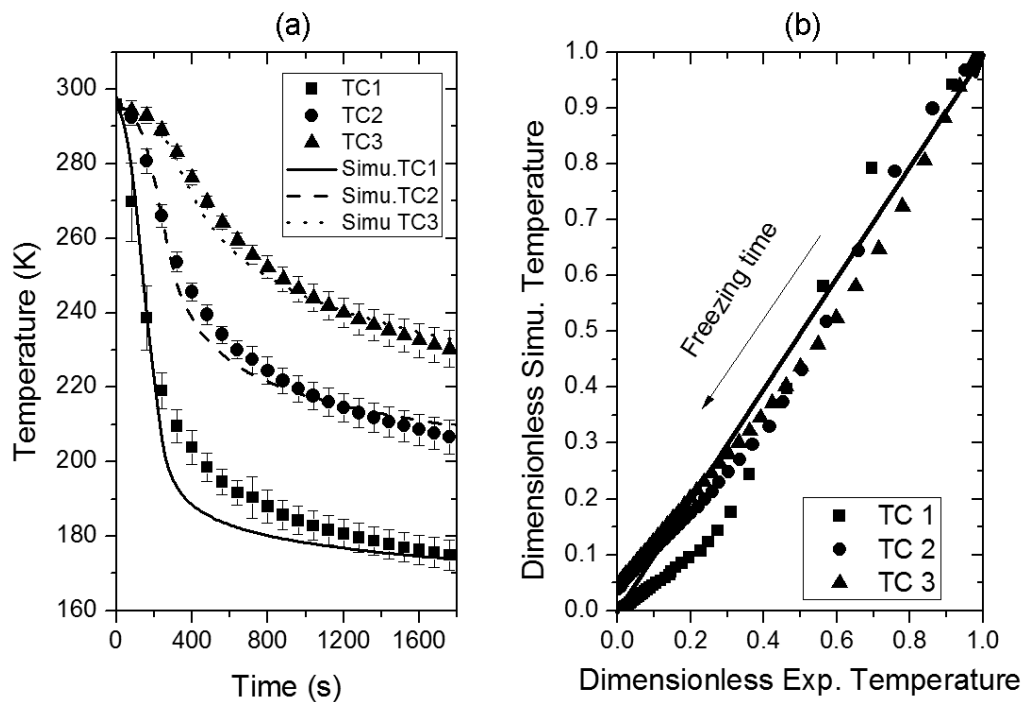
Figure 6.14 Comparing experimental results and simulation by the temperatures at three locations when the current supply was at 4.2 A. (a) absolute temperature

progression over time; (b) comparison of dimensionless temperatures.

Figure 6.14 shows the validity of the model by comparing the temperature parameters between experimental data and simulation results. Figure 6.14 (a) compares the absolute temperatures of the experimental and simulated data over time. Compared to the temperatures obtained by the thermocouples, the largest error in the simulation is observed to be 6.3% Experiments are repeated four times and the variability is shown with error bars. Comparing data variance, dimensionless simulated temperatures versus dimensionless experimental temperatures are plotted in Figure 6.14 (b). Dimensionless temperatures are computed by dividing the local temperature difference at t with the largest temperature difference within t_0. Simulated dimensionless temperatures are calculated from absolute simulated temperatures while the experimental dimensionless temperatures are computed from experimental data. The local temperature difference at time t is obtained from the difference between the transient local temperature T (t,X) and the minimum local temperature $T_{min}(t_0,X)$. Therefore, the dimensionless temperature parameter under a predetermined operating condition can be derived from the equation: $(T(t,X)-T_{min}(t_0,X))/ (T_{max}(t_0,X)-T_{min}(t_0,X))$. This normalized parameter spans 0 to 1 and it facilitates the intuitive comparison of varying dimensionless temperature parameters.
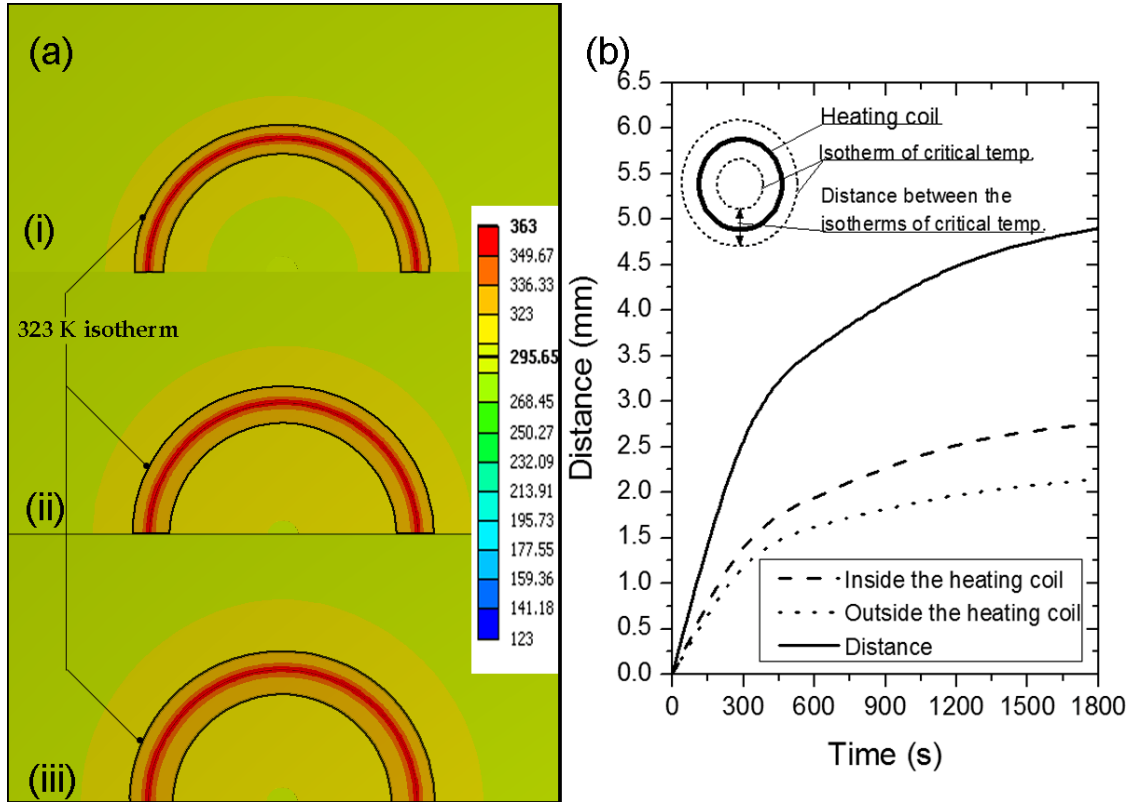
Figure 6.15. (a) Heating coil temperature development without the activation of the cryo-freezing at (i) 600 s, (ii) 1200 s and (ii) 1800 s; and (b) Lethal temperature boundary formed by the heating coil. The lethal temperature isotherm of 328K was identified inside and outside of the heating coil from the center of the cryoprobe. The overall lethal temperature isotherm distance was illustrated by a solid line.

To avoid the thermal interference due to cryo-freezing, the tissue's temperature distribution was studied only with the activation of the heating coil. Figure 6.15 shows the development of 328 K isotherms [168]. Taking reference from the heating coil's perimeter, the internal isotherm contracted while the external isotherm expanded. A slower growth rate of the radial distance between these two isotherms was detected due to the subtle degradation of the coil's heating power. The activation of heating coil for a period of 10 min produced a 3.5 mm gap between the two isotherms. The maximum radial distance between the two critical temperature isotherms was observed to be 4.9 mm.

6.3.3. Ice front development and critical temperature isotherms
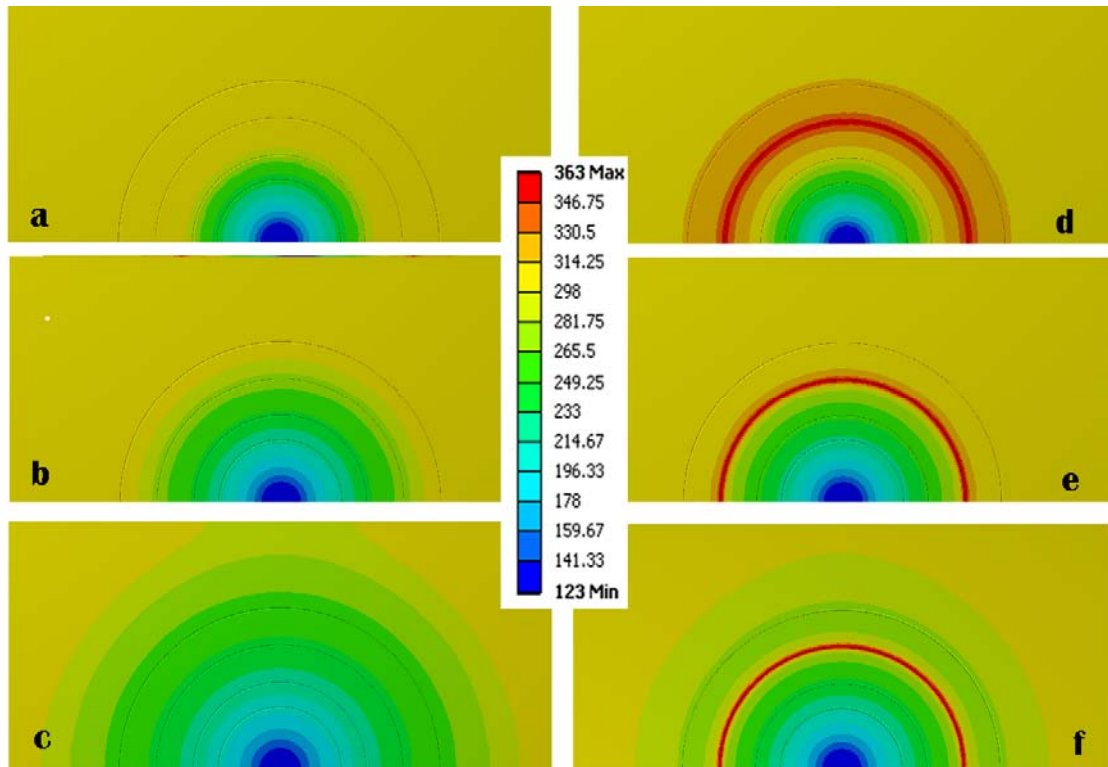
Figure 6.16 Comparison of temperature development in the simulation: (a) no heating coil at 200 s; (b) no heating coil at 600 s; (c) no heating coil at 1800 s; (d) 50 mm heating coil at 200 s; (e) 50 mm heating coil at 600 s; (f) 50 mm heating coil at 1800 s.

Figure 6.16 compares the simulated temperature contours with and without the heating coil. Apparently, the installation of the circular heating coil retarded the progression of the 265K and 233K isotherms. Regulating the heating power of the coil would allow surgeons to control the development of the ice front and tune the cryo-lesion region.
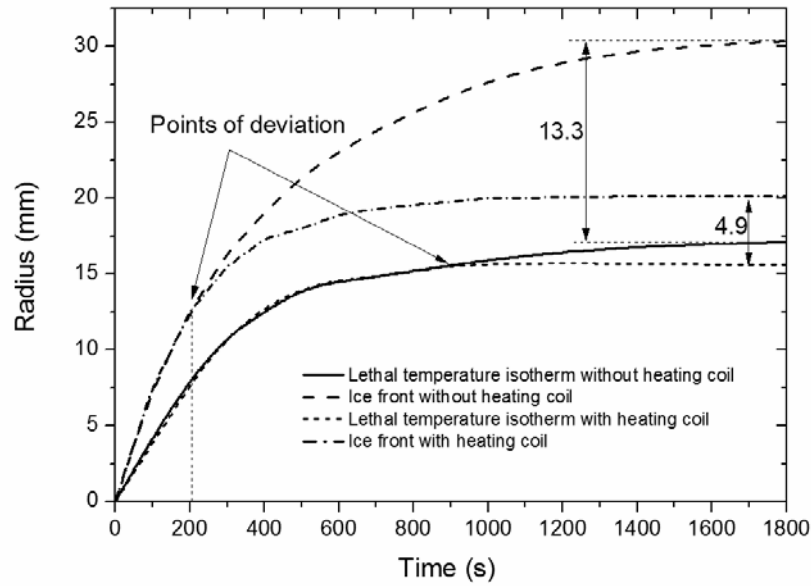
Figure 6.17 Development of the ice front and 233 K isotherm in radial direction with and without the adoption of 50 mm heating coil.

Figure 6.17 shows the development of the 265 K and 233 K isotherms in the radial direction with and without installing the heating coil. In a conventional system where no boundary heating was adopted, the 265 K isotherm achieved a radial distance of 30.5 mm while the 233 K isotherm progressed radically to 17.2 mm. It was observed that by simply adopting a heating coil of 50 mm diameter, the radius of 265 K and 233 K isotherms could be regulated to 20.1 mm and 15.2 mm, respectively. Figure 6.17 further illustrates that the point of deviation between the ice two isotherms (with and without heating coil) occurred at 205 s while the point of deviation of the 233 K isotherm occurred at 900 s. In other words, the boundary heating coil possessed the capability to contain the movement of the 265 K ice front without interfering without the 233 K isotherm progression in the first 900 s, Comparing the relative distance between 265 K and 233 K isotherms, we observed a marked reduction from 13.3 mm to 4.9 mm. The reduction is largely attributed to the external heat provision by the heating coil that significantly diminished the growth of the 265K isotherm.

6.3.4. Selection of appropriate heating device

Once the physical morphology of a tumor is detected, the size of heating coil and the operating condition are required to be determined. The size of the heating coil and its operating condition are correlated. The ice front (265 K isotherm) can surpass a small heating coil within a short freezing duration. On the other hand, incorporating a large heating coil may generate minimal thermal impacts on reshaping the frozen tissue. To evaluate the performance of heating coil, we introduce a dimensionless parameter coined as "heating coil coefficient". It refers to the ratio of the frozen area with the heating coil to the frozen area without the heating coil. The coefficient quantifies the thermal impact of heating coil compared to the conventional cryo-freezing process. A small value of heating coil coefficient demonstrates greater therapeutic efficacy of the heating coil in protecting large peripheral tissue from freezing.
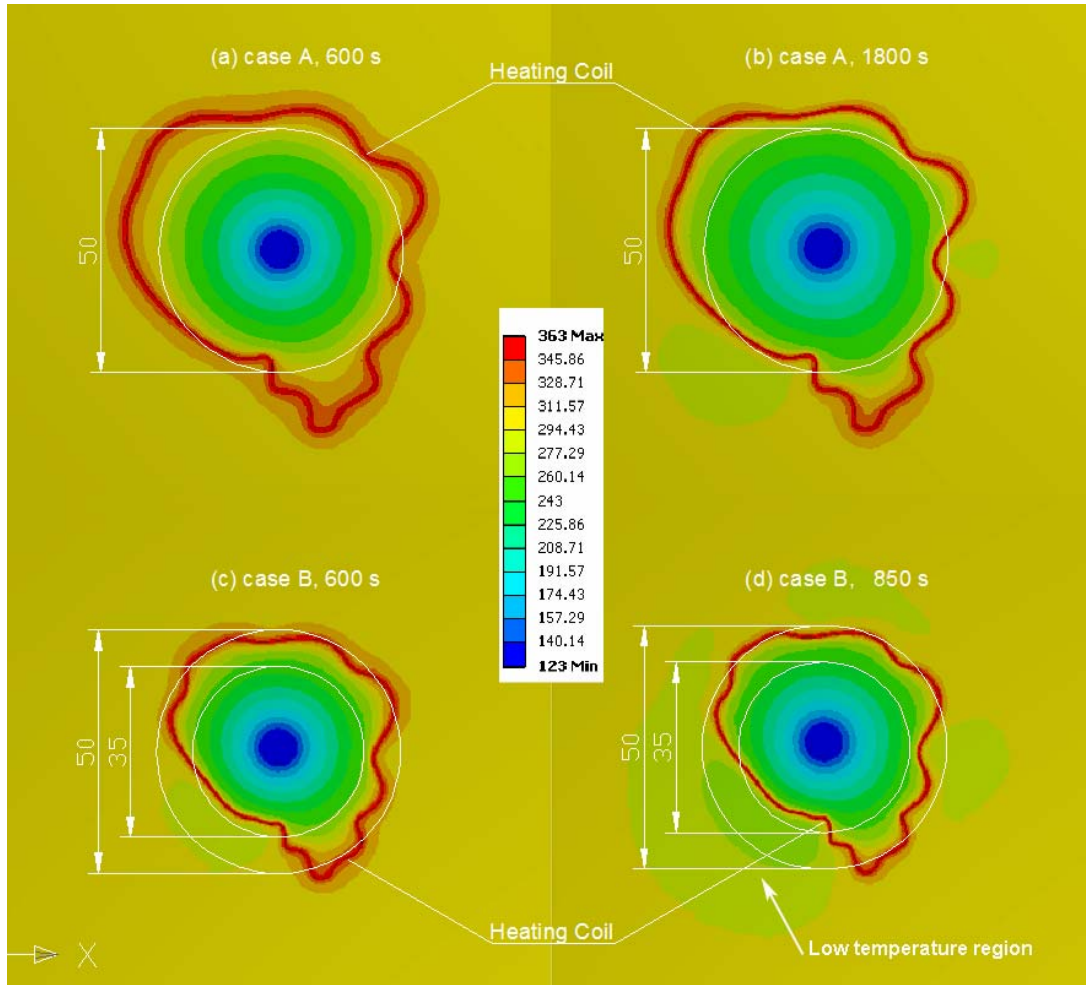
Figure 6.18 Temperature contours of the tissue with customized heating coils. (a) case A at 600 s; (b) case A at 1800 s; (c) case B at 600 s; (d) case B at 1250 s.

To enhance the performance, the customized configuration of heating coil becomes necessary, especially when tumors are associated with different sizes and formations. As the Nikrothal wire is thin (0.4 mm), the shape of the heating coil allows to be adjusted manually. The physician can reshape the outline of the heating coil according to cryosurgical needs. We demonstrated the versatility of using malleable heating coils based on the tumor's profile. The profile of a liver tumor was adopted from a reference [169]. Figure 6.18 shows temperature distributions of the tissue with two customized heating coils. Both cases (A and B) were installed with the same operating condition but the size of the heating coil in case A was comparatively larger than that in case B. Two reference circles of 50 mm and 35 mm are plotted in Figure 6.18

to demonstrate the sizes of the heating coils. Figure 6.18 shows the temperature profile of case A at 600 s. Figure 6.18 (b) shows that the ice front is still constrained within the heating coil at 1800 s. Figure 6.18 (c) shows the temperature profile of case B at 600 s while Figure 6.18 (d) shows the temperature profile of case B at 850 s. It is apparent that further cryo-freezing would induce the frozen zone forming in the region outside the heating coil.
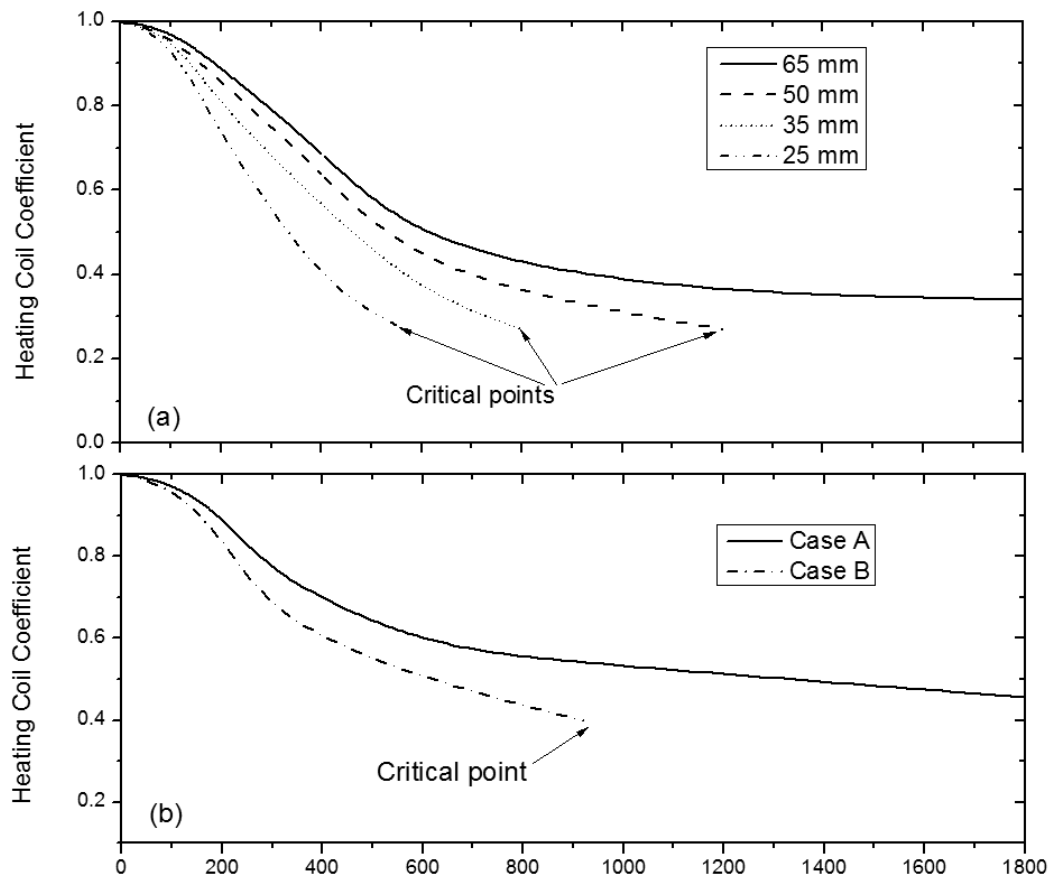
Figure 6.19 Variation of heating coil coefficient as time proceeds. (a). heating coil coefficients of the circular heating coils; (b) heating coil coefficient of the customized heating coils based on the profile of tumor.

The heating coil coefficient is a useful indicator to evaluate the degree of the peripheral tissue protection arising from the employment of an appropriate boundary heating device. Figure 6.19 (a) shows the variation of the heating coil coefficients for four circular heating coils. The starting value of the

heating coil coefficient was 1 for all coils, indicating that the impact on minimizing freezing in the undesired area with and without adopting heating coils was equal. The heating coil coefficient continued to drop thereafter till the end. When the ice front exceeds the heating coil perimeter, the heating coil becomes ineffective in containing the frozen tissue. We employ a critical point to identify the effective operating duration when the ice front surpasses the edge of the heating coil. Results have indicated that the critical points of heating coils with diameters of 25 mm, 35 mm and 50 mm occurred at 520 s, 800 s and 1200 s, respectively. Beside the circular heating coil, the critical point for customized heating coil was also investigated. Figure 6.19 (b) illustrates the developments of heating coil coefficients for customized heating coils.

6.3.5. Discussion of the heating coil cryotherapy

The effectiveness of incorporating the heating coil in cryosurgery depends on several key factors. First, the primary concern associated with this proposed peripheral heating assisted cryo-therapy is the size of the selected coil and the operating condition. For instance, our results have shown that a heating coil of 35 mm diameter is ineffective in containing the growth of the 265K isotherm as the ice front exceeds the boundary of the heating coil after 15 min. In contrast, a heating coil of 50 mm diameter with the same freezing duration is effective in containing the growth of the 265K isotherm. Investigations have demonstrated that smaller heating coils translate to lower heating coil coefficients for the same time frame. For example, results have shown that the heating coil coefficient for a 65 mm diameter is 0.47 while a 35 mm diameter one realizes a coefficient of 0.37 at 600 s. From the illustration depicted in Figure 6.19 (a), the heating coil coefficient was obtained to be 0.44 at 600 s by incorporating a circular heating coil of 50 mm diameter. This translates to a

potential saving of 56% reduction in undesired freezing of the neighboring tissue compared to an existing cryo-system without the use of a boundary heater. No critical point was detected for a heating coil with 65 mm diameter within 1800 s. The ice front is well contained within the coil boundary. We infer from these observations that a larger diameter heating coil has a longer valid operating duration. In contrast, a relatively smaller one is capable of minimizing the undesirable over-freezing of neighboring tissue.

It is noteworthy that the size of the heating coil depends on the heating coil's configuration. This work further investigates the shape of non-circular heating coil and its impact on shaping the frozen tissue. Specifically, a customized heating coil has proven to be effective in shaping the ice front. Compared to the circular heating coil, the customized heating coil adheres to the same heat transfer principle in that a large heating coil has a longer valid operating duration and is less capable of minimizing the unwanted frozen zone. Figure 6.19 (b) shows that the critical point of case B is at 850 s which is similar to the critical value of the circular 35mm diameter heating coil. Examining case B in Figure 5.21, the shortest distance from the heating coil to the cryoprobe is less than 35 mm. Within this region, the tissue temperature out of the heating coil boundary is lower than the tissue temperature from the cryoprobe to the coil periphery. When the freezing duration is sufficiently long, the frozen zone can start to grow in this external coil region. The critical point of the customized heating coil is determined chiefly by the portion close to the cryoprobe.

Temperature control of the heating coil influences the degree of tissue damage. A small elevated body temperature (hyperthermia) can induce severe disability or even death by prolonged exposure [168]. Studies have shown that temperatures as low as 318K can inflict an irreversible tissue damage over an

126

extended period of time whereas 373K can kill tissue in fractions of seconds [168]. Generally, the tissue destruction requires only milliseconds at 373K, 1-2 s at 328K, 15-20 s at 323K and well over 15 min at 318K [168]. Previous studies have illustrated that the 233K isotherm can achieve a distance over of 15 mm in the radial direction without blood vessels [170, 171]. Compared to cryo-freezing, the thermal damage induced by the heating coil is comparatively small. Figure 6.15 shows that the distance of thermal damage is only about 4.5 mm at 1200 s. This may be attributed to thermal conductivities of tissue under frozen and unfrozen states. The thermal conductivity of the unfrozen tissue is about four times less than that of frozen tissue [149]. In addition, the temperature drop of the cryoprobe is typically several times higher than the temperature increase of the heating coil as described earlier in Section 6.3.1.

Coupling cooling with heating during cryosurgery has been studied in several works [35, 44, 117, 172]. The cryoheater acts as a complementary device to the cryoprobe as a means of shaping the cryo-ablative zone. Compared with the proposed heating coil, one key drawback of the cryoheater is the large number of cryoheaters required to achieve optimal cryosurgery control of complex tumor geometries [117]. To reduce the complexity of cryo-planning, Yan et. al. proposed a treatment modality combining cryosurgery and hyperthermia treatment [44]. This method labeled as one time's percutaneous insertion while multiple times' freezing/heating ablation is flexible in administrating cryo-freezing of non-spherical tumors [44]. Apparently, this treatment approach seems to be effective for treating slender or elongated tumors. Compared to these studies, our results have indicated the heating coil approach to be markedly effective in controlling the profile of the frozen zone. In addition, this approach is less invasive and is capable of generating uniform heating throughout the tumor's periphery.

Chapter 7: An Analytical Study on RF-assisted Cryosurgery

Radio frequency (RF) ablation and cryosurgical ablation are both minimally invasive tools that have been widely used in clinical procedures to destroy aberrant tissues. However, there are very few studies focusing on the evaluation of a hybrid method of combining these two technologies. Therefore, we have built an axisymmetric three-dimensional finite element model that evaluates the performance of RF-assisted cryosurgery. In the first stage of this work, the RF ablation and cryosurgical ablation are studied separately. This helps to validate simulated results with their respective experimental data. The second stage contains a proposed RF-assisted cryo-device. The electrode and the ground pad in a conventional RF ablation system are incorporated within a cryoprobe. This RF-assisted cryosurgery is capable of producing heating while freezing. The goal of this study is to produce complete ablation while limiting the collateral damage to adjacent healthy tissue.

7.1. Test of a single RF probe
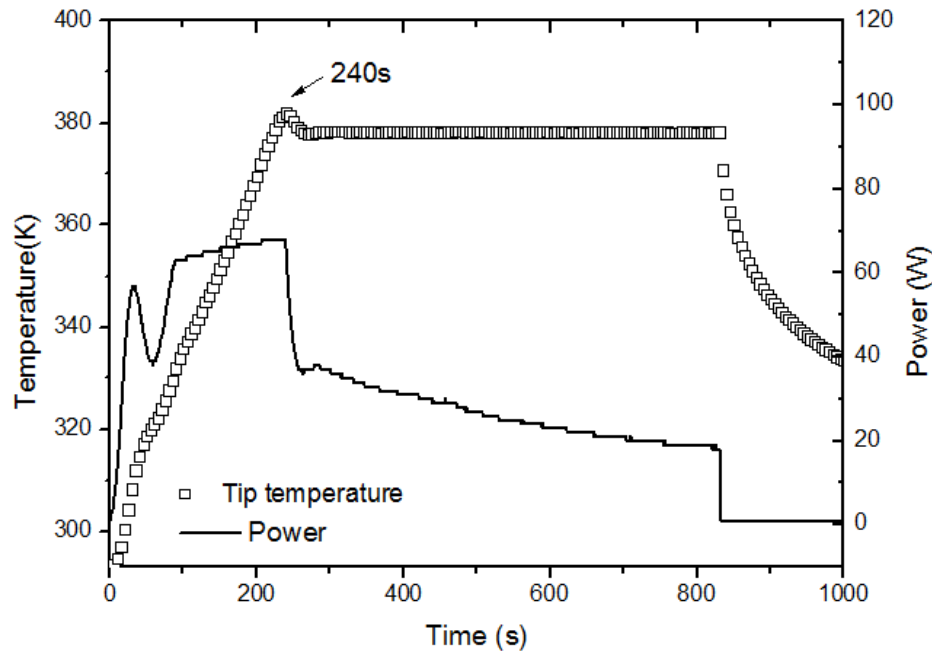
Figure 7.1 Development of the electrode temperature and the RF power under ATC mode.

Figure 7.1 shows the development of electrode temperature and RF power under ATC mode within an ablative duration of 820 s. The power increased at the initial stage of ablation until the electrode temperature was above 380 K. The maximum RF power was observed to be 68 W. ATC mode subsequently reduced supplying power to 38 W within a few seconds. Thereafter, the power of RF generator slowly dropped to 20 W at 820 s. The benefit of ATC mode compared to the constant power mode is that the system employs large RF power at the initial stage of ablation. The large power accelerates the electrode to reach the predetermined temperature and reduces the overall duration of treatment. Meanwhile, the tissue nearby electrodes can be protected from charring since the ATC mode reduces the supply power when the ceiling temperature is met.
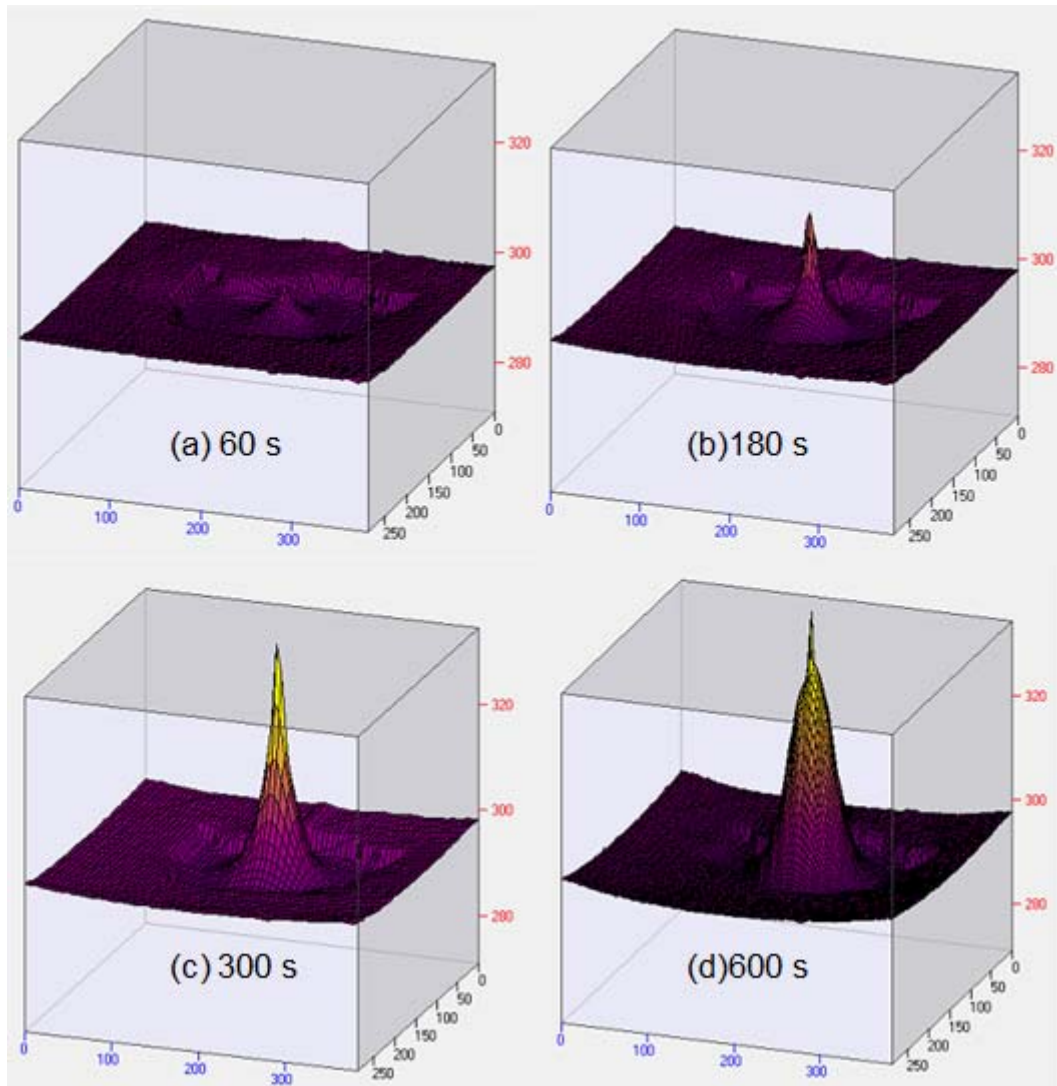
Figure 7.2 Three-dimensional view of the temperature development, at 60 s, 180 s, 300 s and 600 s.

Figure 7.2 shows the development of surface temperature during RF ablation. When the single RF electrode was activated, the temperature of tissue around the electrode was raised up and the heat propagated to the surrounding tissue. Figure 7.2 displays the tissue temperature at 60 s, 180 s, 300 s and 600 s. The highest temperature within the first 600 s was 340 K as shown in Figure 7.2 (d). Compared to highest electrode temperature in Figure 7.1, the highest temperature at the surface was low. The difference was because that the active ablating potion of RF electrode was located within the surface of porcine liver. The temperature contours of single RF probe obtained within 1200 s are

shown in Figure 7.3.
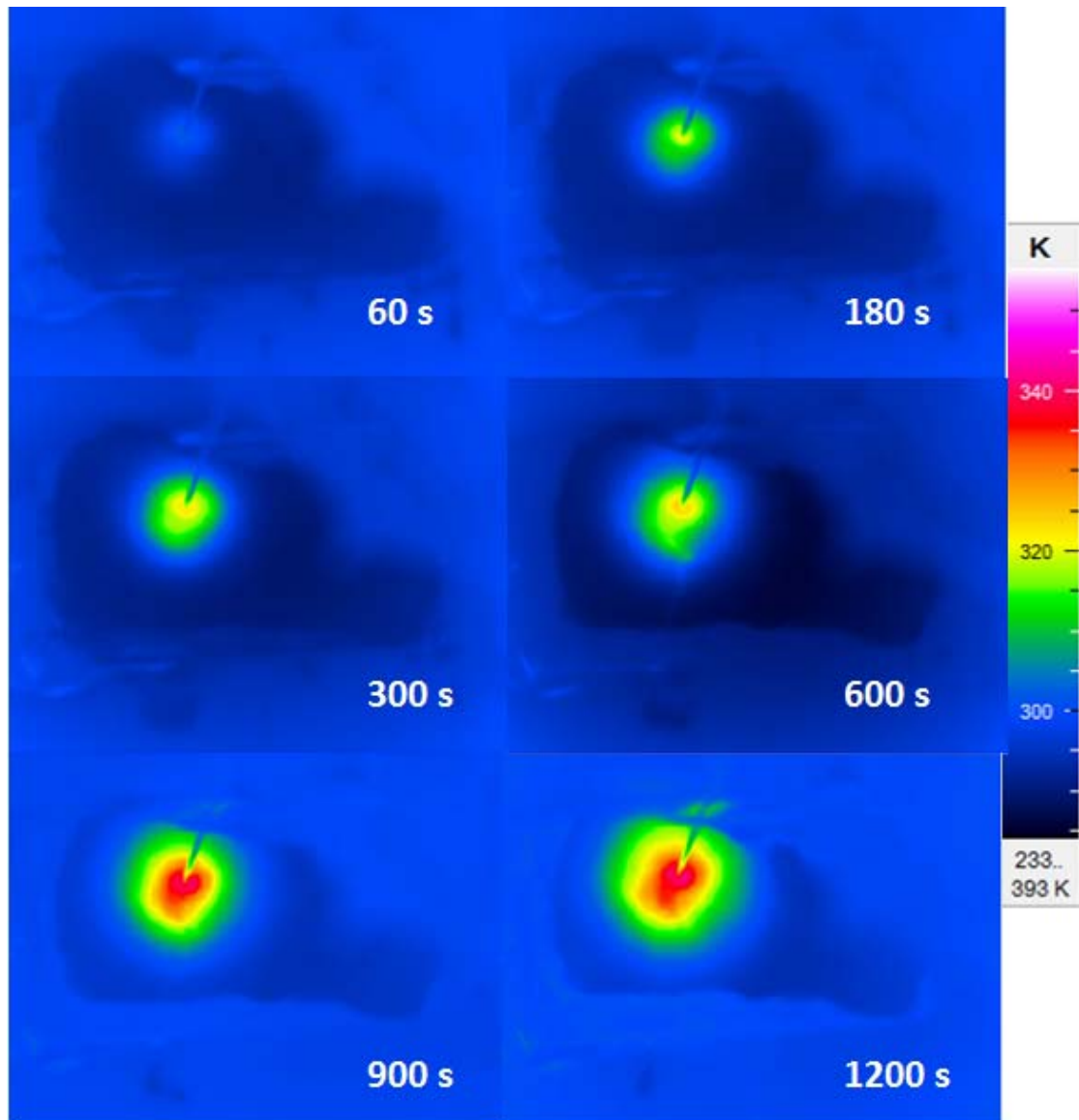
Figure 7.3 Temperature contours of a single RF probe at 60 s, 180 s, 300 s, 600 s, 900 s and 1200 s.

RF probes that we used during experiments were non-internally cooled electrode. As illustrated in literature review, the internally cooled electrode is commonly used to enlarge the ablation zone by circulating chilled saline solution in two coaxial lumens situated within the electrode [173]. It avoids carbonization around the electrode and subsequently maintains low impedances during the ablation [174]. Table 7.1 compares the performance of the internally cooled electrode and non-internally cooled electrode.

131

Figure 7.4 Size of complete ablation.

Table 7.1 Performance of internally cooled and non-internally cooled RF electrode

Technical parameters	Single RF electrode			
Type	Internally cooled [139]		Non-internally cooled	
Ablation time (s)	600	600	600	800
Average power (W)	30	40	41.3	32.74
Initial temperature (K)	-	-	293±2.5	293±2.5
Needle diameter (mm)	1.8	1.8	2	2
DS (mm)	20±1.4	22±1.6	17±1.8	21±2.5
Highest temperature (K)	341.3±4.55	353.7±8.45	382.1±3.2	380.5±3.2

Note: table displays the technical parameters, lesion diameter and temperature data. Some data are mean values ± standard deviation. DS: short-axis diameter of the ablative area.

Table 7.1 shows the key results for internally cooled and non-internally cooled RF electrode. ATC mode was employed in the comparison. Experimental results showed that within the same targeted duration of 600 s, the internally cooled RF ablation produced 22±1.6 mm at 40 W while non-internally cooled RF ablation produced 17±1.8 mm at 41.3 W. The highest temperatures were 353.7±8.45 K and 382.1±3.2 K for internally and non-internally cooled RF

ablation, respectively. The internally cooled RF electrode employed distilled water circulating within the probe so that the tissue in high temperatures, which is close to the RF electrode, can be largely reduced. The sizes of lesions for the above two tests were 22±1.6 mm and 17±1.8 mm, respectively. Therefore, compared to the non-internally cooled probe, the internally cooled probe were associated with low maximum temperature and large ablation lesion. Table 7.1 also indicates that by the same probe, the extended ablative duration or a large input power can enhance the volume of complete ablation.

7.2. Test of a multi-tine RF probe

In this section, a nine-tine RF probe was tested within *in-vitro* livers. The coverage of deployed electrodes, controlled by marked Labels of the development shaft, is shown in Figure 4.13. *Label* 2, *Label* 3 and *Label* 4 refer to the maximum coverage diameter of nine-array electrodes are 20 mm, 30 mm and 40 mm, respectively. The size of nine-tine RF probe subjected to *Labels* are shown in Figure 7.5.
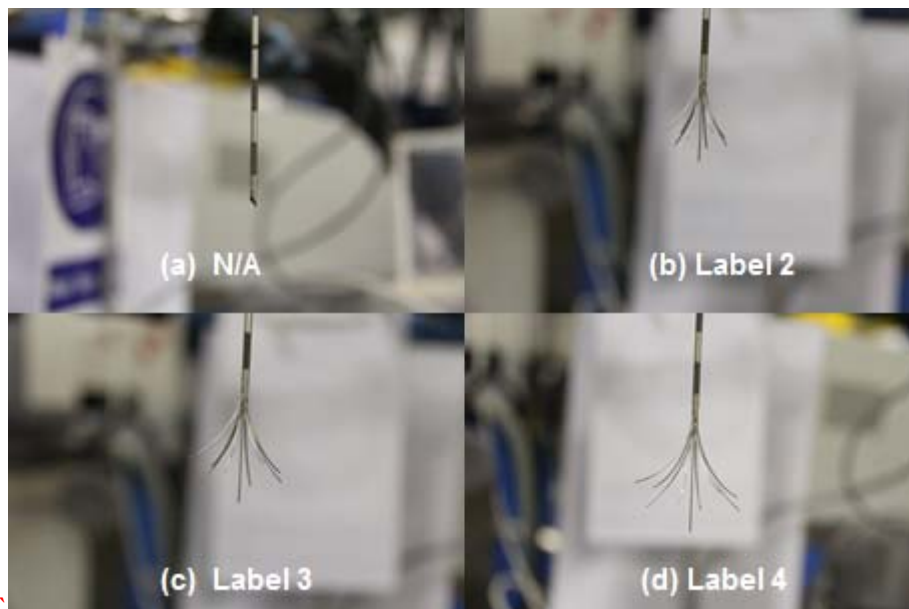
Figure 7.5 the display of nine-tine RF probe with three labels shown in the development shaft.

During experiments, the ground pad was placed under the liver samples

around 150 mm from the tip of RF probe. The RF probe was deployed to *Label* 4 before the activation of ATC mode. Figure 7.6 shows the temperature contours of a nine-tine RF ablation with the ground pad marked.
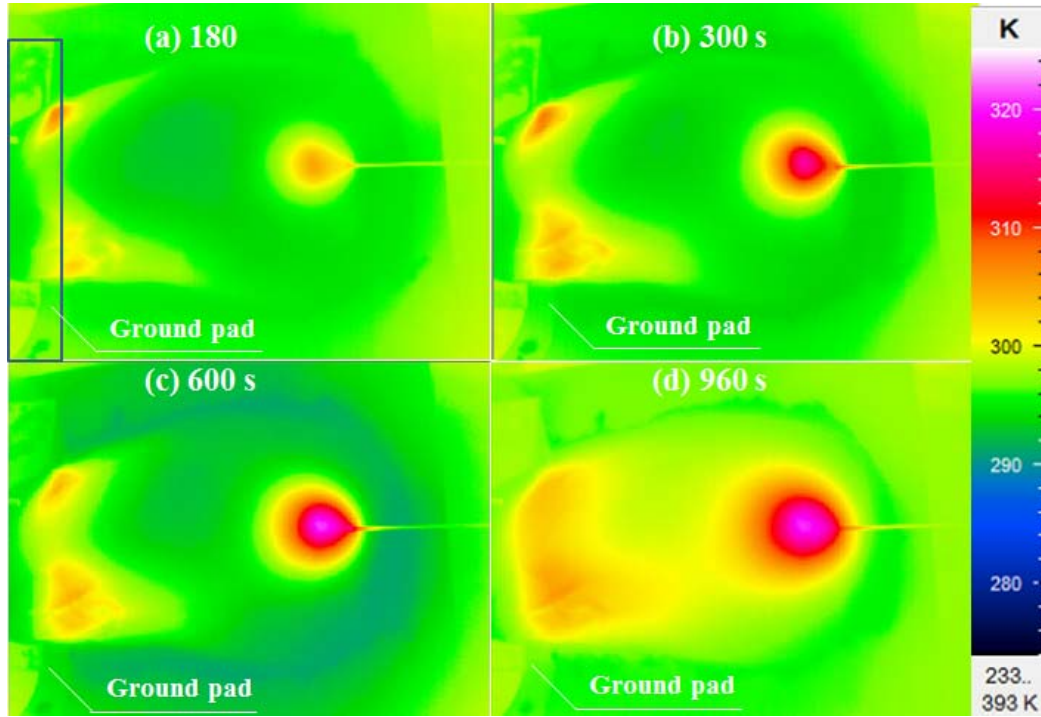
Figure 7.6 Temperature contours of a liver with a nine-tine RF probe at (a)180 s; (b)300 s; (c)600 s; and (d)960 s. The ground pad is marked on the graphs.

Figure 7.6 displays the temperature contours at four ablation durations. The tissue near the ground pad and the RF electrode was associated with high temperatures. On the ground pad side, the surface temperatures in the top left and left bottom were higher than the temperature in the middle. This can be attributed to the variation of the thickness of the liver. The middle portion of the liver tissue was a bit thicker than the tissue on the top left and left bottom. Considering the same heating power along the ground pad, the high temperatures requires longer time to propagate to the surface of thick tissue. The geometry of liver samples was observed important for the monitoring of the surface temperature. This issue is further discussed in Section 7.4.1.
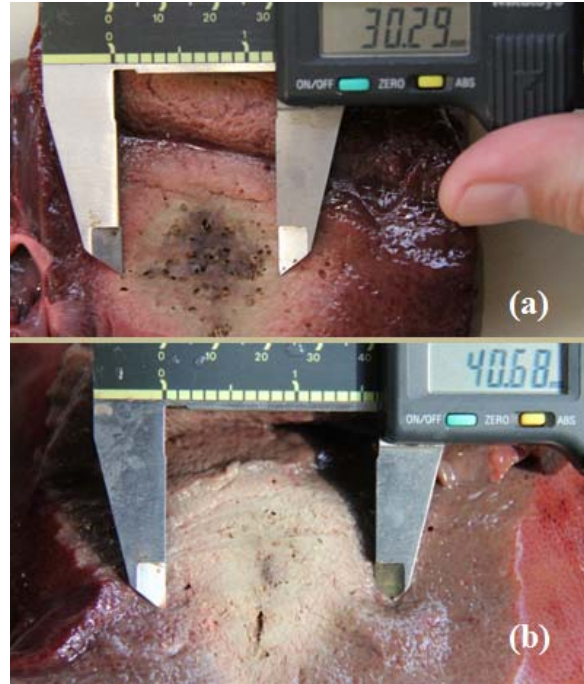
Figure 7.7 Measurements of the complete ablation zone. (a) Complete ablation zone by one-step invasion; (b) complete ablation zone by multi-step invasion.

Generally speaking, the procedure of multi-tine RF ablation depends on the volume of lesion. The influence of RF procedure can be dominant when the ablation zone is in large volumes. The importance of the RF procedure is shown in Figure 7.7 by comparing two scenarios. Both scenarios took the same the multi-tine RF probe with the development shaft at *Label* 4. They were tested under the same ATC mode. Figure 7.7 (a) measures the complete ablation zone after one-time ablation. The complete ablation zone obtained in short-axis was 30.3 mm. The lesion size of multi-step ablation is shown in Figure 7.7 (b). The RF ablation started with the development shaft at *Label* 2. When selected temperatures reached 373 K, the development shaft was moved to *Label* 3. Therefore, the electrodes were inserted further into the tissue and the electrode temperatures were reduced. We repeated the same operating procedure again so that the multi-tine electrodes were fully opened (*Label* 4). The size of the complete ablation zone in short-axis was 40.7 mm. Compared to Figure 7.7 (a), the ablation zone in Figure 7.7 (b) was uniform and complete. There were no observed charring shown in Figure 7.7 (a) due to the

overheating temperatures. Therefore, it is concluded that the multi-step ablation procedure was capable of producing large ablation zone with uniform temperatures.

7.3. Experimental observation of a simple hybrid process

With the understanding on RF ablation, we incorporated RF-generated heating into cryoablation. The RF electrode was placed 30 mm from the cryoprobe in parallel. As the duration of one-probe RF ablation was usually less than that of cryoablation, the cryo-freezing was activated 600 s ahead of RF ablation. Temperature developments of the hybrid cryosurgical process are shown in Figure 7.8. Results indicated that the temperature contours around the RF probe were not uniform. The high temperature propagated faster in the direction opposite to cryoprobe. The cryosurgery could change the temperature development of RF ablation.
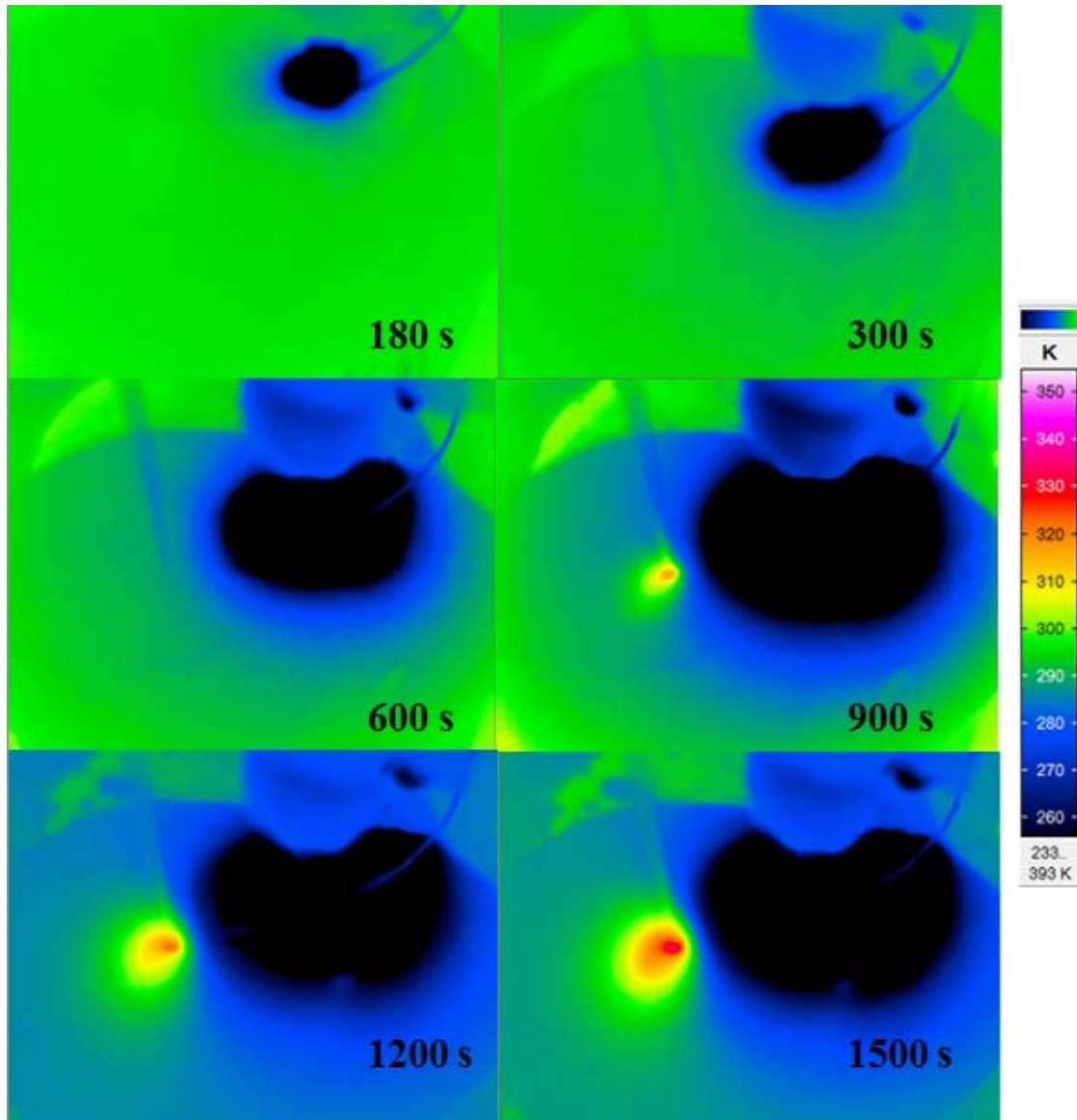
Figure 7.8 Temperature contours of cryosurgical process with RF ablation at 180 s, 300 s, 600 s, 900 s, 1200 s and 1500 s.

The change of temperature contours around the RF electrode is mainly resulted from two reasons. The first reason is obvious: the RF heating is dissipated in the low temperature region. The other reason is due to the change of electrical conductivity of biological tissue. When the tissue temperature falls, the electrical conductivity reduces and more RF currents tend to flow to tissue with high electrical conductivities.

The second reason is not applicable for the cartridge heating. The cartridge

heating converts the electrical energy into the thermal energy within the cartridge heater. The change of electrical conductivity has no effects on the heat transfer. Therefore, compared to the cartridge heater, the RF electrode is less effective in reforming the temperature contour of the tissue with low temperatures.

7.4. Experimental tests of the cryosurgery with RF-generated heating

As observed in Section 7.3, the variation of current resistance has reformed the scope of RF ablation; that is, the RF ablation is influenced by the electrical conductivity of tissue. Inspired by this concept, we have proposed several tests to manipulate the scope of RF-generated heating and develop feasible cryosurgical protocol to integrate RF ablation during cryoablation.

7.4.1. Test of the surface freezing

In this section, the invasive direction of cryoprobe was changed. The new allocation is shown in Figure 7.9. The cryoprobe was allocated within a layer close to the surface of porcine liver. The benefit of this design is that the formation of frozen tissue can be visualized along the cryoprobe. Figure 7.9 (a) shows the side view of the procaine liver sample. Figure 7.9 (b)-(d) show the formation of frozen tissue at 180 s, 1080 s and 1500 s, respectively. The flow rate during experiments was controlled at 250 L/min. The largest diameter of frozen tissue was 73.3 mm at 1080 s and 84.5 mm at 1500 s. The results are used to compare with results in Section 7.4.2 and 7.4.3.
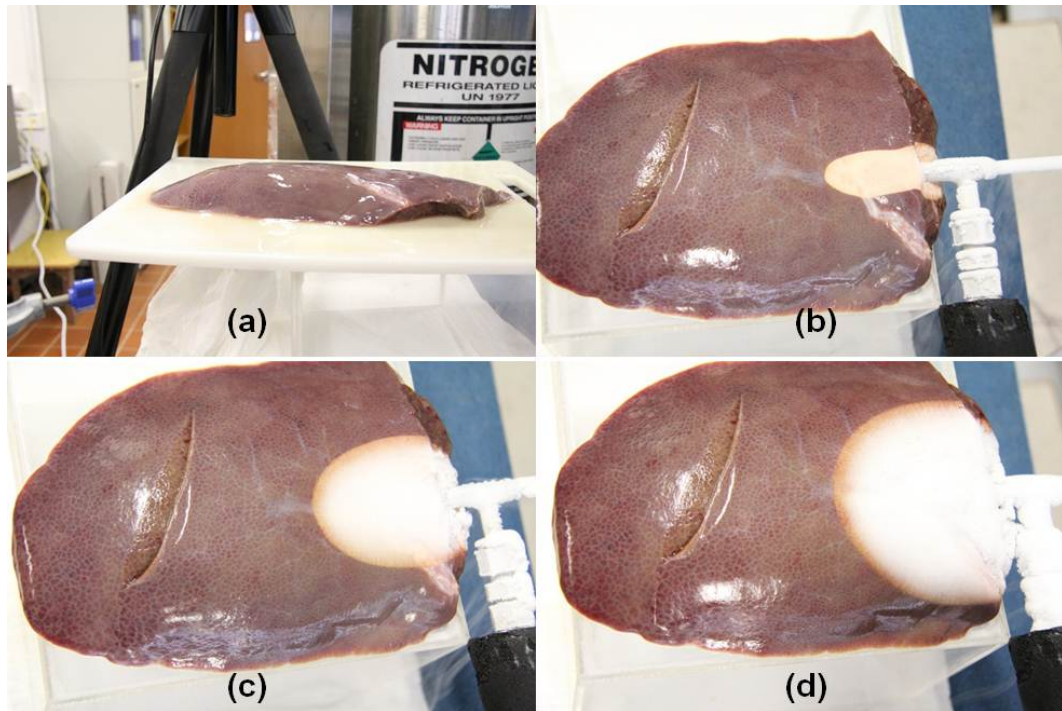
Figure 7.9 Surface freezing of a liver sample (a) side view of the liver sample; (b) 180 s; (c) 1080 s; (d) 1500 s.

It is important to ensure a similar testing environment so that the experimental results are comparable. It is observed that the testing environment for the infrared images could be largely influenced by sample geometry. This effect on the experimental observation is shown in Figure 7.10. Figure 7.10 (a) shows a liver sample while Figure 7.10 (b) and (c) show the infrared images at 480 s and 720 s, respectively. The sample geometries in Figure 7.9(a) and Figure 7.10 (a) are different. Figure 7.10 (a) displays a case that the surface of liver was not flat. The middle portion of the liver was significantly thicker than the surrounding. Even installed with the same experimental settings, the development of the frozen tissue was observed with a remarkable change.
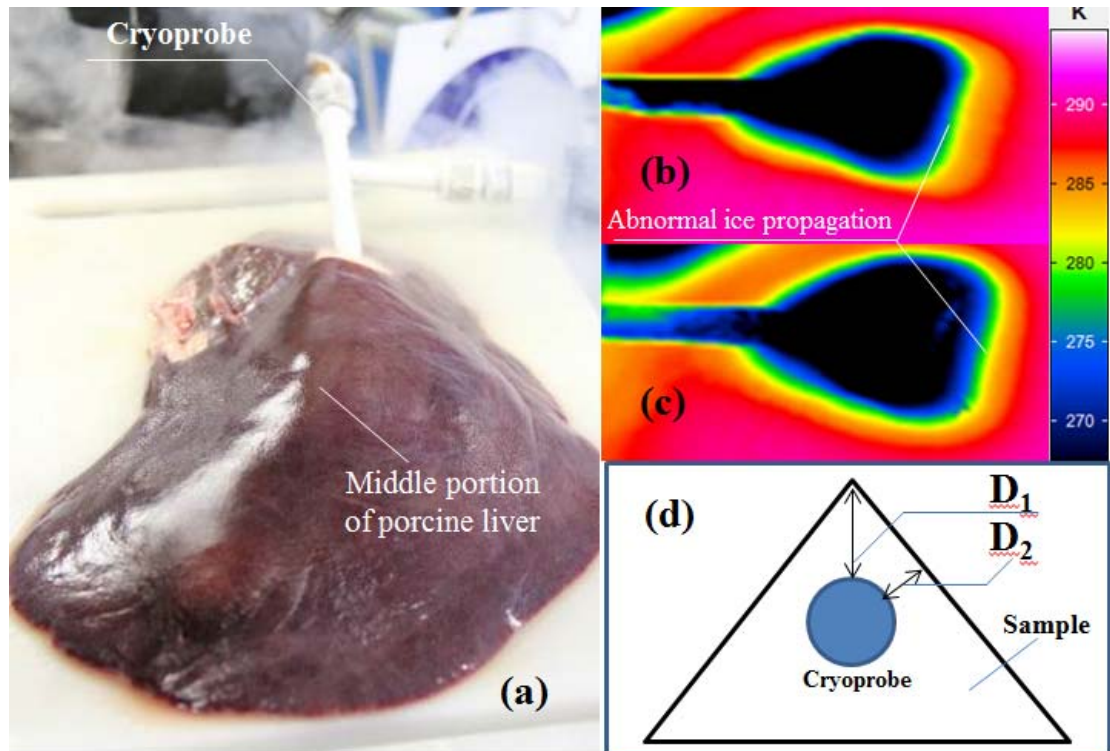
Figure 7.10 Effect of sample geometry on the experimental observation (a) picture of the porcine liver; (b) abnormal infrared image at 480 s; (c) abnormal infrared image at 720 s; (d) schematic diagram of a reason for the abnormal infrared images.

The experimental samples ought to be carefully selected; otherwise, when RF ablation is incorporated into cryoablation, it is difficult to explain the reason why the temperature profile of frozen tissue is changed. It is necessary to cut certain portion of porcine liver to ensure that the sample surface is relatively flat.

Two reasons are proposed to explain the abnormal infrared images of the frozen tissue in Figure 7.9. First, the waved surface of liver samples generated distorted temperature contours due to the image perspective. A characteristic feature of image perspective is that objects are drawn smaller as their distance from the observer increases. It well explained why the infrared images are asymmetric against the cryoprobe. The other reason was that the waved surface caused the undesirable invasive distance between the cryoprobe and the sample surface. Figure 7.10 (d) shows the schematic graph of the

undesirable invasive distance. A schematic triangle is taken as a sample with a waved surface. The invasive distances from the cryoprobe to the waved surface are different. The invasive distance D_1 is larger than D_2. The variation of invasive distances induced inhomogeneous boundary conditions so that temperatures on the surface were different.

7.4.2. Cryosurgery incorporating RF-generated heating with one ground pad

The main purpose of this section was to control and reshape the frozen tissue by integrating RF ablation with cryosurgery. The RF current can be used to generate heat and protect the surrounding healthy tissue from low temperatures. During the test, the RF probe was placed against the cryoprobe as shown in Figure 7.11. The development shaft of RF probe was located at *Label* 2. The distance between the tips of the two probes was 25 mm. The cryoprobe was activated 300 s ahead of RF ablation at a flow rate of 250 L/min. The RF probe was controlled by ATC mode. The ground pad of RF ablation system was placed under the porcine liver. It was designed to be placed near to the cryoprobe. Figure 7.11 (a) and (b) show the frozen tissue during experiment at 600 s and 1100 s. Compared to Figure 7.11 (a), Figure 7.11 (b) shows that the profile of the frozen tissue, especially in the region near to RF electrodes, has been reformed. The heat generated by RF ablation impeded the propagation of frozen tissue. Besides, the largest diameter (53 mm) of the frozen tissue in this test was observed to be 53 mm, which was compared to the diameter (73 mm) shown in Figure 7.9.
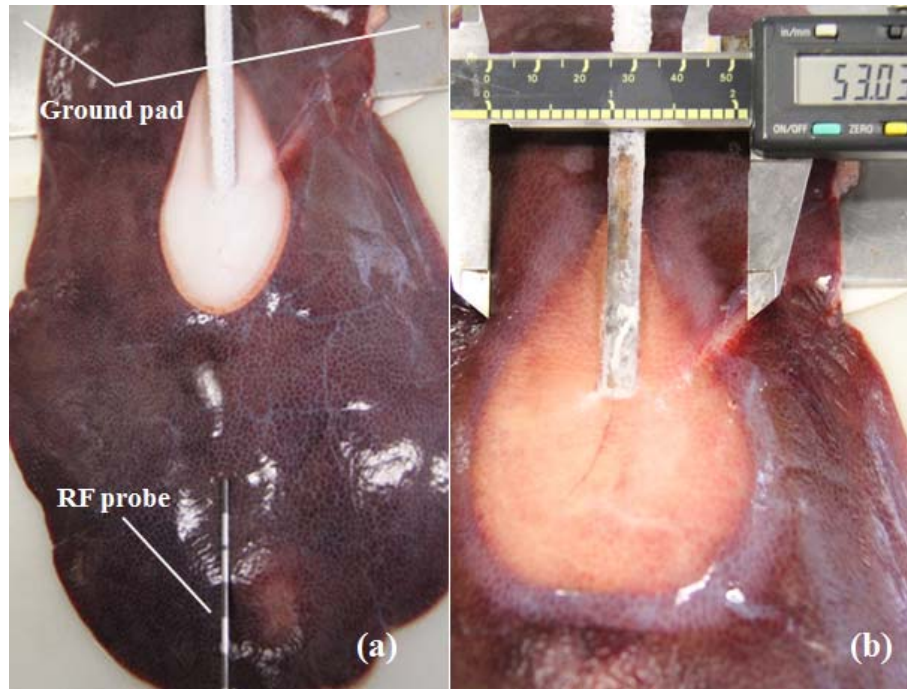
Figure 7.11 Cryosurgery incorporated with RF ablation (a) allocations of RF probe, ground pad, cryoprobe and RF probe; (b) the size of frozen tissue at 1080 s.

Figure 7.12 shows selected temperatures and the input power in response to ablation duration. The input power increased until the electrodes met the targeted temperature. The maximum input power was 71 W. Figure 7.12 indicates the electrodes T1-T4 varied within a small temperature range after 200 s; however, the temperature of central electrode T5 is lower than the rest. The temperature drop of T5 can be attributed to the cryo-freezing. The central electrode T5 is a straight electrode (shown in Figure 4.13) that is mostly near to the cryoprobe. Therefore, it is reasonable that the temperature of central electrode is lower than the rest.
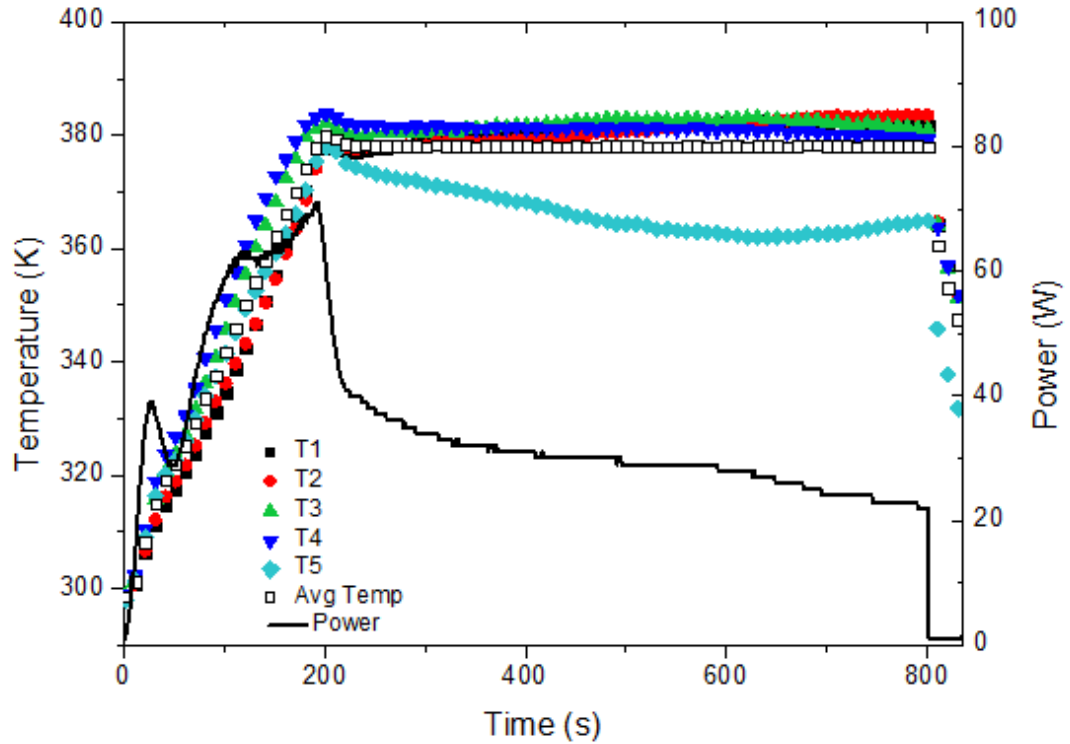
Figure 7.12 Development of probe temperatures and RF power with one ground pad. The x-axis is the duration for RF ablation.

Adopting RF ablation has largely reduced the size of frozen tissue. In Section 7.4.1, the diameter of frozen tissue grows to 73.3 mm at 1080 s while in this section, the diameter only increases to 53.0 mm within the same operating duration. The RF ablation has successfully reduced the size of frozen tissue. The monitored tissue temperature contours are shown in Figure 7.13. Figure 7.13 (a)–(c) show the temperature contours at 300 s, 600 s and 1080 s. These graphs illustrate that the RF-generated heating surrounded the frozen tissue. The RF heating was intense in the direction towards the ground pad and in contrast, it was weak in the direction along the insulated shaft.
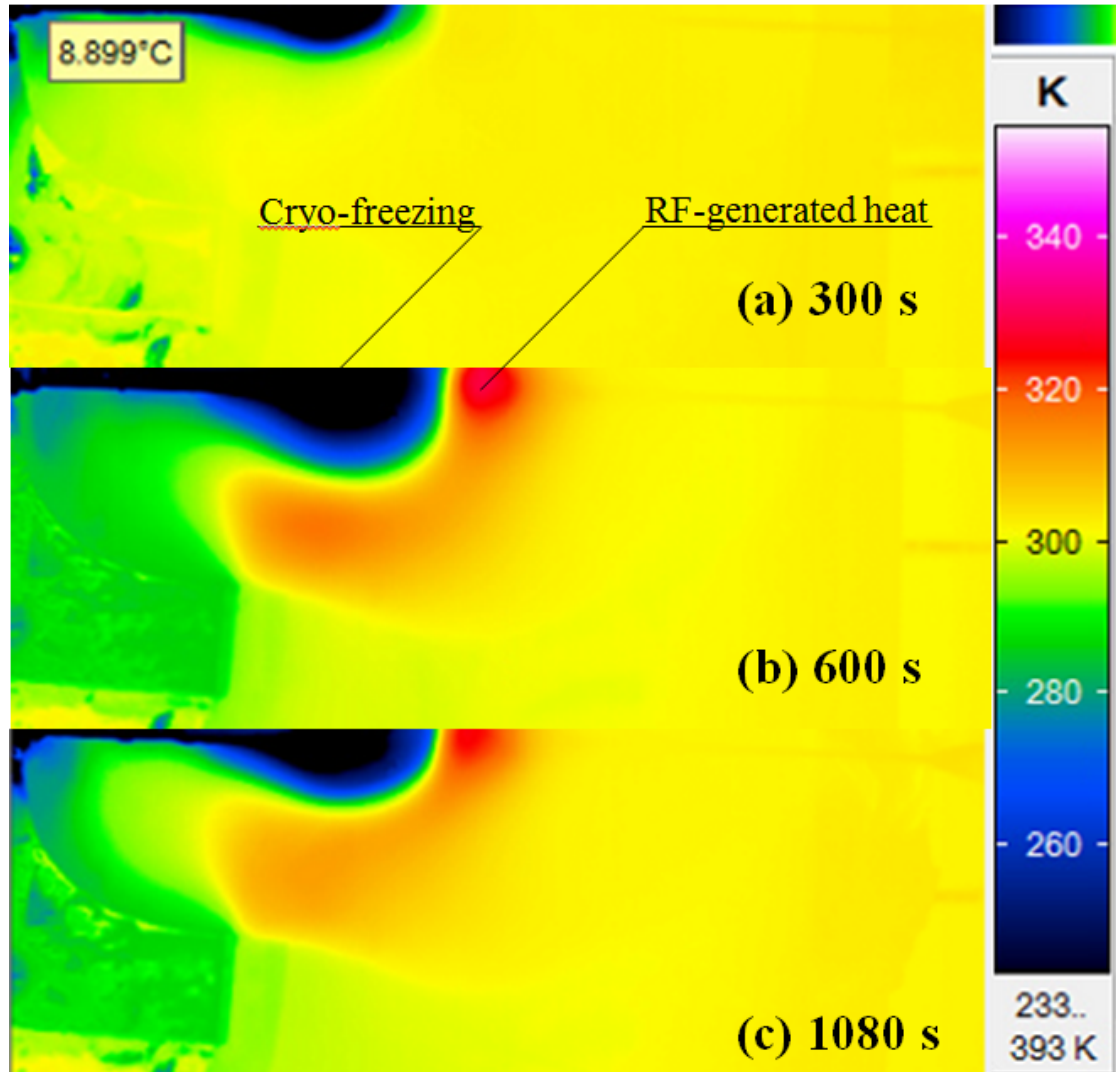
Figure 7.13 Infrared images of tissue temperature at 300 s, 600 s and 1080 s.

7.4.3. Cryosurgery incorporating RF-generated heating with discrete ground pads

In this section, we studied the thermal influence due to multiple ground pads. To simplify experimental facility, we used an insulator pasted on the ground pad and placed the liver on top of the insulator. Therefore, only portions of the ground pad without covering the insulator were effective in the electrical conduction. The ground pad covered with insulator was considered as "discrete ground pads". The placement of ground pad with a 64 mm-width insulator is shown in Figure 4.14.

144
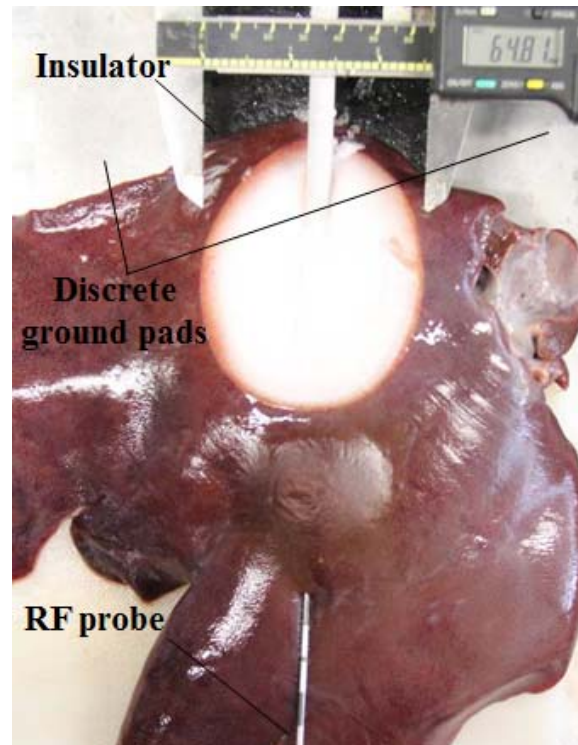
Figure 7.14 Cryosurgery with RF-generated heating with two discrete ground pads.

Besides the change in the ground pad, the operating settings of both RF probe and cryoprobe were consistent with the settings in Section 7.4.2. Similar to the thermal contours shown in Figure 7.13, the RF-generated heating has reduced the diameter of the frozen tissue. The diameter of the frozen tissue at 1080 s was 64.8 mm in Figure 7.14.
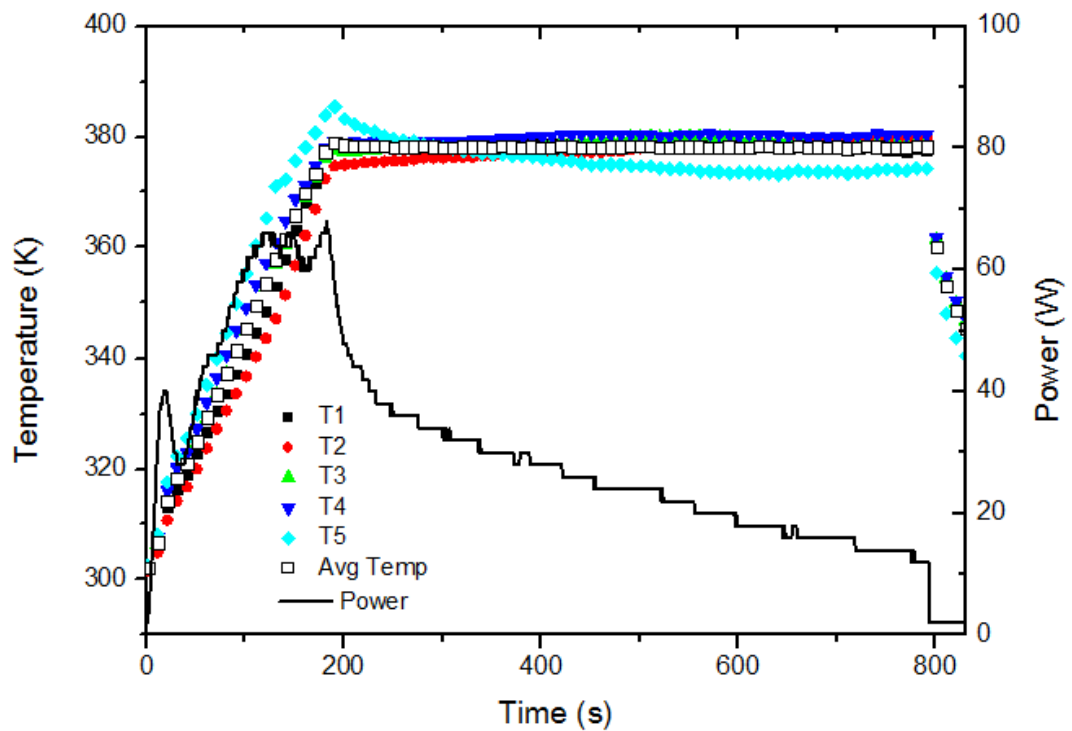
Figure 7.15 Electrode temperatures and RF input power tested with discrete ground
pads. The x-axis is the duration for RF ablation.

The probe temperatures and input power are shown in Figure 7.15. The
maximum input power was 69 W at 190 s. The initial heating duration and
input power were very identical to the results in Section 7.4.2. T5 was still
associated with lowest temperatures after 300 s compared to other electrodes.
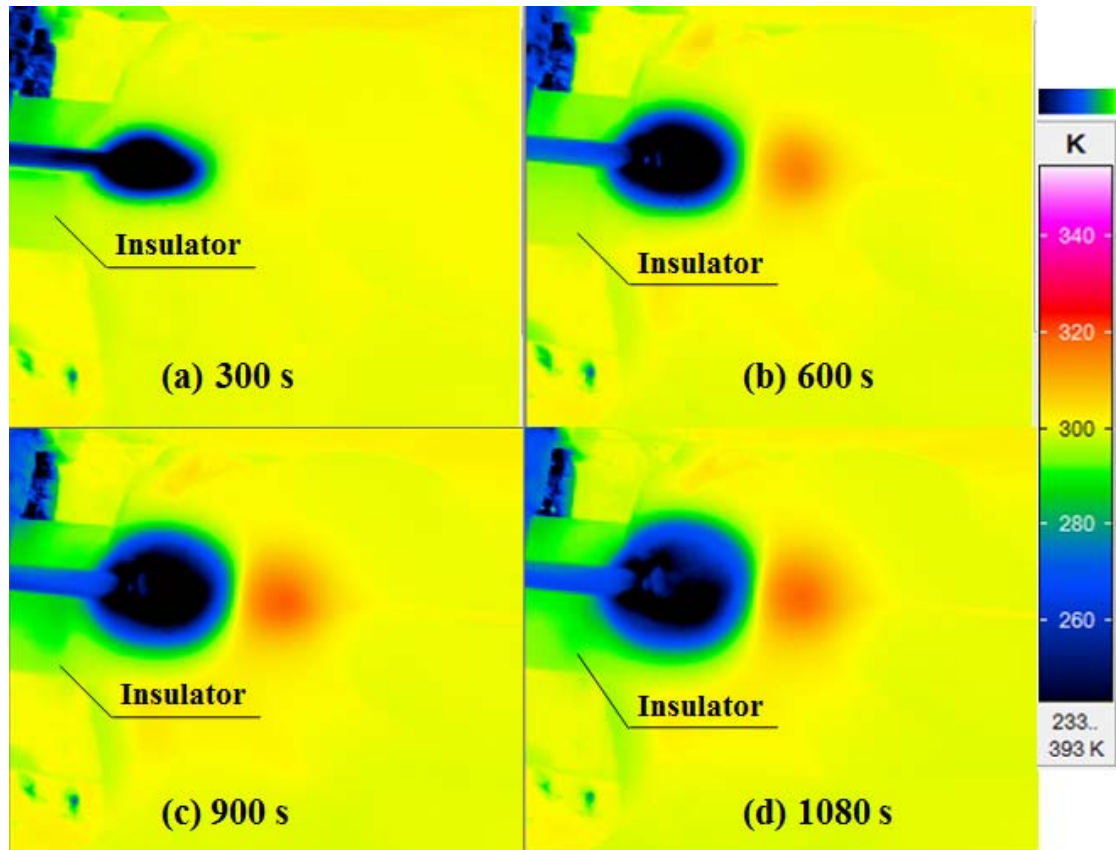
Figure 7.16 Infrared images of tissue temperature with discrete ground pads at 300 s, 600 s, 900 s and 1080 s.

Figure 7.16 (a)-(d) display the temperature distribution with discrete ground pads at 300 s, 600 s, 900 s and 1080 s, respectively. The discrete ground pads were divided by an insulator marked. There are several reasons contributing to the temperature difference between the insulator and the ground pad. First, the insulator was directly attached to tissue with low temperatures. The temperature of insulator reduced as the size of the frozen tissue increased. Second, compared to the conventional cryosurgery, the RF-generated heating nearby the ground pad impeded the temperature drop of the ground pad.

Table 7.2 Summary of key parameters of the three scenarios in Section 7.4.

	Cryoablation	RCA with a ground pad	RCA with discrete ground pads
Duration (s)	1080	1080	1080
Gas flow rate (L/min)	250	250	250
Diameter of 265 K isotherm,	73.3±1.5	53.0±1.4	64.8±1.5

short-axis (mm)			
Diameter of 233 K isotherm, short-axis (mm)	14.8±0.8	14.0±0.8	14.5±0.6
Max. RF input power (W)	N/A	71	69
Time at Max. Power (s)	N/A	191	190

* RCA: RF-assisted cryosurgical ablation; short-axis of the frozen tissue is in the direction perpendicular to cryoprobe.

Table 7.2 lists the key parameters tested in cryoablation and RF-assisted cryosurgical ablation. To be comparable, the same freezing duration was selected under the same flow rate of the freezing medium. It shows that the maximum RF input power and the duration to achieve the maximum power were very close for two hybrid ablations. However, the hybrid ablation with discrete ground pads allowed reforming the diameter of frozen tissue. The hybrid cryosurgical ablation with one ground pad and discrete ground pads reduced the short-axis diameter of frozen tissue by 27.7 % and 11.6 %, respectively. However, the complete ablation zone (233 K isotherm) for these two hybrid ablations only decreased by 5.5 % and 2.1 %, respectively. Therefore, it is concluded that the RF-assisted cryosurgery can largely reduce the frozen tissue while sustaining the size of the complete ablation.

7.5.   Model validation and grid resolution

COMSOL 4.2 Multiphysics was used to solve the numerical model and obtain simulated data at all node of the finite element mesh. An finite element model with an initial coarse grid of 29462 elements was used to test the reliability of the model. Due to *in-intro* testing conditions, the initiate temperature was set to be 293 K and the biological heat generations (metabolism and blood perfusion) were deactivated. The validation of RF ablation was conducted by single RF probe with the schematic diagram shown in Figure 3.2. The properties that used in the simulation were listed in Table 5.3. The RF

generator supplied voltage at a frequency of 460 kHz. The temperature validation of the RF mode is shown in Figure 7.17.
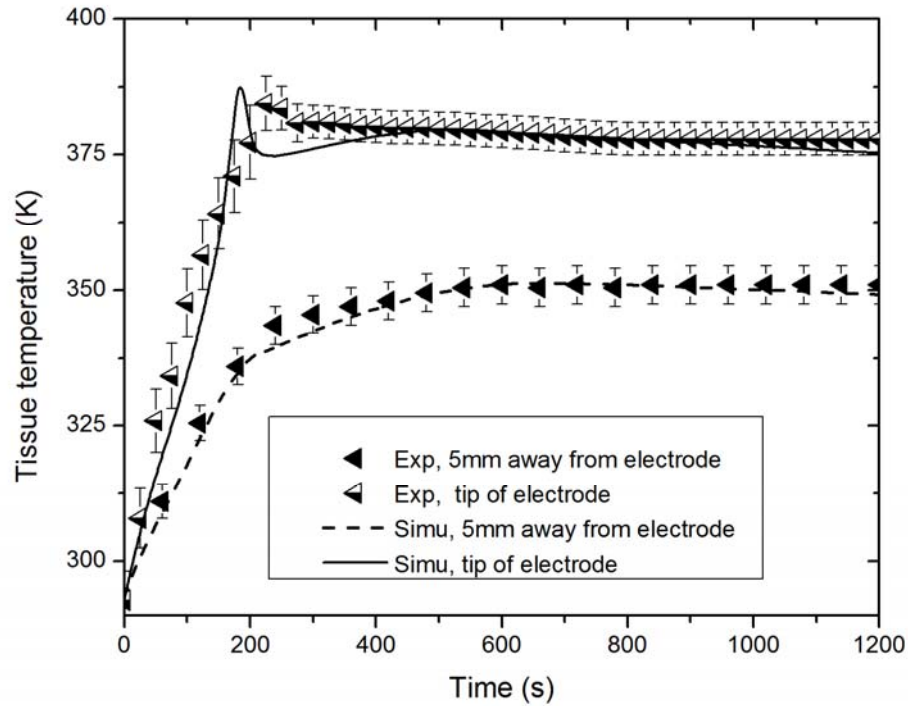
Figure 7.17 Validation of RF ablation model by temperatures.

Figure 7.17 illustrates the temperatures at two monitoring locations in the domain of RF experiments and the corresponding simulated results. One is the electrode temperature and the other one is the tissue temperature 5 mm from the electrode. Experimental results are shown in dots while simulated results are displayed with lines. The error bars represented the standard deviation of the temperature readings obtained by three experiments. The maximum temperature differences of the simulated and experimental data for these two sets of data were 6.8 % and 3.1 %, respectively.

A grid independent test was conducted for the simulation of RF ablation. The grid resolution was studied by comparing temperatures between simulated and experimental data. Three meshes of 37593, 29462 and 20485 were divided for the model. Results indicated that the largest temperature difference obtained

with these meshes were 6.1 %, 6.8 % and 7.3%, respectively. With the balance of the computational time and model accuracy, the mesh size of 29462 was taken in the simulation of single RF electrode.

7.6. Simulation of a single RF probe and a multi-tine RF probe

Since the focus of this section is mainly on the hybrid method of RF ablation and cryosurgical ablation, the simulations on pure RF ablation were briefly disclosed. Single RF probe contained an insulated shaft followed by a 20 mm conducting tip. The conducting tip was inserted into the biological tissue with an initial temperature of 293 K. The thermal development of the simulation with a single RF electrode is shown in Figure 7.18.
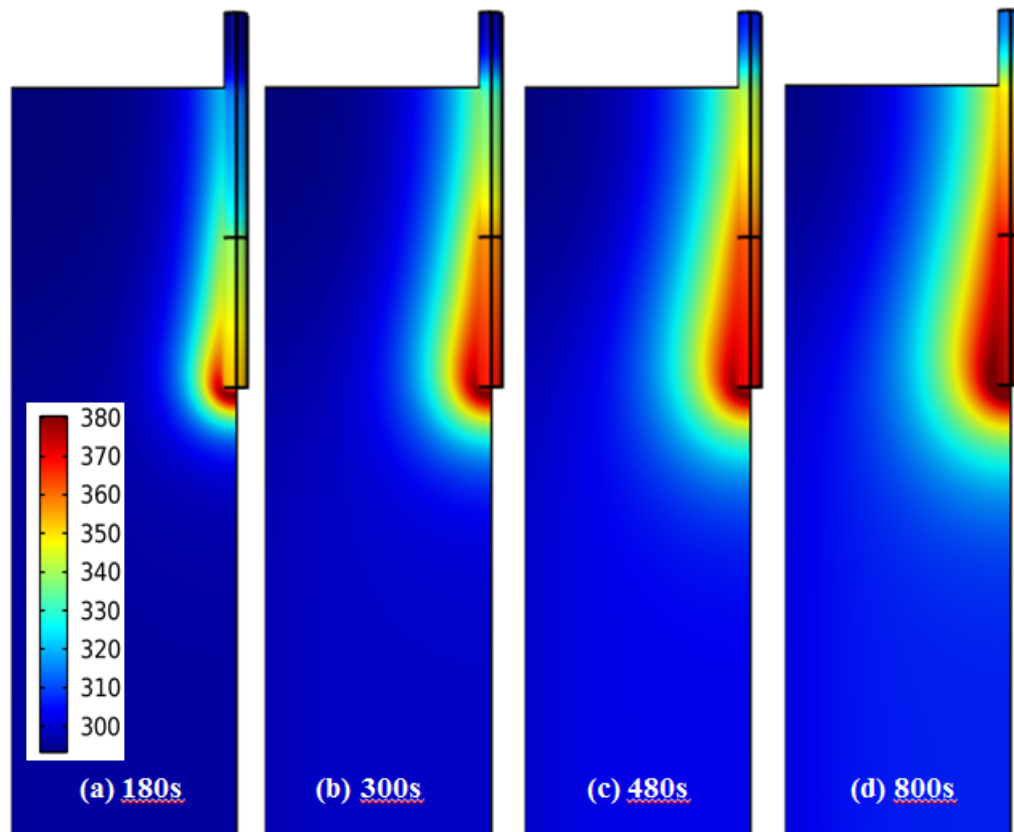
Figure 7.18 Comparison of temperature distributions computed at 180 s, 300 s, 480 s and 800 s.

Figure 7.18 shows the cross-sectional temperature distributions computed at

180 s, 300 s, 480 s and 800 s. It can be observed that the tissue temperature was raised up in the region close to the distal portion of the electrode. The high temperatures propagate to the surrounding tissue. The diameter of 328 K isotherm at the end of the electrode was measured to be 22.5 mm at 800 s. Compared to our experimental results in Table 7.1, the simulated result has coincided well with experimental observation with the lesion diameter of 21.5 mm.

The multi-tine RF probe has been widely used to enlarge the size of the ablation zone. We simulated the thermal response of the multi-tine electrodes with the schematic diagram given in Figure 3.3.
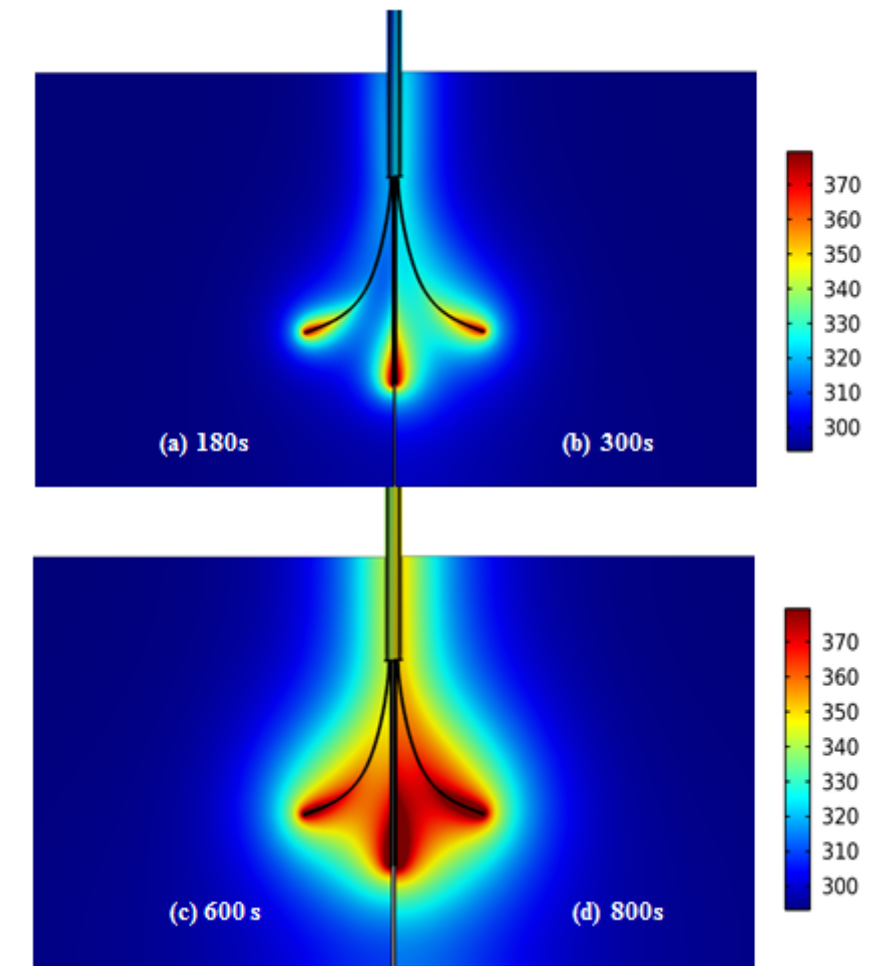
Figure 7.19 Comparison of temperature distributions computed at 180 s, 300 s, 600 s, and 800 s.

Figure 7.19 shows the temperature contours of multiple-electrode ablation at 180 s, 300 s, 480 s and 800 s. Similar to the single RF electrode ablation, the tissue temperatures were raised up in the region close to the distal portions of electrodes. The diameter of 328 K isotherm at the end of the electrode was measured to be 43.4 mm at 800 s.

7.7.   Simulation on a RF-assisted cryoprobe

Section 7.4 has disclosed that it was possible to use RF-generated heating to reduce the unwanted frozen tissue. Therefore, we incorporated RF electrode into the cryoprobe to produce a new cryo-device coined as "RF-assisted cryoprobe". The concept of the RF-assisted cryoprobe is shown in Figure 7.20. The RF electrode and the ground pad are incorporated in the two sides of the freezing portion. Two insulators with low thermal/electrical conductivity are taken among the ground pad, freezing portion and the electrode.
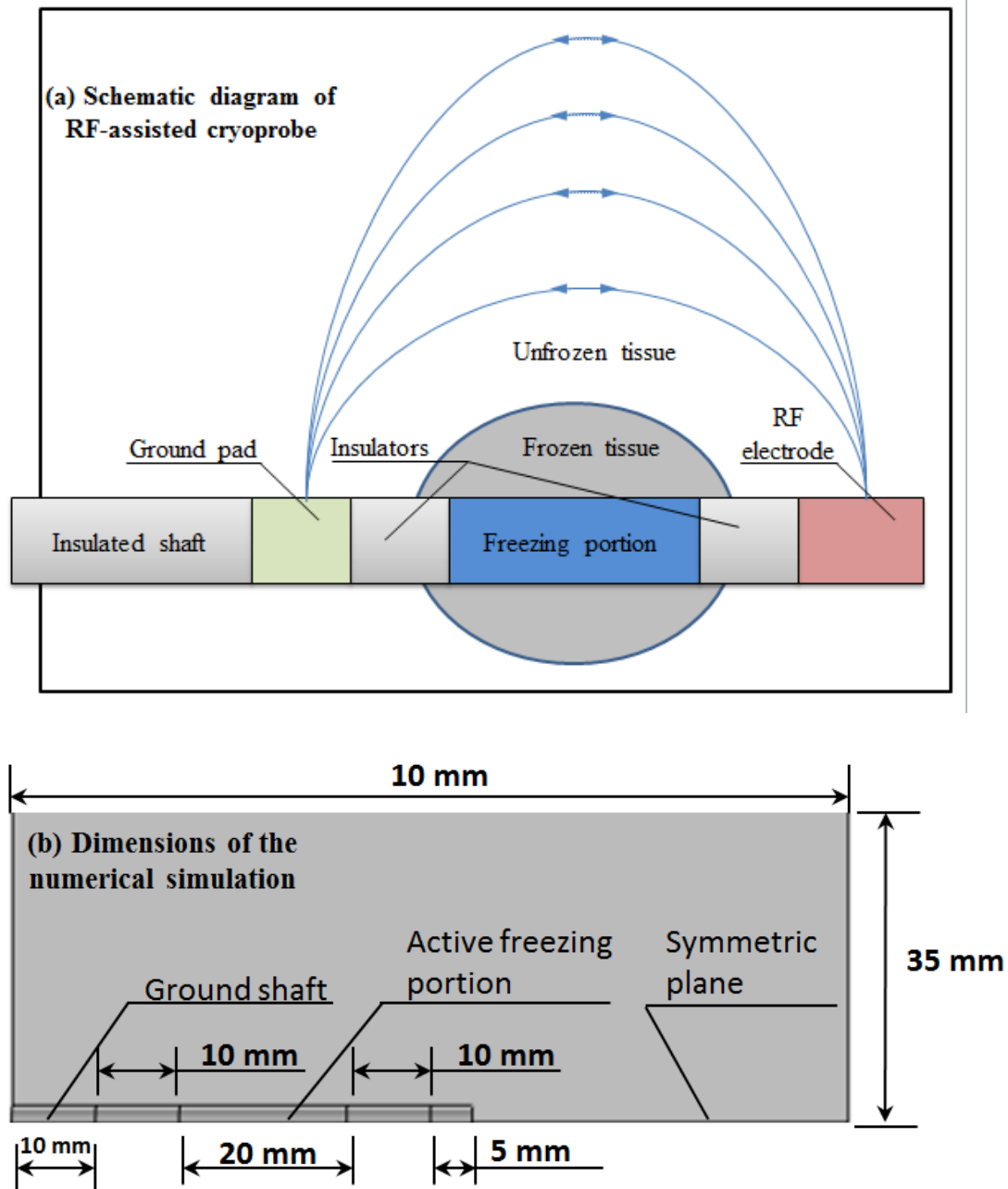
Figure 7.20 Depiction of RF-assisted cryoprobe. (a) schematic diagram of a RF-assisted cryoprobe; (b) dimensions of the numerical simulation.

The cryo-freezing was activated 300 s ahead of RF ablation. The reason that the cryo-freezing was initiated ahead of RF ablation was due to three reasons. Firstly, the cryo-freezing requires higher energy threshold than the RF ablation. The difference between critical temperature for cryo-freezing (i.e. 233 K) and the normal tissue temperature (i.e. 310 K) can be four or five times of the temperature difference between or the critical temperature for heating (i.e. 325

K) and body temperature. Secondly, the cryoprobe can reduce to extremely low temperatures. However, RF ablation probe is regulated with a temperature ceiling. The constrain was because that high temperatures may dehydrate the tissue and form a strong tissue attachment. Thirdly, the main focus of this dissertation is cryosurgery. RF-generated heating only serves as a complementary tool to promote the performance of ablation.

7.7.1. Cryo-freezing generated by the RF-assisted cryoprobe
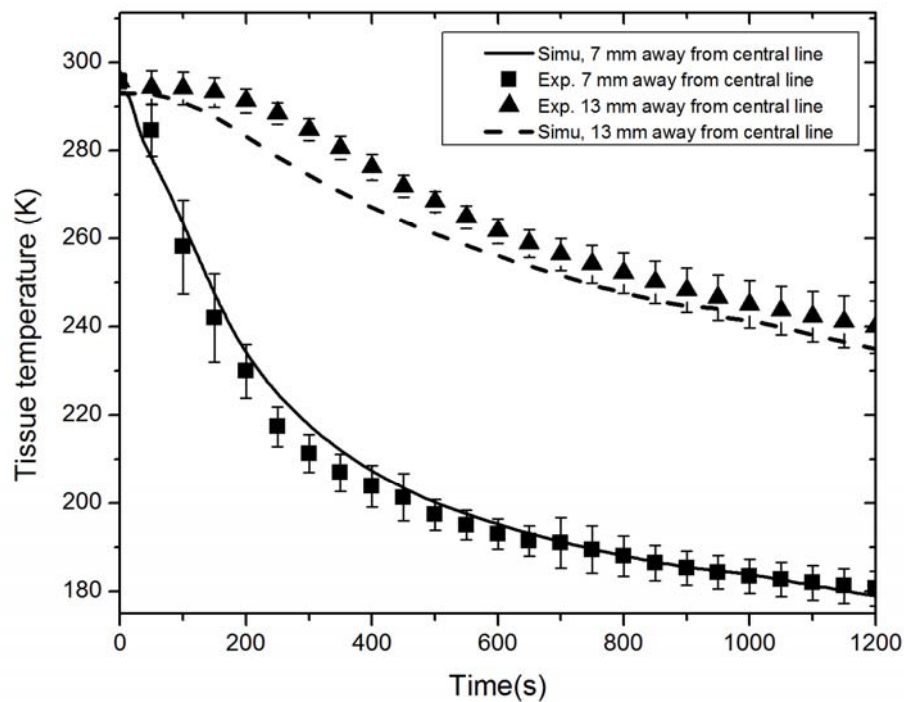
Figure 7.21 Validation of the temperatures with RF-assisted cryoprobe, when RF heating is deactivated.

Figure 7.21 shows the validation of the numerical model by temperature readings at 7 mm and 13 mm from the RF-assisted cryoprobe. The error bar represents the standard deviation of uncertainty. The temperatures were taken by two thermocouples at predetermined locations. As experiments were conducted in *in-vitro* tests, the metabolism and the blood perfusion terms were deactivated. The initial temperature of the simulation was 293 K. The maximum temperature difference between the simulated and experimental data

is 7.8 %.
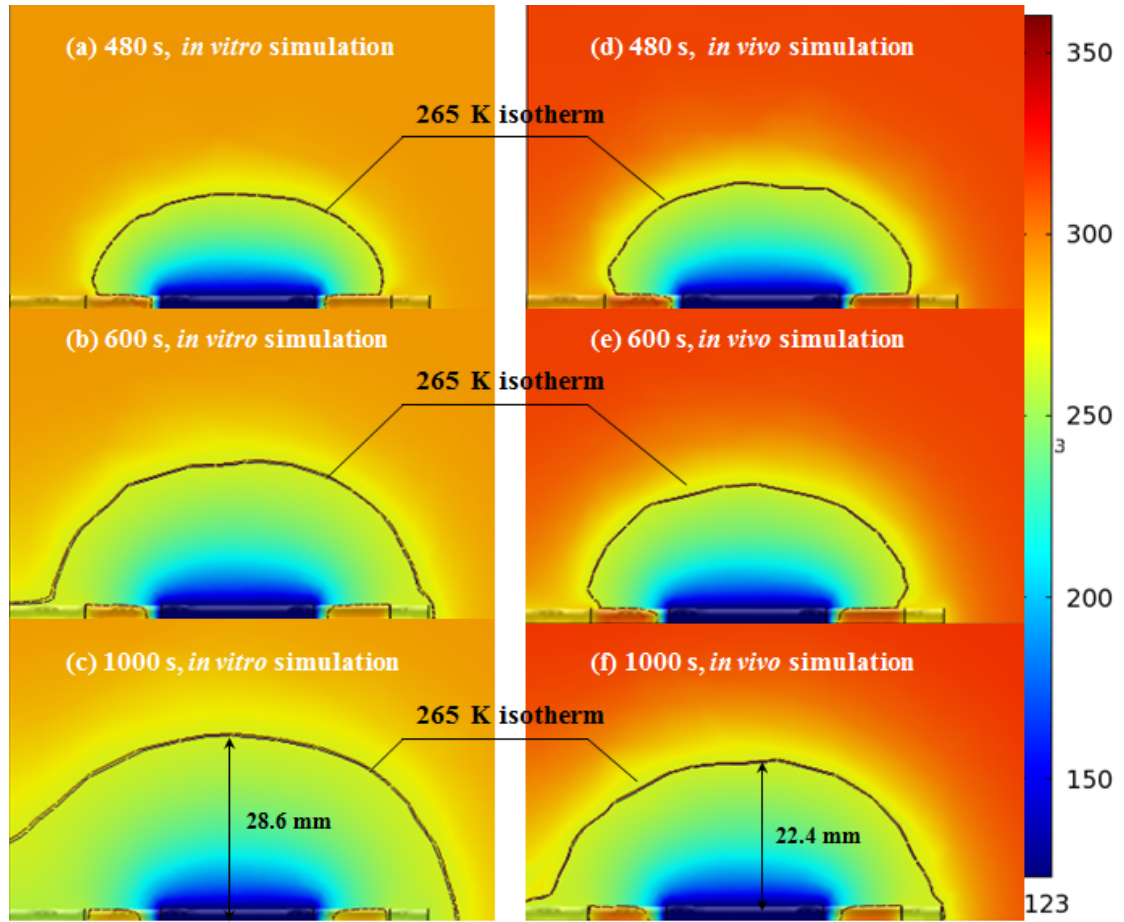
Figure 7.22 simulations of the freezing process in in intro and in vivo. (a)-(c) display temperature contours in in vitro tissue at 480 s, 600 s and 1000 s, respectively. (d)-(f)display temperature contours in in vivo tissue at 480 s, 600 s, and 100 s, respectively.

The metabolism term and the blood perfusion rate terms were activated to simulate the *in-vivo* biological condition. The values of properties are listed in Table 5.3. The initial temperature of *in vivo* tissue was 310 K. Figure 7.22 compares the cryosurgical process *in vitro* and *in vivo* tissue at three selected freezing durations. In order to identify the difference between the *in vitro* and *in vivo* tests, we have monitored the development of 265 K ice front. The 265 K isotherm was marked on these graphs. The largest radius of 265 K isotherm for in *in vitro* simulation was 28.6 mm at 1000 s while the *in vivo* simulation only obtained 22.4 mm within 1000 s. The comparison shows that the 265 K

isotherm was reduced by 21.7% in radius *in vivo* test comparing to the *in vitro* test. The metabolism and blood perfusion have a large influence on the temperature distribution.

7.7.2. The effects of the applied voltage on the RF-assisted cryoprobe

RF-generated heating used in this work is only a complementary tool to the boundary of the frozen tissue. Therefore, high temperatures above the critical temperature (i.e. 325 K) that forms a complete ablation are not desirable. We only use the RF-generated heating to protect tissue. The complete ablation generated by the RF-assisted cryoprobe is mainly created by cryoablation.
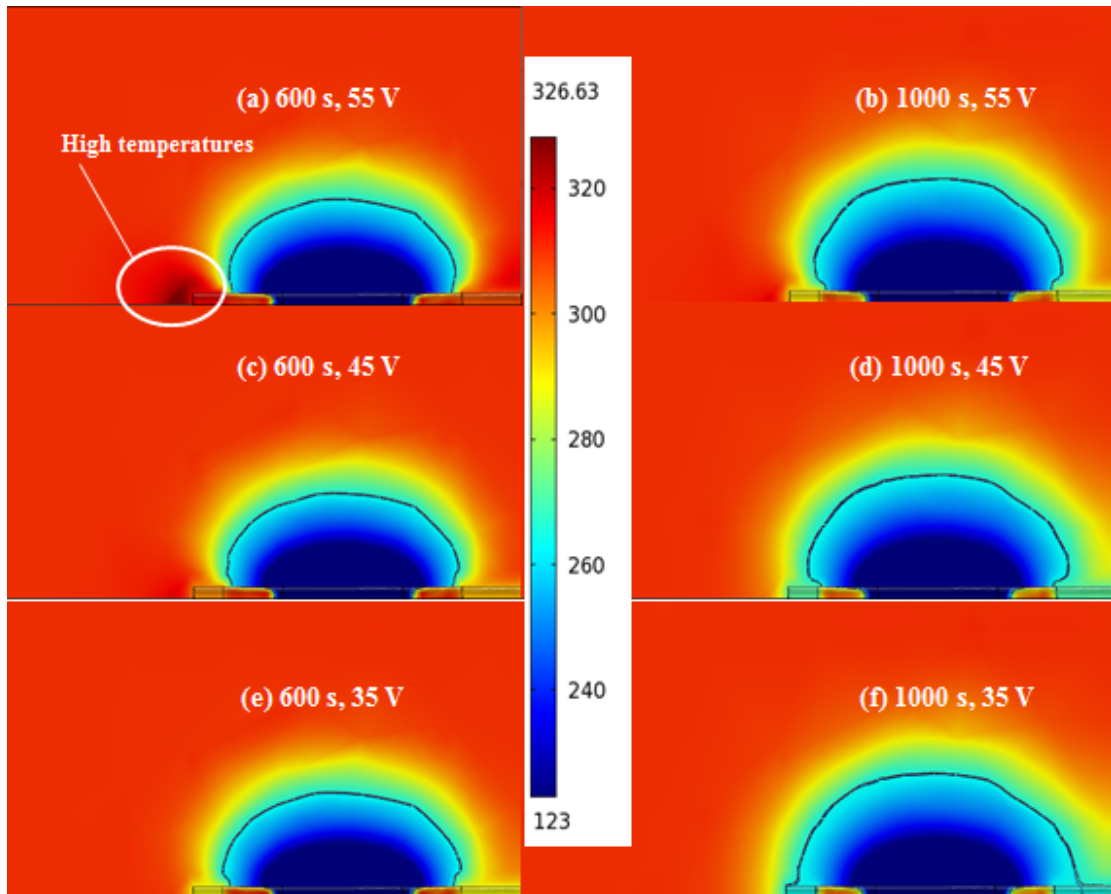
Figure 7.23 the effects of the applied voltage on the temperature contours at 600 s and 1000 s. (a)-(b) 55 V; (c)-(d) 45 V; (e)-(f) 55 V.

Figure 7.23 shows thermal impacts of RF-assisted probe in response to three

voltages. Figure 7.23(a) indicates that the high temperature region was located in the tissue close to the electrode. The highest temperature was 329.5 K. This high temperature zone was reduced when the ablation time extended to 1000 s as shown in Figure 7.23(b). This was because of the propagation of the frozen tissue. The frozen tissue can be depicted with long-axis (along cryoprobe) and short-axis (perpendicular to cryoprobe). Simulation shows that the long-axis radius grew from 38.4 mm at 600 s to 42.5 mm at 1000 s. Furthermore, it is observed that the short-axis radius of the frozen tissue at 600 s was 19 mm in the RCA (RF-assisted cryosurgical ablation) at 35 V, while the radius for RCA at 55 V was only decreased to 18.5 mm. Therefore, it is concluded that the increase in the applied voltage could reduce the size of the frozen tissue; however, according to simulation with the voltages ranging from 35 V to 55 V, the increased voltage only induced a marginal reduction of the frozen tissue.

Table 7.3 Summary of the size of the frozen tissue in short-axis and long-axis

| Parameters | 600 s | | 1000 s | | Max.Temp (K) |
	short-axis radius(mm)	long-axis radius(mm)	short-axis radius(mm)	long-axis radius(mm)	
CA	22.4±1.8	42.4±1.5	26±0.8	55.2±1.2	310.0
RCA at 55 V	18.5±1.2	38.4±0.8	20.3±1.2	42.5±1.4	329.5
RCA at 45 V	18.7±1.5	39.5±1.2	20.4±0.9	42.4±1.5	317.1
RCA at 35 V	19.0±0.8	40.5±0.6	20.5±1.5	49.5±0.8	315.2

CA: cryoablation; RCA: RF-assisted cryosurgical ablation.

Table 7.3 summarizes the short/long-axis radius at 600 s and 1000 s with their maximum temperatures. RCA at 55 V was not desirable, since the RF-generated heating has induced lethal damage to the surrounding tissue. More importantly, the increase of the voltage from 45 V to 55 V has only generated a marginal change of the frozen tissue. Compared RCA at 45 V with 35 V, we find that both RF-generated heating have avoid high temperatures to damage the surrounding tissue. However, RCA at 35 V has a very large long-axis radius (49.5 mm) at 1000 s. This is mainly due to the low RF input power.

7.7.3. Specific absorption rate

Specific absorption rate of tissue measures the rate at which RF energy is absorbed by the biological tissue. It refers to the power absorbed per mass of tissue and can be defined as

$$SAR = (\sigma |E_f|^2)/\rho \qquad (7.1)$$

where σ is the electrical conductivity and E_f is the electric field. We calculated the SAR based on the temperature-dependent electrical conductivity and the electric field. The SAR contours are shown in Figure 7.24.
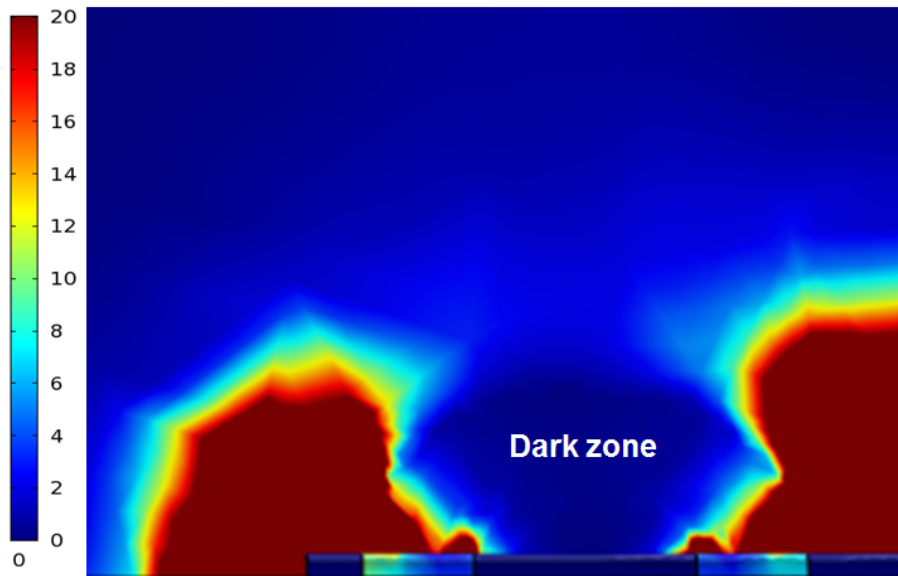
Figure 7.24 Contour of specific absorption rate at 480 s with applied voltage of 45 V.

Figure 7.24 displays the contour of specific absorption at 480 s when RF voltage is 45 V. The large SAR values in tissue were formed near the RF electrode and the ground pad. There was a marked dark zone with low SAR between the ground pad and electrode. The main portion of this dark zone was the tissue in frozen state. In other words, the frozen tissue had a very low ability to absorb the RF energy. This result was coincided with our experimental observation in Section 7.3.
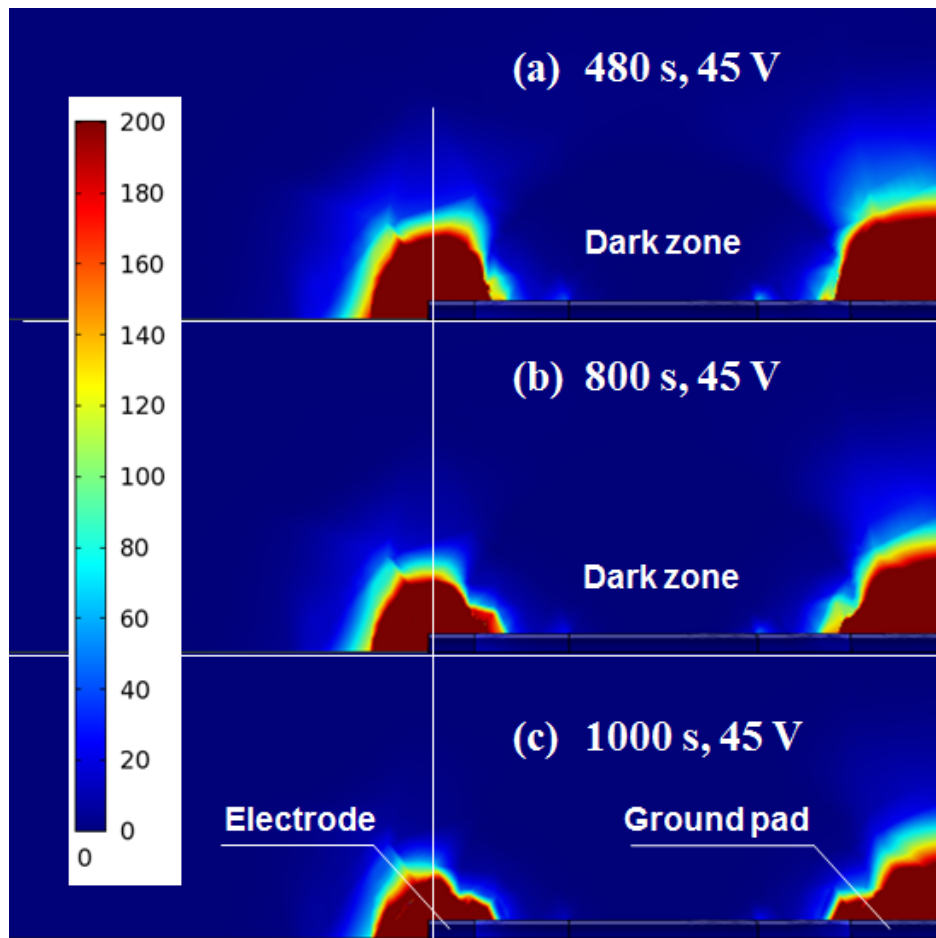
Figure 7.25 Contours of SAR at 480 s, 800 s and 1000 s when the RF voltage is 45 V.

Figure 7.25 compares the contours of specific absorption rate when RF voltage was 45 V. The maximum values at 480 s, 800 s and 1000 s were 15450 W/m^3, 12262 W/m^3 and 8271 W/m^3. However, only a very small region of the tissue was associated with such a large SAR. Most tissue close to the electrodes was below 1000 W/m^3. It is found that the SAR was reduced as the freezing proceed. The boundary of 200 W/m^3 (dark red) shown in Figure 7.24 was reduced from 480 s to 1000 s. The dark zone increased with time due to the propagation of low temperatures.

Chapter 8:   Conclusions and Recommendations

In Chapter 8, we summarize main conclusions and contributions to the knowledge obtained in this dissertation. Besides, the limitations associated with this study are discussed. Several recommendations are proposed for the future work.

8.1.   Conclusions

Chapter 5, Chapter 6 and Chapter 7 contain all results obtained in this dissertation. Chapter 5 optimizes the freezing processes while Chapter 6 and Chapter 7 incorporate Joule heating devices and RF-generated heating elements to enhance the treatment of solid tumors. Both experiments and simulations have been conducted. The simulated results agreed well with experimental data. The results have shown that the improvements involve promising features to enhance the accuracy of cryosurgical planning and the success rate of cryosurgery.

In chapter 5, the performance of cryosurgical system due to key controlling factors was investigated using the orthogonal experimental methodology. The real-time fluctuations of flow rate and entrance pressure were monitored in a conventional cryosurgical system. In the modified system, the fluctuations have been successfully reduced so that the system can deliver the freezing with more accuracy. The phenomenon of "pressure jump" was observed at the beginning of freezing under the protocol of constant flow rate. The pressure must be reduced to maintain the flow rate of freezing medium. In contrast, under the passive controlling protocol where the pressure maintains constant, the temperature depreciation of cryoprobe increased within the initial freezing.

These two controlling protocols were capable of manipulating the temperature profile of cryoprobe. Furthermore, the system response made by liquid level of freezing medium on the freezing process was evaluated. The relation between liquid levels and the minimum temperatures was established. By adopting the orthogonal experiment analysis, the flow rate was found to be the major impact factor for the initial freezing while the nitrogen liquid level exerted the principal influence of producing the minimum temperature.

An analytical study was conducted to investigate the performance of several unconventional bifurcate probes specifically designed to treat irregularly shaped tumors. The successful application of bifurcate cryoprobe saved the healthy tissue by producing a closely matched ablation zone to the tumor profile. Compared to a conventional cryoprobe, a bifurcate cryoprobe with $\beta=75°$ could generate a 51.1% larger complete ablation zone with a high degree of profile irregularity. Among the three bifurcate cryoprobes, the one with $\beta=75°$ generated the largest complete ablation zone incorporated with the highest profile irregularity, but it incurred the penalty of higher invasive trauma compared to the total tissue damage.

To improve the success rate of cryosurgery with large blood vessels, we developed a model to simulate heating effects of dominant vessels. A case study was conducted incorporated with a human vascular network taken from a CT-scanned image for the first time. The model enabled cryosurgeons to achieve greater success rate by knowing how to regulate the development of ice front. The case study revealed that by precisely controlling the freezing process, up to 44.6 % of the unintended freezing tissue could be protected. It is also shown that blood vessels with large flow rates markedly reformed the evolved temperature profile. However, the vascular effects impacted on the isotherm at lower temperatures (i.e. 233 K) were less than the isotherm at

higher freezing temperatures (i.e. 265 K). This observed phenomenon can be explained due to the formation of a thermal "buffer zone".

In Chapter 6, Joule heating elements were incorporated as complementary tools to enhance the cryosurgical performance. A hybrid freeze-thaw cryoprobe was capable of regulating the unwanted frozen zone for internal tumors while a heating coil was proposed to assist cryosurgery for surface tumors. The performance of a hybrid cryoprobe under cyclic freeze-thaw conditions promoted the cryoablation efficacy. The hybrid probe incorporated several expandable antenna-like hooked-shape heaters to a central freezing probe. The probe could generate freezing and peripheral heating effects. It regulated the propagation of ice front while sustaining an excellent coverage of complete ablation zone. The implementation of several freeze-thaw cycles has produced a "temperature diminishing effect" whereby the minimum tissue temperature was observed to reduce at decreasing rate after each freeze-thaw cycle. The amount of tissue ablation was quantified when the hybrid cryoprobe operated under a cyclic freeze-thaw condition. A temperature-based cell damage rate, having close agreement with data derived from literature, was proposed to quantify the cell destruction. The proposed hybrid probe had the capability to promote tissue ablation by controlled freezing followed by repeated external peripheral thawing.

To protect the healthy tissue in the treatment of surface tumors, a circular heating device was developed to minimize the detrimental effects of freezing on neighboring tissue. This cryosurgical therapy could be efficiently applied to ablate tumors located closely to surfaces of organs. Thermographic images captured from experiments revealed that employing a proper heating coil could reduce the volume of frozen tissue. Additionally, simulated results showed that the judicious incorporation of a heating coil to a conventional

cryosurgical system enabled to sustain the volume of 233 K isotherm while effectively reducing of the over-freezing of neighboring tissue.

The heating coil coefficient was proposed for the first time to study the feasibility of incorporating a heating device to regulate the formation of the frozen tissue. Critical operating durations of heating coils in different sizes were given. Compared with larger heating coils, smaller coils performed better in reducing the frozen area of peripheral tissue but they were associated with shorter effective operating durations.

In Chapter 7, the RF-generated heating is incorporated into cryosurgery. In the first stage, performance of the RF and cryosurgical ablation was tested in *in-vitro* porcine livers separately. In RF ablation tests, both one-tine and multi-tine RF probes, were examined while the cryosurgical ablation was tested with a 4 mm diameter lab-made cryoprobe. The multi-step ablation procedure for multi-tine RF probe was found to be effective in producing a large ablation zone with uniform temperatures. The procedure reduced the overheating by moving the ablating electrodes within the tissue.

In the second stage of this study, a novel hybrid therapy coined as RF-assisted cryoprobe was proposed with the minimally invasive nature. The performance of proposed cryo-device was evaluated with a validated numerical model. RF-generated heating can effectively reduce the frozen tissue at the boundary during the cryosurgical ablation. The RF-assisted cryosurgery could largely reduce the frozen tissue while sustaining the size of the central complete ablation. However, the RF-generated heating was not effective as the cartridge heating in terms of reducing the frozen tissue. This was mainly because the energy conversion from electrical energy to thermal energy in the RF-generated heating is accomplished within tissue. The increase in the

applied voltage could reduce the size of the frozen tissue; however, according to simulation with voltages ranging from 35 V to 55 V, the increased voltage only induced a marginal reduction of the frozen tissue.

8.2. Contributions to knowledge

a.) The phenomenon of "pressure jump" is observed to be effective to accelerate the flow rate to reach the predetermined level within the initial stage of freezing. The pressure of the freezing medium must be reduced to maintain the flow rate of the freezing medium. Under the passive controlling protocol where the pressure is consistent, the temperature depreciation of cryoprobe increases within the initial stage of freezing.

b.) By using orthogonal experiment analysis, the flow rate is found to be the major influencing factor for the initial freezing while the nitrogen liquid level exerts the major impact on the induced minimum temperature.

c.) A bifurcate cryoprobe can generate a larger complete ablation zone with a higher degree of profile irregularity than a conventional cryoprobe, but it incurs the penalty of higher invasive trauma compared to the total tissue damage

d.) Incorporating a CT-scanned vascular image into cryosurgery planning enables cryosurgeons to achieve greater success rates by knowing how the isotherm at the critical temperature (i.e. 233 K) moves in the vascular tissue. The heating effects produced by large vessels generate less thermal impacts on tissue with low freezing temperatures than

tissue with high freezing temperatures, due to the formation of the buffer zone.

e.) The implementation of freeze-thaw cycles produces a "temperature diminishing effect" whereby the minimum tissue temperature is observed to reduce at a decrease rate after each freeze-thaw cycle.

f.) The proposed temperature-based damage rate has a close agreement with data derived from literature. The damage function has taken the overlapping effects of freeze-thaw cycles.

g.) The cryosurgical therapy with Joule heating devices is efficient to reduce the size of unwanted frozen tissue and sustain the size of the complete ablation zone. Compared with larger heating coils, smaller coils perform better in reducing the frozen area of peripheral tissue but they are associated with shorter effective operating durations.

h.) The multi-step ablation procedure for multi-tine RF probe was effective in producing a large ablation zone with uniform temperatures. The procedure reduced the overheating by moving the ablating electrodes within the tissue.

i.) RF-generated heating can effectively reduce the frozen tissue and sustain the size of the central complete ablation. However, the RF-generated heating was not effective as the cartridge heating in terms of reducing the frozen tissue.

8.3. Limitations of study

The limitations of this study include:

a.) Only liquid nitrogen is used to test the performance of cryosurgical process. Therefore, the experimental observation of the controlling parameters (i.e. flow rate, pressure) is based on this specific freezing medium.

b.) All experiments are conducted in *in-vitro* porcine livers and gelatin gels. The properties of *in-vitro* porcine livers and gelatin gels are not identical to human livers. The living organ has the vascular effects and metabolism that cannot be exactly measured with *in-vitro* samples.

c.) The study of heating effects due to the clinically-extracted vascular network is simulated with a two-dimensional model. The two-dimensional model is incapable of simulating three-dimensional structure of large vessels.

d.) Damage function during freeze-thaw cycles has been validated by one reference. More experiments are required to provide the validation data for different types of tumors.

8.4.   Recommendations for future work

For a better understanding of the bioheat transfer processes during cryosurgery, some possible future work may include:

a.) Additional supporting data can be achieved by the experiments conducted in *in-vivo* samples. The *in-vivo* samples provide the realistic experimental results with realistic vascular effects. The data could be used to improve the accuracy of the temperature development and the damage function for freeze-thawing cycles.

b.) The chemo-coated nanoparticles can be injected to the solid tumor via the expandable/retractable "antenna-like" hooked-shape channels in hybrid cryoprobe. This allows a new synergetic therapy involving chemo-nano-cryosurgery to be conducted in a highly controlled and targeted manner. A hybrid simulation model incorporating add-on chemo-coated targeted nanoparticles to the present model is presently being developed to study this new tri-hybrid tumor ablation method–chemotherapy hybrid with targeted nanoparticles hybrid with cryosurgery.

c.) Numerical and experimental investigation on how multiple cryoprobes can be employed to optimize the formation of frozen tissue within the irregularly shaped tumors. Incorporation of the thermal conductivity of nanoparticles into the analysis on multiple cryoprobe or fractal tree-like branched networks using the Hamilton Crosser model to study how the resultant thermal conductivity varies with the network geometrical structures.

d.) A numerical study can be developed to investigate various flow patterns of nitrogen in order to improve the performance of the cryo-devices. The results are applicable to the design of cryoprobes in small dimensions.

Bibliography

[1] A. Jemal, F. Bray, M.M. Center, J. Ferlay, E. Ward, D. Forman, Global cancer statistics, CA: a cancer journal for clinicians, 61(2) (2011) 69-90.

[2] J. Ferlay, H.R. Shin, F. Bray, D. Forman, C. Mathers, D.M. Parkin, Estimates of worldwide burden of cancer in 2008: GLOBOCAN 2008, International journal of cancer, 127(12) (2010) 2893-2917.

[3] W.J. Berger, J. Poledna, New strategies for the placement of cryoprobes in malignant tumors of the liver for reducing the probability of recurrences after hepatic cryosurgery, International Journal of Colorectal Disease, 16(5) (2001) 331-339.

[4] J. Shi, Z.Q. Chen, M.H. Shi, Simulation of heat transfer of biological tissue during cryosurgery based on vascular trees, Applied Thermal Engineering, 29(8-9) (2009) 1792-1798.

[5] F. Popken, M. Land, M. Bosse, H. Erberich, P. Meschede, D.P. König, J.H. Fischer, P. Eysel, Cryosurgery in long bones with new miniature cryoprobe: an experimental in vivo study of the cryosurgical temperature field in sheep, European Journal of Surgical Oncology, 29(6) (2003) 542-547.

[6] J. Bickels, I. Meller, M. Malawer, The biology and role of cryosurgery in the treatment of bone tumors, in: Musculoskeletal Cancer Surgery, Kluwer Academic Publishers, 2004, pp. 135-145.

[7] J. Seifert, A pig model of hepatic cryotherapy. In vivo temperature distribution during freezing and histopathological changes, Cryobiology, 47(3) (2003) 214-226.

[8] J. Joosten, G. Jager, W. Oyen, T. Wobbes, T. Ruers, Cryosurgery and radiofrequency ablation for unresectable colorectal liver metastases, European Journal of Surgical Oncology, 31(10) (2005) 1152-1159.

[9] K.J. Chua, S.K. Chou, On the study of the freeze–thaw thermal process of a biological system, Applied Thermal Engineering, 29(17-18) (2009) 3696-3709.

[10] J. Arnott, On the treatment of cancer, by the regulated application of an anaesthetic temperature, 1855.

168

[11] L. Cailletet, Recherches sur la liquéfaction des gaz, Ann Chemie Physique, 15 (1878) 132-144.

[12] S. Cooper, R. Dawber, The history of cryosurgery, JRSM, 94(4) (2001) 196-201.

[13] K.J. Chua, X. Zhao, S.K. Chou, Effects of crucial parameters on the freezing delivery in the cryosurgical system, Applied Thermal Engineering, 51(1–2) (2013) 734-741.

[14] M. Yan Moore, Paul Sofer, MD, Mordechay Ilovich, PhD, The science and technology behind cryosurgery, Technical Notes,   (2001).

[15] R.C. Marcove, T.R. Miller, Treatment of primary and metastatic bone tumors by cryosurgery, JAMA: The Journal of the American Medical Association, 207(10) (1969) 1890-1894.

[16] R.C. Marcove, D.S. Sheth, E.W. Brien, A.G. Huvos, J.H. Healey, Conservative surgery for giant cell tumors of the sacrum. The role of cryosurgery as a supplement to curettage and partial excision, Cancer, 74(4) (1994) 1253-1260.

[17] H. Bart Schreuder, H.B. Van Beem, R.P. Veth, Venous gas embolism during cryosurgery for bone tumors, Journal of surgical oncology, 60(3) (1995) 196-200.

[18] I.S. Cooper, A.S.J. Lee, Cryostatic congelation: a system for producing a limited, controlled region of cooling or freezing of biologic tissues, The Journal of nervous and mental disease, 133(3) (1961) 259.

[19] K.L. Reed, T.D. Brown, M.G. Conzemius, Focal cryogen insults for inducing segmental osteonecrosis: computational and experimental assessments of thermal fields, Journal of Biomechanics, 36(9) (2003) 1317-1326.

[20] Z.S. Deng, J. Liu, H.W. Wang, Disclosure of the significant thermal effects of large blood vessels during cryosurgery through infrared temperature mapping, International Journal of Thermal Sciences, 47(5) (2008) 530-545.

[21] T. Ichikawa, S.M. Erturk, T. Araki, Multiphasic contrast-enhanced multidetector-row CT of liver: Contrast-enhancement theory and practical scan protocol with a combination of fixed injection duration and patients' body-weight-tailored dose of contrast material, European Journal of Radiology, 58(2) (2006) 165-176.

[22] M.J. Bassignani, A.S. Fulcher, R.A. Szucs, W.K. Chong, U.R. Prasad, A. Marcos, Use of imaging for living donor liver transplantation, Radiographics, 21(1) (2001) 39-52.

[23] S.A. Müller, K. Bläuer, M. Kremer, M. Thorn, A. Mehrabi, H.-P. Meinzer, U. Hinz, J. Metzger, M.W. Büchler, B.M. Schmied, Exact CT-Based Liver Volume Calculation Including Nonmetabolic Liver Tissue in Three-Dimensional Liver Reconstruction, Journal of Surgical Research, 160(2) (2010) 236-243.

[24] G. Xiong, G. Choi, C.A. Taylor, Virtual interventions for image-based blood flow computation, Computer-Aided Design, 44(1) (2012) 3-14.

[25] A.V. Bui, R. Manasseh, K. Liffman, I.D. Sutalo, Development of optimized vascular fractal tree models using level set distance function, Medical Engineering & Physics, 32(7) (2010) 790-794.

[26] T. Peng, D.P. O'Neill, S.J. Payne, A two-equation coupled system for determination of liver tissue temperature during thermal ablation, International Journal of Heat and Mass Transfer, 54(9-10) (2011) 2100-2109.

[27] D. Heymann, D. Pence, V. Narayanan, Optimization of fractal-like branching microchannel heat sinks for single-phase flows, International Journal of Thermal Sciences, 49(8) (2010) 1383-1393.

[28] F. Zhao, Z.Q. Chen, M.H. Shi, Numerical study on freezing-thawing phase change heat transfer in biological tissue embedded with two cryoprobes, Journal of Central South University of Technology (English Edition), 16(2) (2009) 326-331.

[29] P. Yuan, Numerical analysis of an equivalent heat transfer coefficient in a porous model for simulating a biological tissue in a hyperthermia therapy, International Journal of Heat and Mass Transfer, 52(7-8) (2009) 1734-1740.

[30] H.H. Pennes, Analysis of tissue and arterial blood temperatures in the resting human forearm, Journal of Applied Physiology, 1(2) (1948) 93-122.

[31] W. Wulff, The energy conservation equation for living tissue, IEEE REVIEWS IN BIOMEDICAL ENGINEERING (6) (1974) 494-495.

[32] S. Wang, B. Yu, Study of the effect of capillary pressure on the permeability of porous media embedded with a fractal-like tree network, International Journal of Multiphase Flow, 37(5) (2011) 507-513.

[33] P. Xu, B. Yu, M. Yun, M. Zou, Heat conduction in fractal tree-like branched networks, International Journal of Heat and Mass Transfer, 49(19-20) (2006) 3746-3751.

[34] M.R. Rossi, D. Tanaka, K. Shimada, Y. Rabin, Computerized planning of cryosurgery using bubble packing: An experimental validation on a phantom material, International Journal of Heat and Mass Transfer, 51(23-24) (2008) 5671-5678.

[35] Y. Rabin, D.C. Lung, T.F. Stahovich, Computerized planning of cryosurgery using cryoprobes and cryoheaters, Technology in Cancer Research and Treatment, 3 (2004) 229-243.

[36] J. McGrath, E. Cravalho, C. Huggins, An experimental comparison of intracellular ice formation and freeze-thaw survival of HeLa S-3 cells, Cryobiology, 12(6) (1975) 540-550.

[37] M.M. Desai, I.S. Gill, Current status of cryoablation and radiofrequency ablation in the management of renal tumors, Current opinion in urology, 12(5) (2002) 387.

[38] A.A. Gage, Experimental cryogenic injury of the palate: Observations pertinent to cryosurgical destruction of tumors, Cryobiology, 15(4) (1978) 415-425.

[39] S. Yamada, S. Tsubouchi, Rapid cell death and cell population recovery in mouse skin epidermis after freezing, Cryobiology, 13(3) (1976) 317-327.

[40] J. Bischof, N. Merry, J. Hulbert, Rectal protection during prostate cryosurgery: design and characterization of an insulating probe, Cryobiology, 34(1) (1997) 80-92.

[41] N.E. Hoffmann, J.C. Bischof, The cryobiology of cryosurgical injury, Urology, 60(2) (2002) 40-49.

[42] J.F. Edd, B. Rubinsky, Detecting cryoablation with EIT and the benefit of including ice front imaging data, Physiological Measurement, 27 (2006) S175.

[43] Y. Rabin, A. Shitzer, A New Cryosurgical Device for Controlled Freezing: I. Setup and Validation Tests, Cryobiology, 33(1) (1996) 82-92.

[44] J.F. Yan, Z.S. Deng, J. Liu, Y.X. Zhou, New modality for maximizing cryosurgical killing scope while minimizing mechanical incision trauma using combined freezing-heating system, Journal of Medical Devices, 1(4) (2007) 264-271.

[45] G. John Morris, E. Acton, B.J. Murray, F. Fonseca, Freezing injury: The special case of the sperm cell, Cryobiology, 64(2) (2012) 71-80.

[46] D.R. Di, Z.Z. He, Z.Q. Sun, J. Liu, A new nano-cryosurgical modality for tumor treatment using biodegradable MgO nanoparticles, Nanomedicine: Nanotechnology, Biology and Medicine, (2012).

[47] K.B. Narayanan, N. Sakthivel, Green synthesis of biogenic metal nanoparticles by terrestrial and aquatic phototrophic and heterotrophic eukaryotes and biocompatible agents, Advances in Colloid and Interface Science, 169(2) (2011) 59-79.

[48] A.A. Gage, J.G. Baust, Cryosurgery for Tumors, Journal of the American College of Surgeons, 205(2) (2007) 342-356.

[49] G. Yang, A. Zhang, L.X. Xu, Intracellular ice formation and growth in MCF-7 cancer cells, Cryobiology, 63(1) (2011) 38-45.

[50] N.E. Hoffmann, J.C. Bischof, The cryobiology of cryosurgical injury, Urology, 60(2, Supplement 1) (2002) 40-49.

[51] A.A. Gage, J. Baust, Mechanisms of tissue injury in cryosurgery, Cryobiology, 37(3) (1998) 171-186.

[52] A. Radtke, G.C. Sotiropoulos, G. Sgourakis, E.P. Molmenti, T. Schroeder, F.H. Saner, S. Beckebaum, A. Schenk, H. Lang, C.E. Broelsch, M. Malagó, "Anatomical" versus "Territorial" Belonging of the Middle Hepatic Vein: Virtual Imaging and Clinical Repercussions, Journal of Surgical Research, 166(1) (2011) 146-155.

[53] W.J. Boeve, T. Kok, E.B. Haagsma, M.J.H. Slooff, W.J. Sluiter, R.L. Kamman, Superior diagnostic strength of combined contrast enhanced MR-angiography and MR-imaging compared to intra-arterial DSA in liver transplantation candidates, Magnetic Resonance Imaging, 19(5) (2001) 609-622.

[54] B. Chen, R. Ning, Cone-beam volume CT breast imaging: Feasibility study, Medical physics, 29 (2002) 755.

[55] F. Lee, D.M. Mahvi, S.G. Chosy, G.M. Onik, W.S. Wong, P.J. Littrup, K.A. Scanlan, Hepatic cryosurgery with intraoperative US guidance, Radiology, 202(3) (1997) 624-632.

[56] W.H. Brewer, R.S. Austin, G.W. Capps, J.P. Neifeld, Intraoperative monitoring and postoperative imaging of hepatic cryosurgery, in: Seminars in surgical oncology, Wiley Online Library, 1998, pp. 129-155.

[57] J.C. Saliken, B.J. Donnelly, J.C. Rewcastle, The evolution and state of modern technology for prostate cryosurgery, Urology, 60(2) (2002) 26-33.

[58] C. Lam, S. Shimi, A. Cuschieri, Ultrasonographic characterization of hepatic cryolesions: an ex vivo study, Archives of Surgery, 130(10) (1995) 1068.

[59] M.L. Rivoire, E.J. Voiglio, P. Kaemmerlen, G. Molina, I. Treilleux, J. Finzy, E. Delay, F. Gory, Hepatic cryosurgery precision evaluation of ultrasonography, thermometry, and impedancemetry in a pig model, Journal of surgical oncology, 61(4) (1998) 242-248.

[60] J.L. Chin, D.B. Downey, M. Mulligan, A. Fenster, Three-dimensional transrectal ultrasound guided cryoablation for localized prostate cancer in nonsurgical candidates: a feasibility study and report of early results, The Journal of urology, 159(3) (1998) 910-914.

[61] B.-Z. Maytal, M. Bliweis, G.E. Sturlesi, System and method for MRI-guided cryosurgery, in, Google Patents, 1999.

[62] G.A. Sandison, M.P. Loye, J.C. Rewcastle, L.J. Hahn, J.C. Saliken, J.G. McKinnon, B.J. Donnelly, X-ray CT monitoring of iceball growth and thermal distribution during cryosurgery, Physics in Medicine and biology, 43(11) (1999) 3309.

[63] M.J. Taylor, The effects of low temperatures on biological systems, B. W. W., Grout and G. J., Morris ed., Edward Arnold, 1987.

[64] W. Berger, B. Uhrik, Freeze-induced shrinkage of individual cells and cell-to-cell propagation of intracellular ice in cell chains from salivary glands, Cellular and Molecular Life Sciences, 52(9) (1996) 843-850.

[65] J. Bischof, K. Christov, B. Rubinsky, A morphological study of cooling rate response in normal and neoplastic human liver tissue: cryosurgical implications, Cryobiology, 30(5) (1993) 482-492.

[66] S. Bellman, J. Adams-Ray, Vascular Reactions After Experimental Cold Injury A Microangiographic Study on Rabbit Ears, Angiology, 7(4) (1956) 339-367.

[67] V.C. Giampapa, C. Oh, A.H. Aufses, The vascular effect of cold injury, Cryobiology, 18(1) (1981) 49-54.

[68] J.H. LeFebvre, L.E. Folke, Effects of subzero temperatures on the microcirculation in the oral mucous membrane, Microvascular Research, 10(3) (1975) 360-372.

[69] D. Whittaker, Mechanisms of tissue destruction following cryosurgery, Annals of the Royal College of Surgeons of England, 66(5) (1984) 313.

[70] D. Whittaker, Vascular responses in the oral mucosa following cryosurgery, Journal of periodontal research, 12(1) (1977) 55-63.

[71] J.C. Rewcastle, G.A. Sandison, L.J. Hahn, J.C. Saliken, J.G. McKinnon, B.J. Donnelly, A model for the time-dependent thermal distribution within an iceball surrounding a cryoprobe, Physics in Medicine and biology, 43 (1998) 3519.

[72] A.A. Gage, G.W. Greene Jr, M.E. Neiders, F.G. Emmings, Freezing bone without excision, JAMA: The Journal of the American Medical Association, 196(9) (1966) 770-774.

[73] E.D. Staren, M.S. Sabel, L.M. Gianakakis, G.A. Wiener, V.M. Hart, M. Gorski, K. Dowlatshahi, B.F. Corning, M.F. Haklin, G. Koukoulis, Cryosurgery of breast cancer, Archives of Surgery, 132(1) (1997) 28.

[74] A. Gage, What temperature is lethal for cells?, The Journal of dermatologic surgery and oncology, 5(6) (1979) 459.

[75] J.J. Smith, J. Fraser, An estimation of tissue damage and thermal history in the cryolesion, Cryobiology, 11(2) (1974) 139-147.

[76] M.L. Rivoire, E.J. Voiglio, P. Kaemmerlen, G. Molina, I. Treilleux, J. Finzy, E. Delay, F. Gory, Hepatic cryosurgery precision evaluation of ultrasonography, thermometry, and impedancemetry in a pig model, Journal of surgical oncology, 61(4) (1996) 242-248.

[77] J. Dow, K. Waterhouse, An experimental study in lethal freezing temperatures of the prostate gland, The Journal of urology, 103(4) (1970) 454.

[78] A.A. Gage, J.A. Caruana, M. Montes, Critical temperature for skin necrosis in experimental cryosurgery, Cryobiology, 19(3) (1982) 273-282.

[79] H.B. Neel III, A.S. Ketcham, W.G. Hammond, Cryonecrosis of normal and tumor - bearing rat liver potentiated by inflow occlusion, Cancer, 28(5) (1971) 1211-1218.

[80] P.L. Steponkus, D.G. Stout, J. Wolfe, R.V.E. Lovelace, Freeze-induced electrical transients and cryoinjury, Cryo Letters, 5 (1984) 343-348.

[81] K. Muldrew, L.E. McGann, Mechanisms of intracellular ice formation, Biophysical Journal, 57(3) (1990) 525-532.

[82] Z. Magalov, A. Shitzer, D. Degani, Isothermal volume contours generated in a freezing gel by embedded cryo-needles with applications to cryo-surgery, Cryobiology, 55(2) (2007) 127-137.

[83] W.G. Cahan, CRYOSURGERY OF MALIGNANT AND BENIGN TUMORS, Federation proceedings, 24 (1965) S241-S248.

[84] P. Dutta, M. Montes, A.A. Gage, Experimental hepatic cryosurgery, Cryobiology, 14(5) (1977) 598-608.

[85] H. Blum, Biological shape and visual science (part I), Journal of Theoretical Biology, 38(2) (1973) 205-287.

[86] T.K. Lee, D.I. McLean, M. Stella Atkins, Irregularity index: a new border irregularity measure for cutaneous melanocytic lesions, Medical Image Analysis, 7(1) (2003) 47-64.

[87] J.E. Golston, W.V. Stoecker, R.H. Moss, I.P.S. Dhillon, Automatic detection of irregular borders in melanoma and other skin tumors, Computerized Medical Imaging and Graphics, 16(3) (1992) 199-203.

[88] E. Claridge, P.N. Hall, M. Keefe, J.P. Allen, Shape analysis for classification of malignant melanoma, Journal of Biomedical Engineering, 14(3) (1992) 229-234.

[89] A.I. Medalia, Morphology of aggregates: I. Calculation of shape and bulkiness factors; application to computer-simulated random flocs, Journal of Colloid and Interface Science, 24(3) (1967) 393-404.

[90] O. Colot, R. Devinoy, A. Sombo, D. Brucq, A colour image processing method for melanoma detection, in: W. Wells, A. Colchester, S. Delp (Eds.) Medical Image Computing and Computer-Assisted Intervention — MICCAI'98, Springer Berlin Heidelberg, 1998, pp. 562-569.

[91] W.V. Stoecker, R.H. Moss, F. Ercal, S.E. Umbaugh, Nondermatoscopic digital imaging of pigmented lesions, Skin Research and Technology, 1(1) (1995) 7-16.

[92] V.T.Y. Ng, T.K. Lee, Measuring border irregularities of skin lesions using fractal dimensions,   (1996) 64-72.

[93] Z.S. Deng, J. Liu, Mathematical modeling of temperature mapping over skin surface and its implementation in thermal disease diagnostics, Computers in Biology and Medicine, 34(6) (2004) 495-521.

[94] K.J. Chua, Computer simulations on multiprobe freezing of irregularly

shaped tumors, Computers in Biology and Medicine, 41(7) (2011) 493-505.

[95] K.J. Chua, S.K. Chou, J.C. Ho, An analytical study on the thermal effects of cryosurgery on selective cell destruction, Journal of Biomechanics, 40(1) (2007) 100-116.

[96] M.R. Rossi, Y. Rabin, Experimental verification of numerical simulations of cryosurgery with application to computerized planning, Physics in Medicine and biology, 52 (2007) 4553.

[97] T. Galvez, J. Hengle, J. Mitchell, G.E. MYERS, K.L. SIEBECKER, Thermal response of human legs during cooling(Human legs thermal response during cooling for refrigeration anesthesia, deriving analytical model for temperature level prediction as function of time), Journal of Applied Physiology, 29 (1970) 859-865.

[98] G. Zhao, H.F. Zhang, X.J. Guo, D.W. Luo, D.Y. Gao, Effect of blood flow and metabolism on multidimensional heat transfer during cryosurgery, Medical Engineering & Physics, 29(2) (2007) 205-215.

[99] A. Shitzer, R.C. Eberhart, Heat transfer in medicine and biology: analysis and applications, Plenum Pub Corp, 1985.

[100] R. Barauskas, A. Gulbinas, T. Vanagas, G. Barauskas, Finite element modeling of cooled-tip probe radiofrequency ablation processes in liver tissue, Computers in Biology and Medicine 38(6) (2008) 694-708.

[101] S. Nath, J. DiMARCO, D.E. Haines, Basic aspects of radiofrequency catheter ablation, Journal of cardiovascular electrophysiology, 5(10) (1994) 863-876.

[102] A.N. Mirza, B.D. Fornage, N. Sneige, H.M. Kuerer, L.A. Newman, F.C. Ames, S.E. Singletary, Radiofrequency ablation of solid tumors, Cancer journal (Sudbury, Mass.), 7(2) (2001) 95.

[103] I. Chang, Finite element analysis of hepatic radiofrequency ablation probes using temperature-dependent electrical conductivity, Biomedical engineering online, 2(1) (2003) 12.

[104] D. Haemmerich, Biophysics of radiofrequency ablation.

[105] J.-P. Ritz, K.S. Lehmann, C. Isbert, C. Reissfelder, T. Albrecht, T. Stein, H.J. Buhr, In-Vivo Evaluation of a Novel Bipolar Radiofrequency Device for Interstitial Thermotherapy of Liver Tumors During Normal and Interrupted Hepatic Perfusion, Journal of Surgical Research 133(2) (2006)

176-184.

[106] C. McCann, M.D. Sherar, The use of a dispersive ground electrode with a loosely wound helical coil for interstitial radiofrequency thermal therapy, Physics in Medicine and biology, 51(15) (2006) 3851.

[107] D.J. Schutt, D. Haemmerich, Sequential activation of a segmented ground pad reduces skin heating during radiofrequency tumor ablation: optimization via computational models, Biomedical Engineering, IEEE Transactions on, 55(7) (2008) 1881-1889.

[108] R. Stoffner, C. Kremser, P. Schullian, M. Haidu, G. Widmann, R.J. Bale, Multipolar radiofrequency ablation using 4–6 applicators simultaneously: A study in the ex vivo bovine liver, European Journal of Radiology, 81(10) (2012) 2568-2575.

[109] M. Rivoire, F. De Cian, P. Meeus, S. Négrier, H. Sebban, P. Kaemmerlen, Combination of neoadjuvant chemotherapy with cryotherapy and surgical resection for the treatment of unresectable liver metastases from colorectal carcinoma, Cancer, 95(11) (2002) 2283-2292.

[110] T. Ravikumar, R. Kane, B. Cady, R. Jenkins, M. Clouse, G. Steele Jr, A 5-year study of cryosurgery in the treatment of liver tumors, Archives of Surgery, 126(12) (1991) 1520.

[111] M.L. Weaver, D. Atkinson, R. Zemel, Hepatic cryosurgery in treating colorectal metastases, Cancer, 76(2) (1995) 210-214.

[112] R.J. Bleicher, D.P. Allegra, D.T. Nora, T.F. Wood, L.J. Foshag, A.J. Bilchik, Radiofrequency ablation in 447 complex unresectable liver tumors: lessons learned, Annals of Surgical Oncology, 10(1) (2003) 52-58.

[113] R. Adam, E.J. Hagopian, M. Linhares, J. Krissat, E. Savier, D. Azoulay, F. Kunstlinger, D. Castaing, H. Bismuth, A comparison of percutaneous cryosurgery and percutaneous radiofrequency for unresectable hepatic malignancies, Archives of Surgery, 137(12) (2002) 1332.

[114] L. Solbiati, T. Livraghi, S.N. Goldberg, T. Ierace, F. Meloni, M. Dellanoce, L. Cova, E.F. Halpern, G.S. Gazelle, Percutaneous Radio-frequency Ablation of Hepatic Metastases from Colorectal Cancer: Long-term Results in 117 Patients1, Radiology, 221(1) (2001) 159-166.

[115] J.D. Hardy, E.F. Du Bois, G. Soderstrom, Basal Metabolism, Radiation, Convection and Vaporization at Temperatures of 22 to 35° C. Six Figures, The Journal of Nutrition, 15(5) (1938) 477-497.

[116] A.C. Burton, The application of the theory of heat flow to the study of energy metabolism, J. Nutr, 7 (1934) 497-533.

[117] Y. Rabin, T.F. Stahovich, Cryoheater as a means of cryosurgery control, Physics in Medicine and biology, 48 (2003) 619-632.

[118] Y. Rabin, A. Shitzer, Exact solution to the one-dimensional inverse-stefan problem in nonideal biological tissues, Journal of Heat Transfer, 117 (1995) 425-431.

[119] Y. Jiang, S. Mulier, W. Chong, M.C. Diel Rambo, F. Chen, G. Marchal, Y. Ni, Formulation of 3D finite elements for hepatic radiofrequency ablation, International Journal of Modelling, Identification and Control, 9(3) (2010) 225-235.

[120] I.A. Chang, Considerations for thermal injury analysis for RF ablation devices, The open biomedical engineering journal, 4 (2010) 3.

[121] A. Stogryn, Equations for Calculating the Dielectric Constant of Saline Water (Correspondence), Microwave Theory and Techniques, IEEE Transactions on, 19(8) (1971) 733-736.

[122] S. Tungjitkusolmun, S.T. Staelin, D. Haemmerich, J.Z. Tsai, H. Cao, J.G. Webster, F.T. Lee Jr, D.M. Mahvi, V.R. Vorperian, Three-dimensional finite-element analyses for radio-frequency hepatic tumor ablation, IEEE Transactions on Biomedical Engineering, 49(1) (2002) 3-9.

[123] T. Amago, Sizing optimization using response surface method in FOA, R&D Review of Toyota CRDL, 37(1) (2002) 1-7.

[124] K. Yakut, N. Alemdaroglu, I. Kotcioglu, C. Celik, Experimental investigation of thermal resistance of a heat sink with hexagonal fins, Applied Thermal Engineering, 26(17–18) (2006) 2262-2271.

[125] S. Gunes, E. Manay, E. Senyigit, V. Ozceyhan, A Taguchi approach for optimization of design parameters in a tube with coiled wire inserts, Applied Thermal Engineering, 31(14–15) (2011) 2568-2577.

[126] T. Sung, D. Oh, S. Jin, T.W. Seo, J. Kim, Optimal design of a micro evaporator with lateral gaps, Applied Thermal Engineering, 29(14–15) (2009) 2921-2926.

[127] I. Kotcioglu, A. Cansiz, M. Nasiri Khalaji, Experimental investigation for optimization of design parameters in a rectangular duct with plate-fins heat exchanger by Taguchi method, Applied Thermal Engineering, 50(1) (2013) 604-613.

[128] Y.-S. Tseng, H.-H. Fu, T.-C. Hung, B.-S. Pei, An optimal parametric design to improve chip cooling, Applied Thermal Engineering, 27(11–12) (2007) 1823-1831.

[129] L. Franek, X. Jiang, Orthogonal design of experiments for parameter learning in image segmentation, Signal Processing, (0).

[130] W. Dewey, L. Hopwood, S. Sapareto, L. Gerweck, Cellular responses to combinations of hyperthermia and radiation, Radiology, 123(2) (1977) 463-474.

[131] M. Stańczyk, J. Telega, Thermal problems in biomechanics–a review. Part III. Cryosurgery, cryopreservation and cryotherapy, Acta of Bioengineering and Biomechanics, 5(2) (2003) 3-22.

[132] P.W. Wilson, The Kinetic Basis of Molecular Biology, Journal of the American Chemical Society, 77(5) (1955) 1395-1396.

[133] E.L. Carstensen, M. Miller, C. Linke, Biological effects of ultrasound, Journal of Biological Physics, 2(4) (1974) 173-192.

[134] J. Sun, A. Zhang, L.X. Xu, Evaluation of alternate cooling and heating for tumor treatment, International Journal of Heat and Mass Transfer, 51(23-24) (2008) 5478-5485.

[135] A. McKelvey, R. Ritchie, Fatigue-crack growth behavior in the superelastic and shape-memory alloy Nitinol, Metallurgical and Materials Transactions A, 32(13) (2001) 731-743.

[136] B. Reedlunn, C.B. Churchill, E.E. Nelson, S.H. Daly, J.A. Shaw, Tension, compression, and bending of superelastic shape memory alloy tubes, Journal of the Mechanics and Physics of Solids, (0).

[137] D. GLOZMAN, M. SHOHAM, Controlled steering of a flexible needle, in, WO Patent 2,007,141,784, 2007.

[138] N.S. Racz, Flow elements for use with flexible spinal needles, needle assemblies and methods therefor, in, Google Patents, 2008.

[139] J. Yu, P. Liang, X. Yu, F. Liu, L. Chen, Y. Wang, A comparison of microwave ablation and bipolar radiofrequency ablation both with an internally cooled probe: Results in ex vivo and in vivo porcine livers, European Journal of Radiology, 79(1) (2011) 124-130.

[140] Y. Zhang, J. Liu, Y. Zhou, Pilot study on cryogenic heat transfer in biological tissues embedded with large blood vessels, Forschung im

Ingenieurwesen, 67(5) (2002) 188-197.

[141] K.H.W. Böker, A. Franzen, M. Wrobel, M.J. Bahr, U. Tietge, M.P. Manns, Regulation of hepatic blood flow in patients with liver cirrhosis and after liver transplantation, Pathophysiology, 6(4) (2000) 251-260.

[142] W.W. Lautt, C.V. Greenway, Conceptual review of the hepatic vascular bed, Hepatology, 7(5) (1987) 952-963.

[143] D. O'Neil, Blood Components, Palomar College, 1999.

[144] D. Biswas, U.S. Chakraborty, A Brief Review on Blood Flow Modeling in Arteries, Assam University Journal of Science and Technology, 6(2) (2010) 10-15.

[145] K.J. Chua, Fundamental experiments and numerical investigation of cryo-freezing incorporating vascular network with enhanced nano-freezing, International Journal of Thermal Sciences, 70(0) (2013) 17-31.

[146] K. Steinke, C. Arnold, S. Wulf, D.L. Morris, Safety of radiofrequency ablation of myocardium and lung adjacent to the heart: an animal study, Journal of Surgical Research, 114(2) (2003) 140-145.

[147] J. Li, J. Chen, L. Zhou, J. Zeng, F. Yao, B. Wu, G. Fang, C. Deng, Z. Chen, Y. Leng, K. Xu, L. Niu, J. Zuo, K. Xu, Comparison of dual- and triple-freeze protocols for hepatic cryoablation in a Tibet pig model, Cryobiology, (0).

[148] M.Z. Kiss, M.J. Daniels, T. Varghese, Investigation of temperature-dependent viscoelastic properties of thermal lesions in ex vivo animal liver tissue, Journal of Biomechanics, 42(8) (2009) 959-966.

[149] C.Y. Lee, J. Bastacky, Comparative Mathematical Analyses of Freezing in Lung and Solid Tissue, Cryobiology, 32(4) (1995) 299-305.

[150] J. Liu, Uncertainty analysis for temperature prediction of biological bodies subject to randomly spatial heating, Journal of Biomechanics, 34(12) (2001) 1637-1642.

[151] T. Hirai, Y. Korogi, K. Ono, K. Maruoka, K. Harada, S. Aridomi, M. Takahashi, Intraarterial chemotherapy or chemoembolization for locally advanced and/or recurrent hepatic tumors: evaluation of the feeding artery with an interventional CT system, Cardiovascular and Interventional Radiology, 24(3) (2001) 176-179.

[152] R.S. Okten, F. Kucukay, H. Dedeoglu, M. Akdogan, S. Kacar, B. Bostanci, T. Olcer, Branching patterns of the main portal vein: Effect on estimated remnant liver volume in preoperative evaluation of donors for liver transplantation, European Journal of Radiology, 81(3) (2012) 478-483.

[153] B.W. Shaw Jr, D.J. Martin, J.M. Marquez, Y. Kang, A.C. Bugbee Jr, S. Iwatsuki, B.P. Griffith, R.L. Hardesty, H.T. Bahnson, T.E. Starzl, Venous bypass in clinical liver transplantation, Annals of Surgery, 200(4) (1984) 524.

[154] J.C. Rewcastle, G.A. Sandison, K. Muldrew, J.C. Saliken, B.J. Donnelly, A model for the time dependent three-dimensional thermal distribution within iceballs surrounding multiple cryoprobes, Medical physics, 28 (2001) 1125.

[155] B.L. Daniel, K. Butts, W.F. Block, Magnetic resonance imaging of frozen tissues: temperature-dependent MR signal characteristics and relevance for MR monitoring of cryosurgery, Magnetic resonance in medicine, 41(3) (1999) 627-630.

[156] J.M. Henderson, G.J. Mackay, M.H. Kutner, B. Noe, Volumetric and functional liver blood flow are both increased in the human transplanted liver, Journal of Hepatology, 17(2) (1993) 204-207.

[157] J. Marigold, I. Gilmore, R. Thompson, Effects of a meal on plasma clearance of [14C] glycocholic acid and indocyanine green in man, Clinical science (London, England: 1979), 61(3) (1981) 325.

[158] C.K. Svensson, D.J. Edwards, P.M. Mauriello, S.H. Barde, A.C. Foster, R.A. Lanc, E. Middleton, D. Lalka, Effect of food on hepatic blood flow: implications in the "food effect" phenomenon, Clinical Pharmacology & Therapeutics, 34(3) (1983) 316-323.

[159] J.F. Langenhuijsen, E.M.P. Broers, H. Vergunst, Cryosurgery for Prostate Cancer: an Update on Clinical Results of Modern Cryotechnology, European Urology, 55(1) (2009) 76-86.

[160] H. Rhim, S.N. Goldberg, G.D. Dodd, L. Solbiati, H.K. Lim, M. Tonolini, O.K. Cho, Essential Techniques for Successful Radio-frequency Thermal Ablation of Malignant Hepatic Tumors1, Radiographics, 21(suppl 1) (2001) S17.

[161] R.B. Coleman, R.N. Richardson, A novel closed cycle cryosurgical system, International Journal of Refrigeration, 28(3) (2005) 412-418.

[162] E. Cao, Y. Chen, Z. Cui, P.R. Foster, Effect of freezing and thawing rates on denaturation of proteins in aqueous solutions, Biotechnology and Bioengineering, 82(6) (2003) 684-690.

[163] H. Takeda, S. Maruyama, J. Okajima, S. Aiba, A. Komiya, Development and estimation of a novel cryoprobe utilizing the Peltier effect for precise and safe cryosurgery, Cryobiology, 59(3) (2009) 275-284.

[164] P.V. Hobbs, Ice physics, in, Clarendon Press, 1974, pp. 627.

[165] Y.T. Zhang, J. Liu, Numerical study on three-region thawing problem during cryosurgical re-warming, Medical Engineering & Physics, 24(4) (2002) 265-277.

[166] R.W. Lewis, K. Morgan, H. Thomas, K. Seetharamu, The finite element method in heat transfer analysis, John Wiley & Sons, 1996.

[167] G. Peng, X. Chen, W. Wu, X. Jiang, Modeling of water sorption isotherm for corn starch, Journal of Food Engineering, 80(2) (2007) 562-567.

[168] B. Medtronic, Radiofrequency Energy Ablation, Business briefing: US kidney and urological disease, (2005) 1-2.

[169] H. Elhaway, S. Oguro, K. Tuncali, P.R. Morrison, S. Tatli, P.B. Shyn, S.G. Silverman, N. Hata, Multimodality non-rigid image registration for planning, targeting and monitoring during CT-guided percutaneous liver tumor cryoablation, Academic Radiology, 17(11) (2010) 1334-1344.

[170] X. Zhao, K.J. Chua, Studying the thermal effects of a clinically-extracted vascular tissue during cryo-freezing, Journal of Thermal Biology (2012).

[171] F. Popken, Comparison of Iceball Diameter and Temperature Distribution Achieved with 3-mm Accuprobe Cryoprobes in Porcine and Human Liver Tissue and Human Colorectal Liver Metastases in Vitro, Cryobiology, 40(4) (2000) 302-310.

[172] G. Zhao, D. Luo, Z. Liu, D. Gao, Comparative study of the cryosurgical processes with two different cryosurgical systems: the endocare cryoprobe system versus the novel combined cryosurgery and hyperthermia system, Latin American applied research, 37(3) (2007) 215-222.

[173] J. Cha, Y.-s. Kim, H. Rhim, H.K. Lim, D. Choi, M.W. Lee, Radiofrequency ablation using a new type of internally cooled electrode with an adjustable active tip: An experimental study in ex vivo bovine and in vivo porcine livers, European Journal of Radiology, 77(3) (2011)

516-521.

[174] T. Lorentzen, A cooled needle electrode for radiofrequency tissue ablation: thermodynamic aspects of improved performance compared with conventional needle design, Academic Radiology, 3(7) (1996) 556-563.

Publications

[1] **X. Zhao**, K.J. Chua, S.K. Chou, A cryosurgical planning based on the shape factor of complete ablation zone (Pending).

[2] **X. Zhao**, K.J. Chua, S.K.Chou, A new modality for the irregularly shaped tumor treatment with the analysis of the irregularity of the cryonecrosis zone, in: International Conference on Engineering and Applied Science, Tokyo, Japan, 2013.

[3] **X. Zhao**, K.J. Chua, On the study of reducing the unwanted frozen area through an optimized thermal process, Biomedical Engineering, (Pending)(2013).

[4] **X. Zhao**, K.J. Chua, S.K.Chou, Numerical investigation of a novel smart cryoprobe incorporating with shape memory effects, in: International Conference on Life Science & Biological Engineering, Tokyo, Japan, 2013.

[5] **X. Zhao**, K.J. Chua, Investigating the cryoablative efficacy of a hybrid cryoprobe operating under freeze–thaw cycles, Cryobiology, 66 (2013) 239-249.

[6] K.J. Chua, **X. Zhao**, S.K. Chou, Effects of crucial parameters on the freezing delivery in the cryosurgical system, Applied Thermal Engineering 51 (2013) 734-741.

[7] **X. Zhao**, K.J. Chua, Studying the thermal effects of a clinically-extracted vascular tissue during cryo-freezing, Journal of Thermal Biology (2012).